1992

Phase equilibria, superconductivity, and flux creep in Nd1+[subscript x]Ba2-[subscript x]Cu3O7+[subscript delta] superconductors

Sang-Im Yoo
Iowa State University

Order Number 9234864

Phase equilibria, superconductivity, and flux creep in $Nd_{1+x}Ba_{2-x}Cu_3O_{7+\delta}$ superconductors

Yoo, Sang-Im, Ph.D.

Iowa State University, 1992

U·M·I
300 N. Zeeb Rd.
Ann Arbor, MI 48106

Phase equilibria, superconductivity, and flux creep in $Nd_{1+x}Ba_{2-x}Cu_3O_{7+\delta}$ superconductors

by

Sang-Im Yoo

A Dissertation Submitted to the
Graduate Faculty in Partial Fulfillment of the
Requirements for the Degree of
DOCTOR OF PHILOSOPHY

Department: Materials Science and Engineering
Major: Metallurgy

Approved:

Signature was redacted for privacy.

In Charge of Major Work

Signature was redacted for privacy.

For the Major Department

Signature was redacted for privacy.

For the Graduate College

Iowa State University
Ames, Iowa

1992

To Younshin

TABLE OF CONTENTS

GENERAL INTRODUCTION

$NdBa_2Cu_3O_7$ is a member of the $REBa_2Cu_3O_7$ (RE123) (RE = Y and rare earth elements except Ce, Pr, Pm, and Tb) class of high temperature superconductors which commonly have a superconducting temperature (T_c) of approximately 92 K. The prototype of this class is Y123. While it is tempting to assume that aside from effects due to the different magnetic moments of the RE ions these materials are quite similar, in fact, the phase diagrams of the RE-Ba-Cu-O system differ in very significant ways [1]. Because of these differences, the possibility arises that a RE123 other than Y123 may be the most suitable for applications. Among these other RE123 phases, Nd123 is interesting for the following reasons; (1) it has wider primary solidification range than Y123 on the RE_2O_3-CuO-BaO pseudo-ternary phase diagrams [2], (2) it exhibits about 100°C higher peritectic decomposition temperature than Y123 [3], and (3) unlike Y123, it forms a solid solution of $Nd_{1+x}Ba_{2-x}Cu_3O_{7+\delta}$ (Nd123ss) [4-8]. In particular, it is hypothesized that this substitution of Nd on Ba sites will result in a uniform distribution of point defects. This distribution of point defects should serve as pinning centers for magnetic flux lines penetrating the Type II superconductor which will enhance the current carrying capabilities of the materials. In this thesis, the subsolidus phase relations in the Nd-Ba-Cu-O system will be investigated. Next, superconductivity of the Nd123ss materials will be extensively studied, and finally, the role of uniformly distributed point defects in Nd123ss as flux pinning centers will be investigated.

Historically, superconductivity was first discovered in mercury by H. Kammerlingh Onnes in 1911 [9]. Thereafter, more than 25 metallic elements [10] and several thousand alloys [11] have been reported to exhibit superconductivity. However, the highest T_c achieved before 1986 was 23.2 K for Nb_3Ge [12,13]. For a brief review on the

development of superconductors prior to 1986, the superconductivity time line as reproduced in Fig. 1 from ref [14] is noteworthy. Since the newly discovered high T_c superconductors (usually, $T_c > 30$ K) are all ceramic materials based on the metal oxides, other low T_c (< 30 K) superconducting oxides discovered before 1986 are also listed in Table 1.

In early 1986, there was a tremendous breakthrough in superconductivity; a new material with a superconducting transition to zero electrical resistivity at an unprecedentedly high temperature of ~35 K was discovered by Bednortz and Müller [16] in the La-Ba-Cu-O system and substantiated by other groups [17,18]. The superconducting phase was identified to be $La_{2-x}Ba_xCuO_4$ [19]. By early 1987, it had been reported that the transition temperature could be raised to about 40 K by substituting strontium for barium [20-22].

The next dramatic event was reported by Wu et al. [23], who had observed a transition temperature as high as 92 K in the Y-Ba-Cu-O system. The same transition was also observed independently by many other groups [24-27]. The superconducting phase was identified to have the composition of $YBa_2Cu_3O_{7-y}$ (Y123) [28-31] and its crystal structure was determined to be an orthorhombic, distorted, oxygen-deficient perovskite structure by x-ray diffraction and transmission electron microscopy [32-34]. The substitution of rare earth elements (except Ce, Pr, Pm, and Tb) for yttrium was reported to have little effect on the superconducting transition temperatures [35], which is an unexpected result because it has been long known that even small amounts of magnetic impurities, like rare earth elements, can destroy superconductivity in the conventional superconductors [36]. Ce, Pr, and Tb have two valence states of +3 and +4. Both Ce and Tb do not form the 123 compound. Though Pr forms the 123 compound, it is not superconducting [37], and Pm123 is unknown because it is radioactive and unstable.

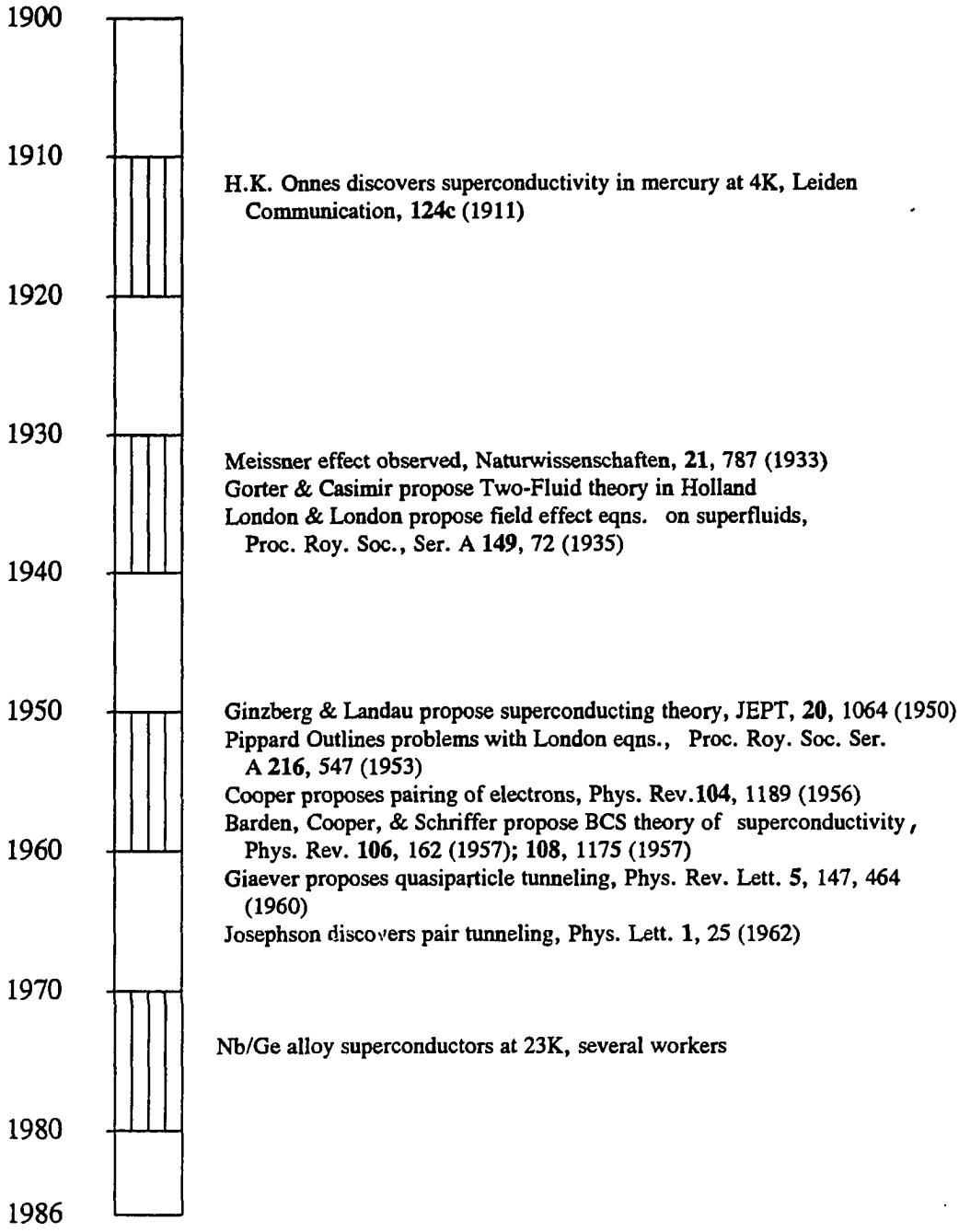

Fig. 1. Superocnductivity time line from 1900 to 1986. From W. J. Painter [14].

Table 1. Low T_c superconducting oxides discovered prior to 1986. From C. W. Chu [15]

Compound System	T_c(K)	Parent Insulator	Remark
NbO	1.2 - 1.5		a
TiO	0.6 - 1.3		b
$SrTiO_{3-\delta}$	0.7	$SrTiO_3$	c
A_xWO_3 *A = alkaline or alkaline earth*	0.6 - 6.0	WO_3	d
$Ag_2O_8HF_2$	1		e
$Li_{1+x}Ti_{2-x}O_4$	13	$Li_{4/3}Ti_{5/3}O_4$	f
$Ba(Pb_{1-x}Bi_x)O_3$	13	$BaBiO_3$ *(or the semimetallic $BaPbO_3$)*	g

a. W. Meissner, H. Franz, and H. Westerhoff, Ann. Phys. **17**, 593 (1933).

b. G.H. Hardy and J. K. Hulm, Phys. Rev. **93**, 1004 (1954).

c. J. F. Schooley, W. R. Hosler, and M. L. Cohen, Phys. Rev. Lett. **12**, 474 (1964)

d. C. J. Raub, A. W. Sweedler, M. A. Jensen, S. Broadston, and B. T. Matthias, Phys. Rev. Lett. **13**, 746 (1964)

e. M. B. Robin, K. Andres, T. H. Geballe, N. A. Kuebler, and D. B. McWhan, Phys. Rev. Lett. **17**, 917 (1966)

f. D. C. Johnston, H. Prakash, W. H. Zachariasen, and R. Viswanathan, Mat. Res. Bull. **8**, 777 (1973); D. C. Johnston, J. Low Temp. Phys. **25**, 145 (1976)

g. A. W. Sleight, J. L. Gillson, and P.E. Bierstedt, Solid State. Comm. **17**, 27 (1975)

In early 1988, several new systems having even higher superconducting transition temperatures were discovered. The Bi-Ca-Sr-Cu-O system [38] and the Tl-Ca-Ba-Cu-O system [39], commonly having several superconducting phases, were found to exhibit maximum transition temperatures of 110 and 125 K respectively. The $(Nd_{1-x}Ce_x)_2\ CuO_4$ materials [40] with T_c above 30 K were found to be electron-type superconductors in contrast to the hole-type ones of other CuO-based materials.

Since the materials having a T_c above nitrogen temperature (77 K) could be operated using relatively cheap liquid nitrogen rather than helium, the new superconducting ceramics could have the revolutionary impact on our way of life if useful devices can be fabricated. The applications of superconductor can be divided into two categories [14]. One is for small-magnitude devices which include superconductor wire, solid state devices known as Josephson junctions, and superconductor film. The other is for large-magnitude devices which include the generation of high magnetic fields such as the superconducting super collider (SSC), larger scale generation, storage, and transmission of electrical power, and trains levitated by superconductive magnets.

The new ceramic superconductors present many exciting possibilities for useful applications as mentioned previously, whereas there are many severe obstacles to be overcome to make applications a reality. Those obstacles have been the challenge of the materials science and engineering community. Two significant obstacles for bulk-type applications are low current carrying capacity and poor fabricability. The low current carrying capacity (i.e., low critical current density, J_c) is not due to the intrinsic property of the new ceramic superconductors. Single crystals of $YBa_2Cu_3O_{7-y}$ show very high J_c [41,42], which is suitable for application (usually, $J_c > 10^5$ A/cm^2), and thin films with $J_c \sim 10^5$ A/cm^2 at the liquid nitrogen temperature under zero field have been fabricated [43-45]. Therefore, this problem may be also overcome in the bulk-type ceramics by

controlling the microstructure through the optimization of thermal processing.

The poor fabricability is, however, due to intrinsic mechanical properties of the new superconducting materials. These oxides are brittle with limited slip systems [46] and can not be plastically deformed using traditional mechanical techniques. Moreover, the mechanical strength appears to be too weak under the magnetic field stress for a strong magnetic application [15]. In order to solve this problem, Ag-sheathed composites have been fabricated [47], but it remains a challenge to achieve an applicable level.

The low transport critical current densities of these sintered ceramics and their severe degradation in a magnetic field are considered to be originated from two major sources; the anisotropic conductivity along the crystallographic direction and the weak coupling at the grain boundaries. The weak links at the grain boundaries are due to the segregation of second phases or impurities at grain boundaries, poor connectivity between grains, microcracks or stressed regions, and the chemical or structural deviation near grain boundaries. Furthermore, even if grain boundaries are clean, large crystal mismatch such as high angle grain boundary can be the origin of the weak link because of the extremely short coherence lengths of these materials. Therefore, much effort has been focused on the phase purification during synthesis, and on the thermal processing to get high density without producing microcracks.

In addition to the above sources for the low J_c, high T_c superconductors have a rather serious problem of the large magnetic flux creep in applications at high temperatures and fields. In a Type II superconductor at high field, the magnetic field penetrates the material. If the flux lines are free to move, the Lorentz force between the flux lines and the currents in the superconductor will cause the flux lines to move, transferring energy from the current to the flux line lattice. This results in a voltage drop (i.e., a non-zero resistance). Therefore, the flux lines must be pinned in order to observe zero resistance in

the presence of a current, which implies that higher J_c is obtained if the flux lines are more strongly pinned. Consequently, it is essential to introduce the effective flux pinning centers in the Type II superconductors for the enhancement of J_c. Although the flux pinning mechanism has not been identified yet in the high T_c superconductors, considerable effort has been made to introduce the pinning centers into bulk-type superconductors. Recent experiments, such as the production of defects in the Y123 single crystal by the irradiation of neutrons [48], protons [49], and heavy ions [50], and the precipitation of fine grained CuO phase within $YBa_2Cu_3O_{7-\delta}$ phase by decomposing $YBa_2Cu_4O_y$ [51], have confirmed that the effective pinning centers exist and hence J_c can be improved in the high T_c superconductors. Though many methods are applicable for the introduction of pinning centers, the above methods are difficult to be applied for the superconducting devices such as wire. Therefore, much simple methods to achieve strong pinning centers would be highly desirable.

For the present study, RE123 materials were selected with the following reasons. First, though RE123 superconductors have lower T_c's than those of Bi-compounds (T_c = 110 K for $Bi_2Ca_2Sr_2Cu_3O_y$: Bi-2223) or Tl-compounds (T_c = 125 K for $Tl_2Ca_2Ba_2Cu_3O_y$: Tl-2223), it is relatively easy to synthesize pure RE123 phase compared to the Bi-2223 compound because the latter needs to be doped with PbO which is volatile during thermal processing, and Tl-compounds contain Tl-oxides which are also volatile and, even worse, toxic. Second, of all the high T_c ceramic superconductors, RE123 superconductors are known to be unique materials which may be applicable at 77 K because of their relatively strong flux pinning compared with other high T_c materials. Third, while the magnetic moments of rare earths lead to interesting magnetic interactions at low temperatures [52], they have minimal effect on T_c and therefore, the presence or absence of the magnetic moment does not directly bear on the choice of RE for

applications.

Among RE123 materials, the reasons for the selection of the Nd123 superconductor are numerous as previously described. Contrary to the Y123 phase (or heavy rare earth elements except Tb) which are point compounds on the phase diagram, Nd123 is known to have a solid solution of $Nd_{1+x}Ba_{2-x}Cu_3O_{7+\delta}$ like other light rare earth RE123 (RE= La, Sm,and Eu) phases. In addition, neodymia (Nd_2O_3) is an order of magnitude cheaper than yttria (Y_2O_3) or other rare earth metal oxides. Consequently, Nd123 is an interesting alternative to Y123 for application and hence a systematic study in the Nd-Ba-Cu-O system must be required.

The outline of this dissertation is as following. In the first chapter, the extensive study on the subsolidus phase relations in the Nd-Ba-Cu-O system is reported. In order to optimize the processing of the Nd123 superconductor, it was necessary to determine the subsolidus phase relationships around the Nd123 compound. More than 30 nominal compositions around Nd123 compound in the Nd-Ba-Cu-O system were selected, processed, and reacted at 890°C in air. The subsolidus phase relationships were determined by a triangular method on the basis of the compounds analyzed by x-ray diffraction. This study raised a question as to whether there exists a solid solution in $Nd_{1+x}Ba_{2-x}Cu_3O_{7+\delta}$ as reported in the literature [4-8] and, if it exists, what the solid solubility limit is, since the upper limit reported for $Nd_{1+x}Ba_{2-x}Cu_3O_{7+\delta}$ showed a large discrepancy in the values of x (i.e., x ranged from 0.5 to 1.0) in the literature. To clarify these discrepancies, a systematic study on the $Nd_{1+x}Ba_{2-x}Cu_3O_{7+\delta}$ solid solution system has been completed. In addition, phase stabilities of these solid solutions as a function of oxygen partial pressure have been studied. In the second chapter, the superconductivity of the $Nd_{1+x}Ba_{2-x}Cu_3O_{7+\delta}$ solid solutions have been extensively studied. The experimental results revealed that the superconducting transition temperatures were almost constant for x

$\leq$ 0.06. The effects of thermal processing on the superconducting transitions have been also studied and discussed with the aid of the results of the structural analysis by neutron diffraction. In the third chapter, the theoretical background on the flux creep including the basic properties of superconductivity is reviewed. In addition, a flux pinning mechanism proposed by Hylton and Beasley [53] is introduced to qualitatively understand the present system. In the last chapter, flux creep in $Nd_{1+x}Ba_{2-x}Cu_3O_{7+\delta}$ has been investigated in the composition range of $0.0 \leq x \leq 0.1$. Since the substitution of Nd for the Ba sites induces an occupation of the O(5) sites shown in Fig. 2, which has been verified by neutron diffraction through a cooperative study with Allenspach [54], this substitution is expected to play a role of the flux pinning centers by depressing a local superconducting order parameter. The results have been analyzed by a thermally activated flux creep model [55,56] and the effect of composition on the flux pinning energy has been discussed.

For these purposes, phases have been identified with x-ray powder diffraction (XRD) and analyzed by differential thermal analysis (DTA), scanning electron microscopy (SEM) with energy dispersive x-ray spectrometry (EDS). Optical microscopy and SEM have been used to characterize microstructures. The critical current densities were estimated from hysteretic magnetization measurements with a Quantum Design MPMS SQUID magnetometer. Other magnetic properties such as T_c and magnetic relaxation have been also measured with the SQUID magnetometer. For the structural analysis, some samples were analyzed by neutron diffraction, which was performed in Eidgenössischen Technischen Hochschule (ETH), Zürich in Switzerland.

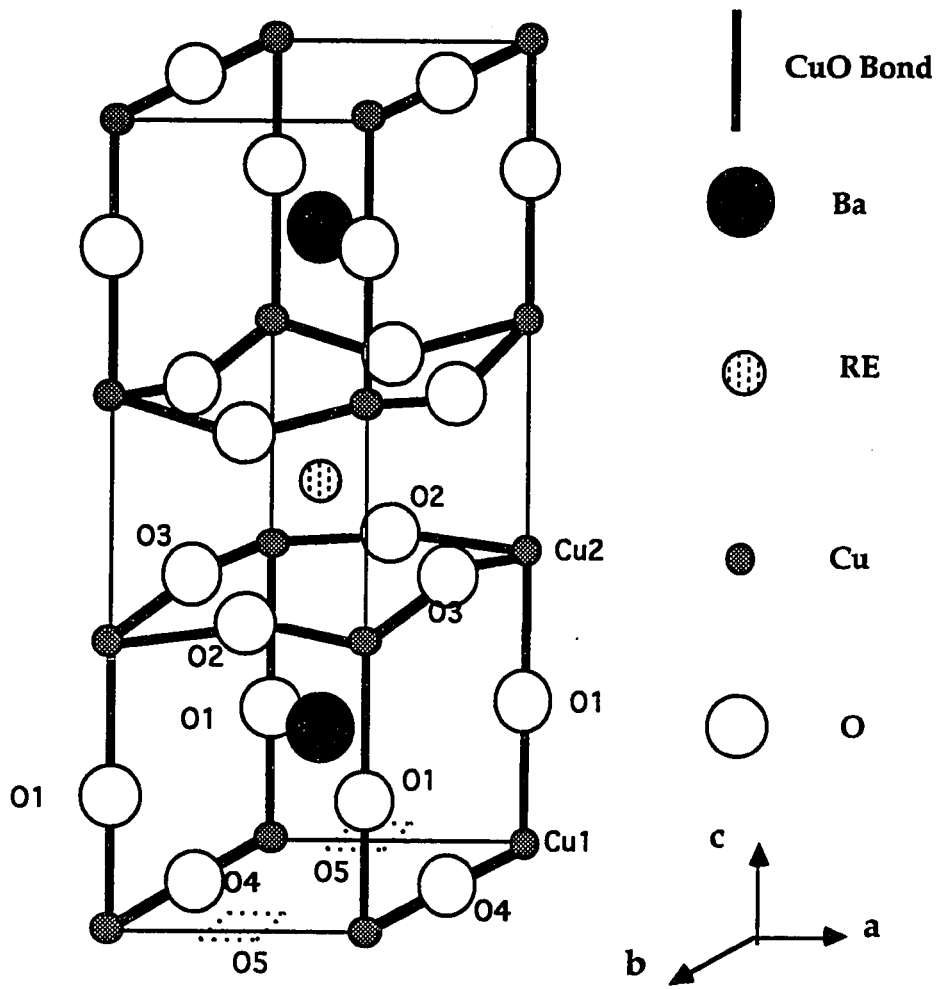

Fig. 2. Structure of RE123 compound. O(5) sites are shown.

PART 1. PHASE DIAGRAM IN THE Nd-Ba-Cu-O SYSTEM

1.1. Introduction

An accurate knowledge of phase equilibria in a given system is necessary for successful materials processing. Such information is conveniently collected in phase diagrams, which are extremely valuable for optimizing thermal processing and crystal growth. It takes a long time (usually, more than several years) to completely work out the phase relationships in a three or more component system if high standards of precision and accuracy are required. Therefore, only portions of specific systems are often investigated for phase relations in that limited portion of the system, which includes phases of interesting chemical or physical properties [57]. This is also the case for the high T_c ceramic superconductors and thus the portions of the equilibrium phase diagrams around $REBa_2Cu_3O_{7-y}$ (RE123), where RE represents lanthanides and yttrium, have been extensively investigated.

For the optimization of the thermal processing in the high T_c ceramic superconductors, an accurate knowledge of the phase relations is crucial. Therefore, it is important to review the thermal processing advanced by the phase diagram investigation in the RE123 superconductors.

It is not simple to produce totally reacted pure RE123 compounds devoid of unreacted starting materials or other impurity phases since many undesirable events may occur during thermal processing. In order to synthesize reproducibly the pure RE123 phase through traditional ceramic processing, two factors must be considered. One is to avoid a liquid phase formation in the sample and the other one is to enhance RE123 phase

stability by controlling ambient atmospheres [58]. First, once a liquid phase forms, more stable RE_2BaCuO_y (RE211) or $RE_4Ba_2Cu_2O_y$ (RE422) phases would preferentially form because of the RE-deficient liquid phase. In this case, it is very difficult to convert RE211 (or RE422) into RE123 via repeated grinding and calcination at low temperature (usually, 890°C in air). In the RE123 phase region on the pseudo-ternary phase diagram of RE_2O_3-BaO-CuO, the ternary eutectic point (e1) is the lowest liquid formation temperature and is strongly dependent on the oxygen partial pressure [3,59]. If the reaction temperature is higher than e1 ($\approx$ 900°C in air), appreciable amounts of the liquid phase can be formed in the sample due to a local inhomogeneous mixture of precursors. At e1, the liquid phase forms through the following reaction; RE123 + $BaCuO_2$ + CuO → L [60]. This RE-deficient liquid phase assists forming RE211 (or RE422) and becomes a major source of impurity phases (mainly, CuO and $BaCuO_2$) segregated on the grain boundaries after subsequent sintering at high temperature. Consequently, the calcination must be performed below the temperature of this invariant point e1 in a given atmosphere. Second, when the precursor includes materials other than oxides, such as $BaCO_3$, the stability boundary of 123 phase as a function of p_{CO2} and temperature must be also considered to prevent 123 phase decomposition [61]. Two important calcination processes for the solid state reaction method, one utilizing dynamic air [58] and the other utilizing a low vacuum dynamic air [62], have been developed. Both methods assure the 123 phase stability by lowering p_{CO2} and enhancing reaction kinetics.

Through the sintering process, the densification is achieved and the microstructure is controlled. Since the sintering temperature should be below the melting point of the material for conventional solid state sintering, the incongruent melting temperatures of RE123 phases as a function of p_{O2} are critical parameters for the determination of the sintering conditions. Especially for Y123, it is well known that liquid formation due to a

ternary peritectic point, p1 (Y123 + CuO → Y211 + L) at about 950°C in air [60] is the main cause for large grain growth and enhanced anisotropic grain morphology [63]. In order to avoid such a liquid phase formation, a nominal composition within the two phase field of RE123 and RE211 (or RE422) solid solutions in the light rare earth systems [1] may be selected. Densification of RE123 usually occurs with grain growth, which is also accelerated by the existence of a liquid phase. In order to prevent microcracks and enhance the mechanical strength, a high density (> 90% theoretical density) with a small average grain size (≈ 1 μm) is required [64]. In such an effort, a transient liquid phase sintering may be applied to control the microstructure of RE123 since the incongruent melting points (m1) of RE123 are different for each rare earth element [3]. For instance, Y123 phase can be used as a transient liquid phase source in the Nd123 matrix because m1 of Y123 is about 100°C lower than that of Nd123.

For the melt processing, such methods as the single crystal growth, liquid-assisted sintering, melt-textured growth, melt-powder-melt-growth (MPMG) process, melt spinning, and plasma spraying are directly related to the phase diagram. Primary phase fields determined by liquidus projections reveal the available composition region for the single crystal growth via a flux growth. Therefore, RE123 single crystals can be grown by selecting a nominal composition within 123 primary phase field [60]. Directional solidification to achieve Y123 grain texturing by Jin et al. [65] utilizes exact information on the liquidus line in the psedo-binary section passing through Y211, Y123 and ($3BaCuO_2$ + 2CuO). For containerless melt processing including melt spinning developed in our group [66], a qualitative understanding of as-dropped phases such as the amorphous or crystalline Nd123 is also possible on the pseudo-binary across Nd211-Nd123-($3BaCuO_2$+2CuO), though those are non-equilibrium products. MPMG processing by Murakami [67] is based on the phase compatibility between Y211 and a ternary liquid

above the Y123 incongruent melting point. In all these processing techniques, the compatibilities between solid and liquid phases are very important to qualitatively understand the final products and hence to choose proper processing parameters, such as composition, temperature, and atmosphere.

In order to fully recover the superconductivity in RE123 ceramics, oxygen annealing is necessary because the samples containing higher oxygen content show better superconductivity. For the optimization of oxygen annealing conditions, the phase stability diagram consisting of composition, temperature, and oxygen partial pressure (x,T, p_{O2}) [68] as well as T-T-T diagram [69] representing oxygenation kinetics is applicable.

Although the superconducting properties of RE123 oxides are known to be minimally affected by complete substitution of lanthanides (except Ce, Pr, Pm., and Tb) for yttrium site [35], the numerous phase diagrams reported in RE-Ba-Cu-O system [1 and references therein] exhibit a significant variation across the lanthanide series. The variation results from differences in compound formation and phase stability. Fundamentally, it is attributed to the difference in the electronic structure, stable valence state, and the size of lanthanide elements.

In the present study, the Nd-Ba-Cu-O system has been investigated. As previously described in the section of the general introduction, Nd123 is an interesting alternative to Y123 for various applications. The information on the phase relationships of this system is, however, rather limited and controversial. No pseudo-binary phase diagram on Nd_2O_3 - BaO has been reported. In addition, several studies [1,70,71] reporting on the subsolidus phase relationships in the Nd-Ba-Cu-O system display significant discrepancies. These discrepancies involve the formation of pseudo-ternary compounds, solid solution range, and compatibility triangles.

In order to clarify such discrepancies, the phase compatibilities surrounding Nd123

phase at 890°C in air have been investigated by powder XRD, DTA, and SEM. Especially, since the tie lines in the BaO-rich region of the subsolidus phase diagram are uncertain even in Y system, more attention has been paid to this region. In addition, the effect of oxygen partial pressure on the phase stabilities has been also investigated with DTA. The results are presented as a pseudo-ternary subsolidus phase diagram. This phase diagram is compared with previously published results of the same system and that of the Y-Ba-Cu-O system. The experimental criterion for the actual attainment of an equilibrium state within a system was based on the consistency of phase properties with the passage of time (so called the time criteria). In a special case, different procedures criterion (i.e., producing phases having the same properties when the same conditions are reached by different paths) was used.

1.2. Experimental Procedures

Various samples with nominal compositions around the Nd123 compound in the Nd_2O_3 - BaO - CuO pseudo-ternary system, were prepared by the conventional ceramic processing. Powders of Nd_2O_3 (99.997%), CuO (99.999%), and $BaCO_3$ (99.78%) were used as starting precursors. The precursor materials were dried in air with the following conditions; Nd_2O_3 at 1000°C for 3 days, $BaCO_3$ at 750°C for 2 days, and CuO at 550°C for 5 days. All powders were passed through 100 mesh (150 μm) sieve. When the starting Nd_2O_3 powder was dried at 700°C, while this temperature is high enough to completely dry Y_2O_3 powder, it turned out to be insufficient to dry Nd_2O_3. Subsequent drying of the Nd_2O_3 for 24 hours at 950°C followed by 10 hours at 1000°C resulted in additional 1.25 % average weight loss. The starting powders were carefully weighed, mixed, and then ground with a Brinkman micromill in a dry nitrogen glove box. Finely

mixed powders were pressed into pellets and placed on MgO single crystals to be calcined at 890°C for 24 hrs in flowing air (flow rate = 10 *l*/min) and then quenched to room temperature in air. Samples were reground with a micromill and reacted at least twice to facilitate the reactions. In order to obtain equilibrium phases, several subsequent reactions in flowing air, containing a low CO_2 content (CO_2 < 3 ppm) (hereafter, it will be called CO_2-free air), were required for the compositions in the BaO-rich region. The CO_2 concentration of natural air was reduced to < 3 ppm by using a commercial filter. Some compositions studied were prepared by mixing as-calcined compounds. The nominal compositions of the samples chosen for the present study are shown in Table 1.1. The compositions are given in cation mole fractions. In this way the compositions can be easily located on a ternary diagram if the compositions in the diagram are mole fractions of BaO, CuO, and 1/2 Nd_2O_3.

Phase identification was carried out via powder XRD on a diffractometer with CuKα radiation and a graphite diffracted beam monochrometer. Subsolidus phase relations were established by XRD characterization with the aid of JCPDS (Joint Committee on Powder Diffraction Standards) and lattice parameters were determined by using a linear least square method [72]. Because of the moisture-sensitive nature of specimens, quenched samples were stored in a desiccator and analyzed as soon as possible after final firing.

The thermal stabilities of compounds were analyzed by DTA in three different partial oxygen atmospheres; 100% O_2, 1% O_2 in Ar, and 0.1% O_2 in Ar. DTA experiments were performed in high purity Al_2O_3 sample cups with a Perkin Elmer 1700 Thermal Analysis System. Heating rate was 10°C/min for all DTA runs, and Al_2O_3 powder was used as the reference material. All cycles were performed in flowing gas (flow rate = 50 *ml*/min). The temperatures of thermal events are reported as the onset

Table 1.1. The nominal compositions and phases observed at 890°C in air in the Nd-Ba-Cu-O system.

Sample No.	Nominal Compositions Nd	Ba	Cu	Phases observed		
1	5	28	67	123,	011	CuO
2	15.1	21.2	63.7	123ss,	CuO	
3	22	21	57	123ss,	CuO	
4	34.7	9.9	55.4	123ss,	201,	CuO
5	40	10	50	201,	123ss	CuO
6	57.1	3.6	39.3	201,	123ss	CuO
7	33.3	0	66.7	201,	CuO	
8	30	20	50	123ss,	201,	CuO
9	63.3	3.3	33.3	201,	422,	123ss
10	66.7	0	33.3	201		
11	61.1	8.3	30.5	201,	422	
12	60	20	20	422,	Nd_2O_3	
13	50	25	25	422		
14	46.2	23.1	30.8	422,	123ss,	201
15	40	20	40	123ss	422,	201
16	30.5	21.2	48.3	123ss,	201	
17	46.2	30.8	23.1	422ss		
18	16.7	33.3	50	123,	011	
19	18.3	31.7	50	123ss		
20	20.8	29.2	50	123ss		
21	25	25	50	123ss(336)		
22	20.1	32	47.9	123ss,	422ss	
23	23	31.3	45.7	123ss,	422ss	
24	25.9	28.4	45.6	123ss,	422ss	
25	10	60	30	163,	unknown minor phase	
26	12.5	50	37.5	163,	123	
27[a]	16.7	50	33.3	163,	422ss,	(123)
28[b]	18.2	40.9	40.9	123,	422ss	163, (011)
29[c]	21.5	37.5	41	123,	422ss	163, (011)
30	7.7	61.5	30.8	163,	unknown minor phase	
31	0	50	50	011		
32	8	42	50	123,	011	
33	11	47	42	163	123,	011

123ss = $Nd_{1+x}Ba_{2-x}Cu_3O_{7+\delta}$, 336 = $Nd_3Ba_3Cu_6O_{7+\delta}$,
123 = $NdBa_2Cu_3O_7$; tentatively, x=0.04 in Nd123ss
422ss = $Nd_{4-2x}Ba_{2+2x}Cu_{2-x}O_{10-2x}$, 422 = $Nd_4Ba_2Cu_2O_{10}$
011 = $BaCuO_2$, 201 = Nd_2CuO_4, 163 = $NdBa_6Cu_3O_y$

a ; 123 phase is hardly discernable on XRD pattern.

b, *c* ; 011 phase still exists after repeated reactions for total 168 hours, but relative peaks of 011 phase slowly decrease as those of 123 phase slowly increase.

For samples from No. 25 to 33, CO_2-free air (CO_2 < 3 ppm) was employed.

temperatures. Sample compositions containing relatively large amounts of barium were found to wet the Al_2O_3 cup after melting. Other compositions did not interact with the Al_2O_3, forming an easily removable ball in the center of the cup. The solubility limits were determined by XRD and DTA. SEM examination of polished samples was carried out at an accelerating voltage of 15 KV and beam current of 20 mA.

1.3. Results and Discussion

The sample compositions studied are listed in Table 1.1. Provided are the starting nominal compositions and phases observed in the resulting materials by powder XRD. Since CO_2 partial pressure affects the phase stability of oxide compounds as well as the O_2 partial pressure [61], reaction was repeated until $BaCO_3$ was completely decomposed below the resolution limit of DTA. DTA was employed to detect minor amount of residual $BaCO_3$, which is undetectable by XRD, by way of the endothermic peak at 820°C due to the structural transition ($\gamma \rightarrow$ ß). For the BaO-poor region (BaO < 35 mole %), two calcination reactions at 890°C for 24 hours with intermediate micromilling were sufficient to fully decompose $BaCO_3$ in the samples. However, for the BaO-rich region (BaO > 35 mole %), extended calcination was required to achieve the complete decomposition of $BaCO_3$.

The importance of complete decomposition of $BaCO_3$ is clearly shown in Fig. 1.1 for example. The XRD patterns for the sample No. 27 in Table 1.1 were obtained from the air-quenched products after 24, 72, 120, and 168 hours respectively. After the first reaction, the peaks of unreacted $BaCO_3$ are still fairly high as shown in Fig. 1.1(a). Other major phases are composed of Nd123 and an unidentified phase which is presumed to be Nd143 oxycarbonate phase. After the second reaction, $BaCO_3$ is reduced to a minor phase

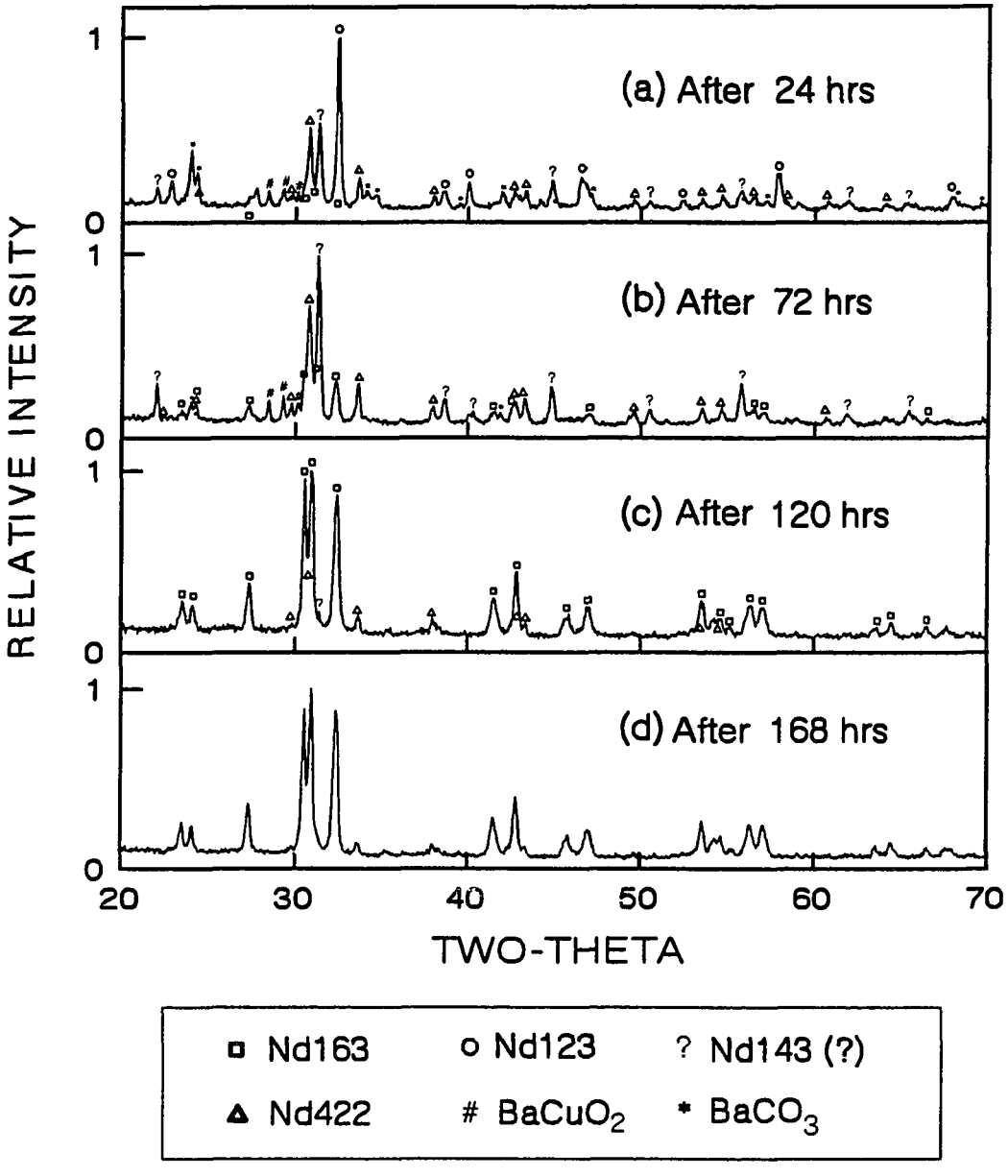

Figure 1.1. XRD patterns for a sample with the nominal composition of Nd : Ba : Cu = 1 : 3 : 2 in BaO-rich region after subsequent reactions for (a) 24 hrs (b) 72 hrs (c) 120 hrs (d) 168 hrs at 890°C in flowing CO_2-free (<3ppm) air.

as shown in Fig. 1.1(b). Nd143 and Nd211 phases become major phases but Nd123 becomes a minor phase as well as $BaCuO_2$ (011) phase and the second unknown phase which will be analyzed as Nd163 phase later. After long-term reaction (168 hrs), $BaCO_3$ phase is no longer detectable via DTA as well as XRD as shown in Fig. 1.1(c). Unexpectedly, the XRD pattern once again drastically changes so that the presumed Nd143 oxycarbonate phase almost disappears. Final products are mainly composed of Nd163 phase with minor Nd211 and Nd123 phases. As shown in Fig. 1.1(d), further reaction confirms that these oxides are equilibrium phases at 890°C in CO_2-free air. Such an abrupt change was commonly observed in the compositions of BaO-rich region but not in BaO-poor region. Consequently, it must be related to the decomposition of $BaCO_3$.

The above reaction path could be qualitatively understood as follows; stagnant CO_2 gas evolved from $BaCO_3$ during heat treatment would sustain relatively high CO_2 partial pressure within a pelletized sample so that relatively stable phases form preferentially at a given local CO_2 partial pressure. As will be discussed later, the presumed Nd143 phase may be stable only in a relatively high CO_2 atmosphere and probably forms the oxycarbonate-type compound. For further understanding, a stability phase diagram for Y123 reported by Fjellvag et al. [61] is reproduced in Fig. 1.2. Points A and B in this figure represent the *in situ* conditions at 890°C in natural air ($CO_2 \approx 300$ ppm) and in CO_2-free air ($CO_2 \approx 3$ ppm) by using a commercial filter, respectively. According to this diagram, point A is so close to the $BaCO_3$ stability boundary that the decomposition reaction in natural air will be more sluggish than for point B. Consequently, both reduced CO_2 partial pressure and flowing air (flow rate of 10 *l*/min) must increase the reaction rate by increasing the decomposition rate of $BaCO_3$.

In order to avoid the CO_2 effect, many authors have employed CO_2-free materials such as BaO, BaO_2, $Ba(NO_3)_2$, and $Ba(OH)_2$ as precursors. In this case, the reaction time

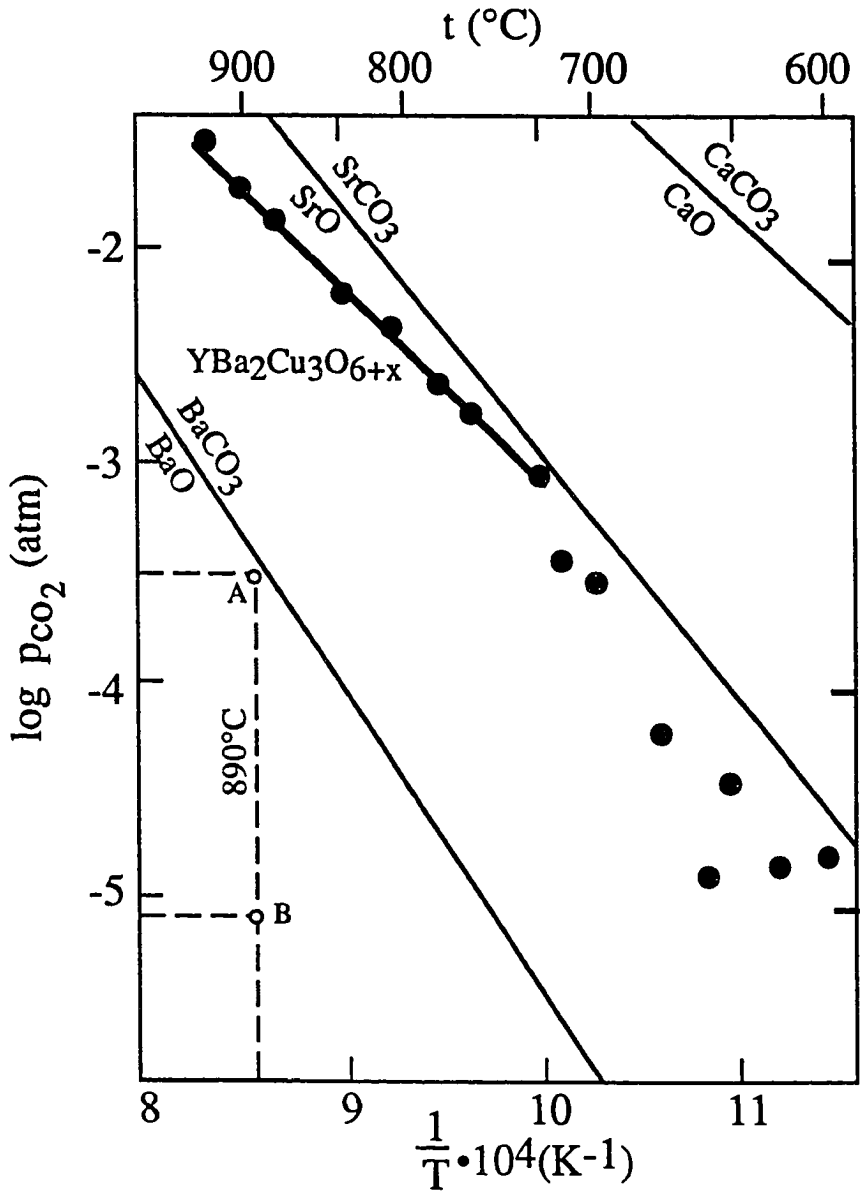

Figure 1.2. The stability phase diagram via p_{CO2} versus 1/T reproduced from Fjellvag et al. [61]. The points A and B represent the positions of natural air (CO_2 $\approx$ 300 ppm) and CO_2-free air (CO_2 $\approx$ 3 ppm) at 890°C, respectively.

must be shortened. However, such compounds are commonly unstable in air and hence the purity is questionable. Moreover, if samples are reacted in air, the CO_2 effect is unavoidable since the average CO_2 content in air is about 300 ppm (p_{CO2} = 3 x10^{-4} atm). A significant effect of CO_2 in natural air on the phase formation has been recently reported by Osamura et al. [73] in the Y-Ba-Cu-O system. According to their results, Y184 is stable in natural air but Y163 and Y143 are stable in artificial air (CO_2 < 1 ppm) at 990°C. In order to determine the pseudo-binary phase diagram in air (i.e. at p_{O2} = 0.2 atm), CO_2 should be, therefore, minimized in the reaction since it would make this system pseudo-quaternary.

The Binary Systems

BaO-CuO

The following five pseudo-binary compounds: $BaCuO_2$, Ba_2CuO_3, Ba_3CuO_4, $BaCu_2O_2$, and a compound with a composition in the vicinity of $Ba_3Cu_5O_{8+\delta}$ have been reported in the Ba-Cu-O system. The compound $BaCuO_2$ is well characterized [74], cubic, I432, a = 18.2855(3). In the present study, a single phase of this compound was readily formed from the stoichiometric mixture of $BaCO_3$ and CuO after several repeated reactions.

The compound Ba_2CuO_3 was first reported by Wang et al. [75]. They argued that the Ba_2CuO_3 compound could not be produced without a $LiCO_3$ mineralizer at 950°C in air because of partial melting. However, without using $LiCO_3$ mineralizer, Frase et al. [76] could prepare the compound Ba_2CuO_3 by using barium oxide (BaO) rather than barium carbonate. The material was described as hygroscopic and decomposing during analysis and above 850°C. Frase et al. suggested that reaction rates were much quicker

when they used barium oxide as a reagent rather than barium carbonate. This difference in reaction rate was understood on the basis of relative stability of the carbonate compared to the oxide. Later, Abbattista et al. [77] recognized the importance of avoiding CO_3^{-2} pollution from natural air as well as from carbonate. By using $BaCuO_2$ and BaO, they ascertained the existence of a dimorphase, $Ba_2CuO_{3+\delta}$ in CO_2-free (CO_2 < 1ppm) air or oxygen. They also noticed that this phase showed a phase transition at 740°C from tetragonal structure of a K_2NiF_4-type to orthorhombic structure derived from that of Sr_2CuO_3. The same phase transition was also observed occurring at 810°C by Zhang and Osamura [78]. In addition, DeLeeuw et al. [79] found that this compound decomposed above 850°C and to melt partially at 950°C.

The compound Ba_3CuO_4 first suggested by Frase et al. [76] has been reproduced by Abbattista et al. [77] in a low ambient partial oxygen atmosphere ($P_{O2} = 10^{-6}$ atm). This material has a rhombohedral symmetry and is isostructural with Ba_3NiO_4. Another compound with the composition in the vicinity of $Ba_3Cu_5O_{8+\delta}$ was found by Roth et al. [80] in the CuO-rich part of the binary system. This compound could be made at temperatures up to 800°C in an ambient of oxygen. They reported that this compound decomposed into $BaCuO_2$ and CuO at higher firing temperatures. At low firing temperatures, the compound $Ba_3CuO_{8+\delta}$ was also made preferably starting from BaO_2 or $Ba(NO_3)_2$. However, all these phases must be unstable in air or higher partial oxygen atmosphere (i.e., $P_{O2} > 0.21$ atm).

The compound $BaCu_2O_3$ was prepared by Teske and Müller-Buschbaum [81] from the oxides at 900°C in Ar. According to their structural analysis, $BaCu_2O_3$ crystallizes in a tetragonal unit cell, space group I41/amd, with a = 5.72 Å and c = 10.06 Å. This compound is also strongly hygroscopic and readily found in as-quenched materials of RE123 melts [66].

Following the above literature survey, only $BaCuO_2$ and Ba_2CuO_3 are stable pseudo-binary phases in the present experimental condition. Therefore, except $BaCuO_2$, further investigations to conform the stable binary oxides in the Ba-Cu-O system have not been performed in the present study.

BaO-Nd_2O_3

Lopato [82] reported extensive work on RE_2O_3 - BaO systems, showing the existence of $RE_4Ba_3O_9$ from Sm to Lu, including Y and Sc, and RE_2BaO_4 from La to Er. All of these compounds were moisture-sensitive. In the pseudo-binary Y_2O_3-BaO, $Y_2Ba_2O_5$ and $Y_2Ba_4O_7$ compounds suggested by Roth et al. [80] were analyzed to be oxycarbonates later [83]. It was also reported that the RE_2BaO_4 (RE = La, Pr) compounds melted incongruently while the Nd_2BaO_4 and Sm_2BaO_4 melt congruently at very high temperatures (above 1900°C). In addition, the compound Nd_2BaO_4 was also identified by Hodorowicz et al. [71] at 950°C in air. Therefore, Nd_2BaO_4 is considered to be the only stable phase in the present experimental condition. However, the BaO-rich part of the psudo-binary Nd_2O_3-BaO is not unambiguous because of a potential CO_2 effect as discussed in the Ba-Cu-O system.

CuO-Nd_2O_3

It is well known that the pseudo-binary compounds with a general formula RE_2CuO_4 are formed for RE = La, Pr, Nd, Sm, Eu, and Gd (i.e., light rare earth elements except Ce and Pm). On the contrary, $RE_2Cu_2O_5$-type formula is common to heavy rare earths (Dy to Lu except Tb). At very low partial oxygen atmospheres, compounds with $RECuO_y$-type formula are sometimes reported in the whole lanthanide series [1]. Not all RE_2CuO_4 phases are isostructural. La_2CuO_4 is orthorhombic with

space group Fmmm, and has the distorted K_2NiF_4 type structure. All other RE_2CuO_4 compounds are tetragonal with space group P4/mmm. These structures do not resemble the K_2NiF_4 type but have a coplanar Cu-O layer similar to that found in CaF_2-type structure. The single Nd_2CuO_4 compound was prepared in the present study and no other pseudo-binary compounds were observed.

The ternary system : Nd_2O_3-BaO-CuO

The results of the x-ray analyses listed in Table 1.1 were used for the determination of the subsolidus phase compatibilities around Nd123 as shown in Fig. 1.3. The Nd_2O_3 formula unit is halved so that composition ratios correspond to cation ratios. The principal findings, described below, are the compatibility triangles (or Gibbs triangles), a previously unreported pseudo-ternary compound of $NdBa_6Cu_3Oy$, and the existence of the solid solutions of $Nd_{1+x}Ba_{2-x}Cu_3O_{7+\delta}$.

The subsolidus phase compatibilities at 930-950°C in air in the Nd-Ba-Cu-O system have been reported by several groups [1,70,71]. The present results are in good agreement with that of Wong-Ng et al. [1] for BaO-poor (Ba < 35%) region, but not those of other groups in the compatibility triangles. The subsolidus phase diagram over the full composition region was reported only by Hodorowicz et al. [71]. However, significant discrepancies from their results could be found in the present study. Firstly, they reported the existence of a new pseudo-ternary line compound, Nd311, instead of Nd422. Secondly, a tie line was drawn between BaO and Nd123 in their diagram. In this study, the nominal composition of Nd : Ba : Cu = 3 : 1 : 1 (sample No. 12 in Table 1.1) had been also selected but the reacted product was analyzed to consist of two phases, Nd422 and Nd_2O_3 instead of a single phase as shown in Fig. 1.4. It was also confirmed

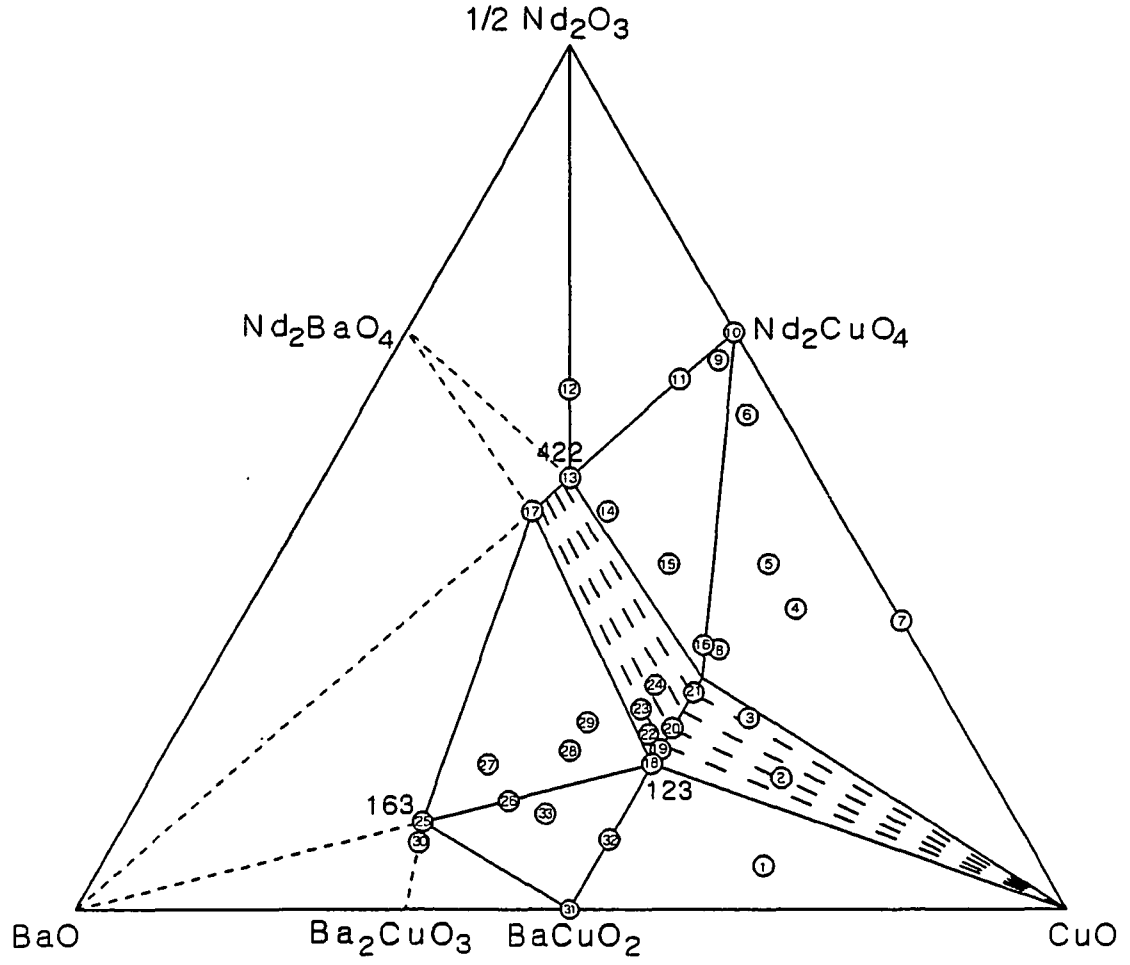

Figure 1.3. Subsolidus phase diagram of the system Nd_2O_3-BaO-CuO at 890°C in air. The triangles including the dashed lines were not experimentally determined. The shaded regions by the broken lines indicate two phase fields. The numbers on the points correspond to those listed in Table 1.1.

by SEM and energy dispersive x-ray spectrometry (EDS) analysis. Their confusion might be originated from the overlapping of major peaks between those two phases. Moreover, as reported by Wong-Ng et al. [1], Nd422 compound was found to have solid solution though its solubility limit was relatively narrower (<0.2) than that of Nd123.

Careful sample preparation as described above enabled the synthesis of a new compound, Nd163 at 890°C in CO_2-reduced air. Additional experiments showed that it was also stable up to 950°C in air. Fig. 1.5 shows the XRD pattern for Nd163. The peaks were indexed by using orthorhombic structure with the cell parameters of a= 3.886(2), b= 3.984(2), c= 13.001(5) Å with the error of fit, R = 3.553 %. Observed and calculated interplanar spacings are listed in Table 1.2. Consequently, Nd123 must be compatible with Nd163 and not with BaO. As previously discussed, their failure to synthesize this compound might be due to inefficient removal of CO_2 gas evolved from the $BaCO_3$ within the sample. More detailed structural analysis on Nd163 was not performed in the present study. During the formation of Nd163, a new transient phase presumed to be Nd143 oxycarbonate could be also observed in Fig. 1.1(b), which eventually disappeared.

It is also interesting to compare the Nd system with other RE (and Y) systems. One of the apparent differences between the Nd and Y (or heavy rare earth) system is in their relevant single phases as summarized in Table 1.3. Since Y system has been more extensively studied, it is instructive to compare the phases involved and their relationships of Nd system with Y system. For compounds, Nd201(black), Nd422(brown; solid solution), and Nd123(extensive solid solution) exist instead of Y202(blue), Y211(green), and Y123(line compound) respectively. Another difference comes from the existence of two phase fields in the Nd system such as 123ss - 422ss (up to m1) and 123ss - CuO (up to p1) due to the formation of Nd123 solid solution. As mentioned in the previous section,

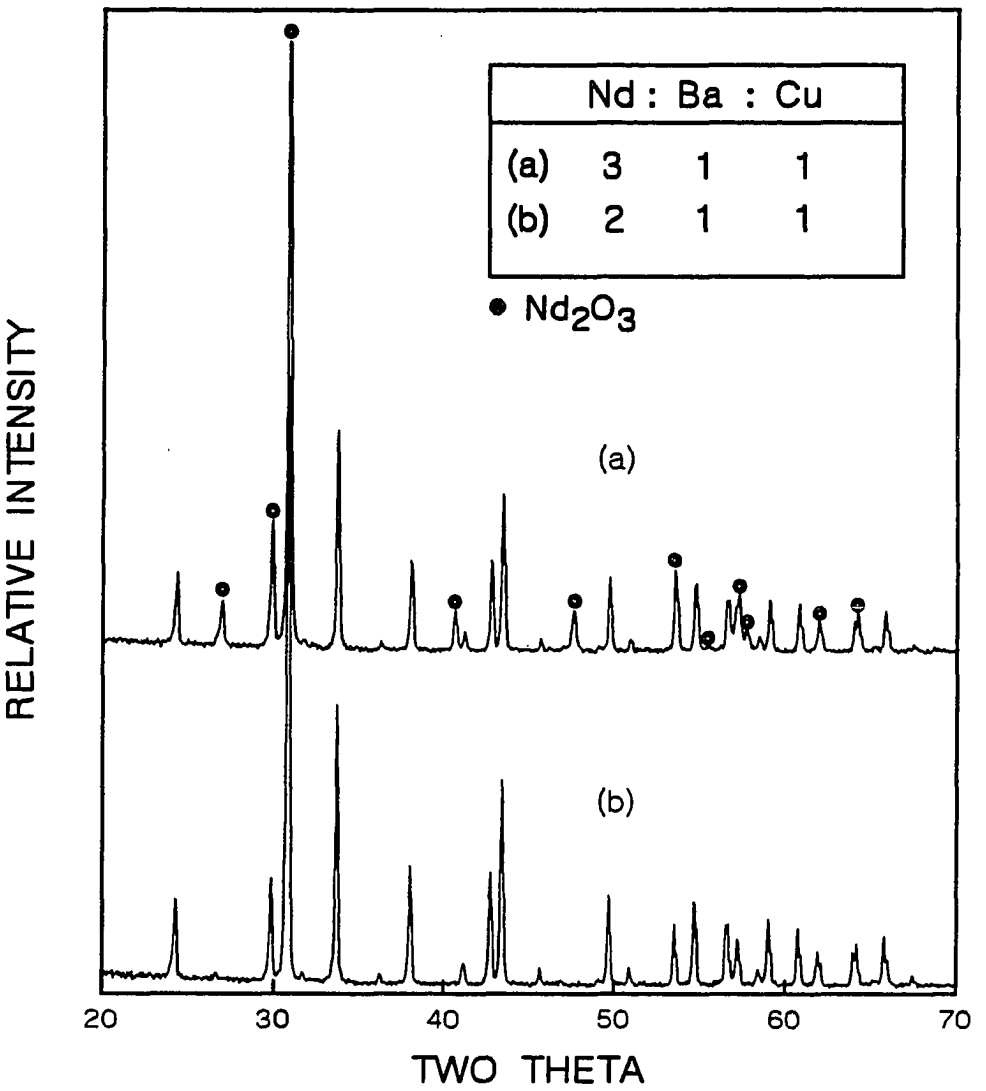

Figure 1.4. XRD patterns for the samples with the nominal compositions of Nd : Ba : Cu = (a) 3 : 1 : 1 and (b) 2 : 1 : 1, respectively.

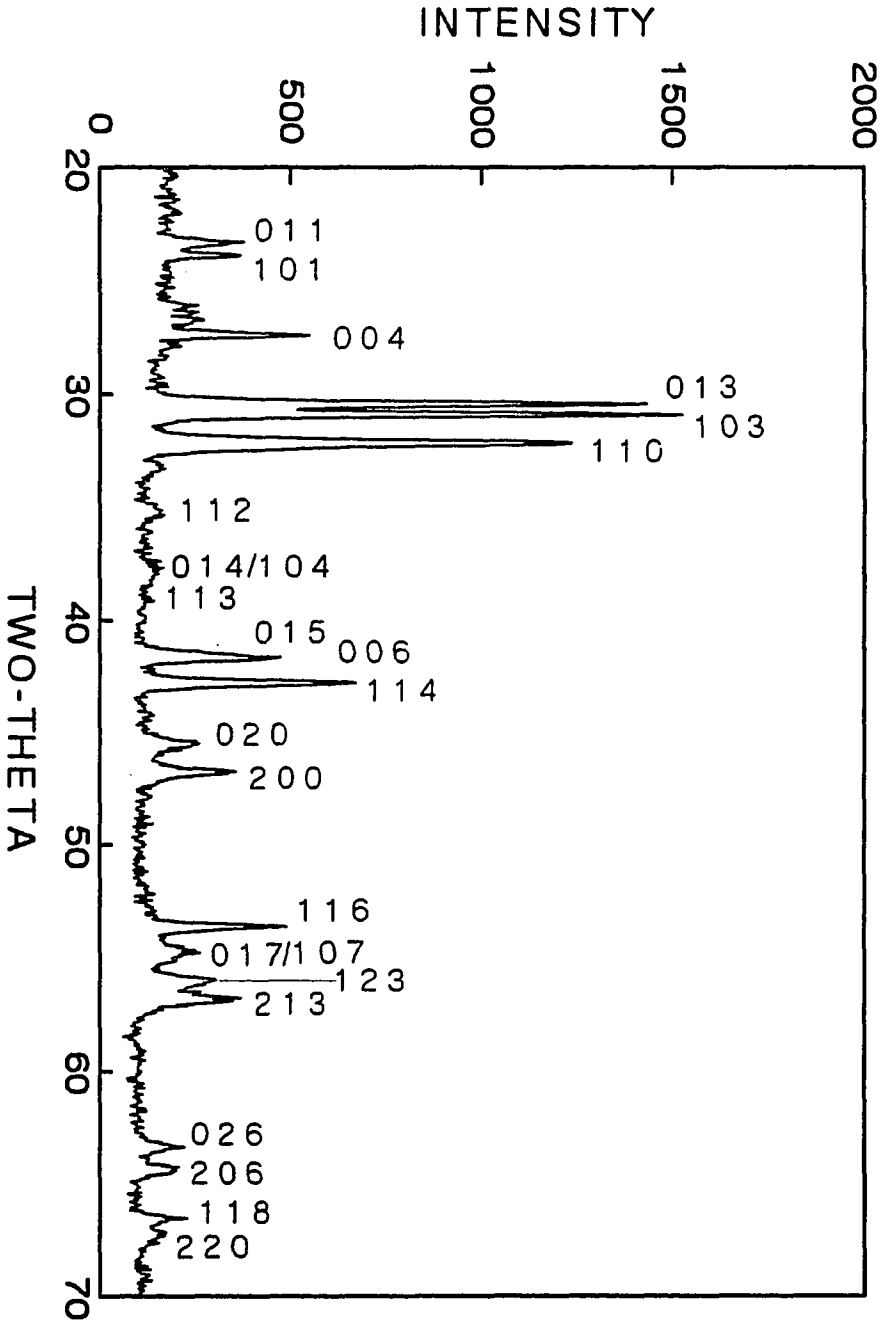

Figure 1.5. XRD patterns and indices for a new compound $NdBa_6Cu_3O_y$.

Table 1.2. Observed interplanar spacings for $NdBa_6Cu_3O_y$ are excellently matched with calculated ones. The XRD peaks are indexed via the orthorhombic crystal system and the unit cell parameters are given to be a= 3.8858(17) Å, b= 3.9843(18) Å, and c= 13.0014(52) Å.

No.	d_{cal}(Å)	h k l	d_{obs}(Å)
1	3.8094	0 1 1	3.8128
2	3.7231	1 0 1	3.7262
3	3.2504	0 0 4	3.2538
4	2.9331	0 1 3	2.9355
5	2.8931	1 0 3	2.8956
6	2.7818	1 1 0	2.7840
7	2.1669	0 0 6	2.1689
8	2.1135	1 1 4	2.1156
9	1.9921	0 2 0	1.9939
10	1.9429	2 0 0	1.9446
11	1.7095	1 1 6	1.7110
12	1.6408	1 2 3	1.6423
13	1.6198	2 1 3	1.6211
14	1.4666	0 2 6	1.4679
15	1.4466	2 0 6	1.4479
16	1.4033	1 1 8	1.4045

Table 1.3. Summary of Phase Formation in the BaO-R_2O_3-CuO systems referred to W. Wong-Ng et al. [1].

R^{3+} =	La	Nd	Sm	Eu	Gd	Dy	Ho	Y	Er	Tm	Yb	Lu
R_2O_3 - CuO :												
R_2CuO_4 [a]	T	T	T	T	T	O	O	O	O	O	O	O
$R_2Cu_2O_5$ [b, c]	O	O	O	O	O	T	T	T	T	T	T	T
R_2O_3 - BaO :												
R_2BaO_4 [d]	T	T	T	T	T	T	T	T	T	O	O	O
$R_4Ba_3O_9$	O	O	T			T	T					
$R_2Ba_2O_5$	O	O	O									T
$R_2Ba_4O_7$	O	O	O									T
R_2O_3 - BaO - CuO :												
$RBa_2Cu_3O_{6+x}$ [e]	T	T	T	T	T	T	T	T	T	T	T	T
R_2BaCuO_5 green phase [f]	O	O	T	T	T	T	T	T	T	T	T	T
$R_{4-2x}Ba_{2+2x}Cu_{2-x}O_{10-2x}$ brown phase [f]	T	T	O	O	O	O	O	O	O	O	O	O
$R_{1-x}Ba_{3+x}Cu_{2-z}O_{6.4-z}$ [e]	O	O						T	T			
$R_4BaCu_5O_{13+x}$ [g, h, i]	T	O	O	O	O	O	O	O	O	O	O	O
$R_3Ba_3Cu_6O_{14+x}$ [j]	T	T	T	T	O	O	O	O	O	O	O	O
$R_{2-x}Ba_{1+x}Cu_2O_{6-x/2}$	T	O	O	O	O	O	O	O	O	O	O	O

a. Von Hk. Muller-Buschbaum and W. Wollschlager, Z. Anorg. Allg. Chem. **414**, 76 (1975).

b. H. -R. Freud and Hk. Müller-Buschbaum,.Z. Naturforsch **32B**, 609 (1977).

c. E. Lambert, JCPDS Grant-in-Aid Report, (1981) and (1982).

d. W. Wong-Ng, and B. Paretzkin, to be submitted to Powd, Diff., (1989).

e. W. Wong-Ng, H.F. McMuridie, B. Paretzkin, M. Kuchinski, and A.L. Dragoo, Powd. Diff. 2[3], 191 (1987) ; 2[4], 257 (1987) ; 3[1] 47 (1988) ; 3[2], 113 (1988) ; 3[3] 179 (1988) ; 4[1], 40 (1989) ; 4[2], 106 (1989).

f. W. Wong-Ng, M.A. Kuchinski, H.F. McMuride, and B. Paretzkin, Powd. Diff., 4[1], 1 (1989).

g. C. Michel, L. Er-Rakho, and B. Raveau, Mater. Res. Bull. **20**, 667 (1985).

h. C. Michel, L. Er-Rakho, M. Hervieu, J. Pannetire, and B. Raveau, J. Solid State Chem. **68**, 143 (1987).

i. F. Herman, Phys. Rev. B **37**, 2309 (1988).

the existence of 123ss - 422ss two phase field enables us to select a starting composition that leads to 123-422 composites completely devoid of minor second phases such as 011 and 001 which segregate at 123 grain boundaries after a solid state sintering. The same type of compounds and two phase fields are, however, commonly observed in the light rare earth elements except Ce, Pr, and Pm [1], in which only the solubility limits of RE123ss and RE422ss (no solid solution for RE = Sm, Eu, and Gd) are different. In addition, the incongruent melting point (m1) for Nd123 is about 100°C higher than that of Y123.

The solubility limit of Nd123ss was $0.04 \leq x \leq 0.6$ for the present experimental conditions. The lower solubility limit has been extensively studied because it is directly related to the high T_c (> 90 K) phase. The lower limit was best determined to be x= 0.04 compared to values of x = 0 by Wong-Ng et al. [1] or x = 0.1 by Zhang et al. [70]. The small peaks of 011 phase on the x-ray diffraction disappear only after the same sample is reacted in low partial oxygen atmospheres such as 1% O_2 in Ar ($P_{O2} = 10^{-2}$ atm) or in Ar as shown in Figure 1.6. DTA and careful metallographic analyses showed no minor 011 phase for the samples of $x \geq 0.04$ which were sintered at 1050°C in pure oxygen. This suggests that it is probably impossible to fabricate stoichiometric Nd123 in air or pure oxygen atmosphere (i.e. at high oxygen partial pressure) as in the case of La123 [84]. Therefore, stoichiometric Nd123 (i.e., x= 0) is considered to be unstable in air or pure oxygen atmosphere and stable only at a low p_{O2}. As shown in Fig. 1.7, the upper limit is x= 0.6., which is similar to x= 0.7 reported by Wong-Ng et al. [1] at 950°C in air, but much smaller than x= 1 reported by Sujia et al. [85] at 930°C in air.

In the case of Nd422ss, acceptable experimental data for the solubility limit have not been reported. Wong-Ng et al. [1] just suggested the solubility limits $0 \leq x \leq 0.1$. However, since our XRD pattern of a sample composition x = 0.2 shows negligibly small

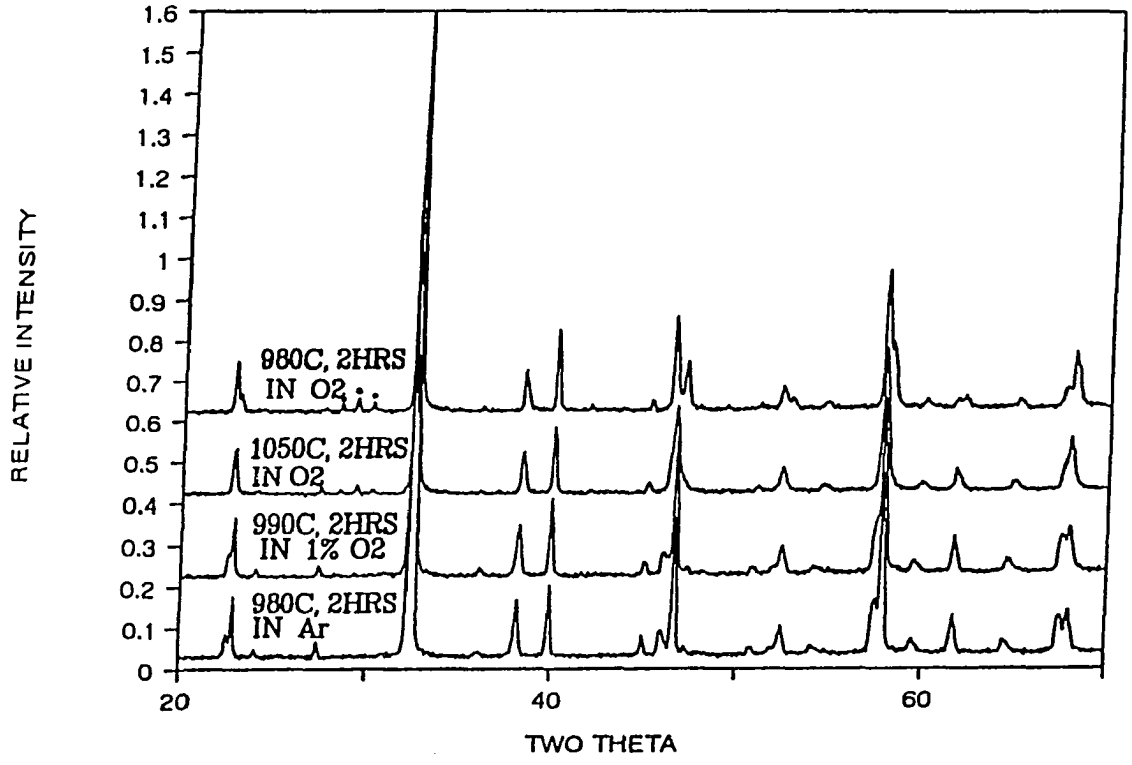

Figure 1.6. XRD patterns for the Nd123 sample reacted in different oxygen atmospheres. The small peaks of minor $BaCuO_2$ phase are observed for the sample reacted in pure oxygen but not in low oxygen atmospheres.

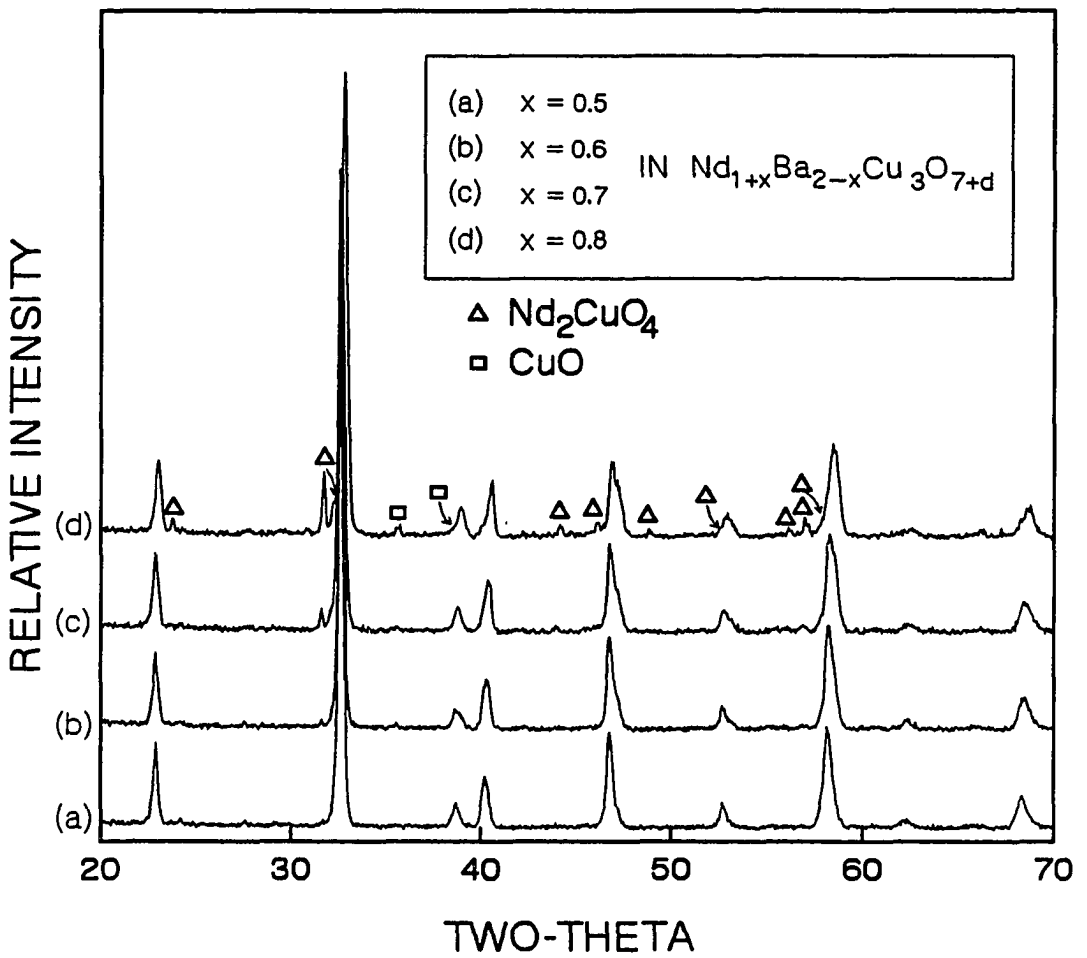

Figure 1.7. XRD patterns for the samples with the nominal compositions of x = 0.5 (a), 0.6 (b), 0.7 (c), 0.8 (d) in $Nd_{1+x}Ba_{2-x}Cu_3O_{7+\delta}$ after air-quenched from 890°C.

impurity peaks, x= 0.2 was taken as the upper limit. For Nd201ss, the sample having the nominal composition of 2.5 % Ba on Nd site still showed minor Nd211 phase. Therefore, the solubility limit is very narrow below 2.5 % if it exists.

Further experiments have been performed to investigate the effect of oxygen partial pressure on the solubility limit and phase stabilities of Nd123 solid solutions. Fig. 1.8 presents the results of DTA in different ambient oxygen partial pressure. As the oxygen partial pressure is reduced, the incongruent melting points (m1) of all compositions decrease. However, the decrease for larger values of x (i.e., more Nd substitution for Ba site) is more abrupt. The above result also suggests that the Ba substitution for Nd site (i.e., $x < 0$) can occur in lower partial oxygen atmosphere.

1.4. Conclusion

The solid phase relations around the Nd123 compound of the Nd_2O_3-BaO-CuO ternary diagram have been investigated at 890°C in air by selecting various nominal compositions in order to identify the subsolidus phase diagram in this region. The unpublished new ternary compound Nd163 was found to be a stable phase at 890 and 950°C in air and compatible with Nd123, Nd422, and 011 phases. The formation of Nd163 compound establishes the compatibility triangles in the region. The solubility limit of Nd123ss is $0.04 \leq x \leq 0.6$ at 890°C in air. Since BaO is unstable in air due to the moisture of $H_2O + CO_2$, further study on the solid phase relationships in the BaO-rich corner will be required, avoiding exposure to CO_2 gas during the preparation of samples. As the oxygen partial pressure is reduced, Nd123 solid solution phases having higher Nd concentration on Ba sites become less stable and Ba substitution on Nd site is presumed to occur. However, this new type of solid solution needs more investigation.

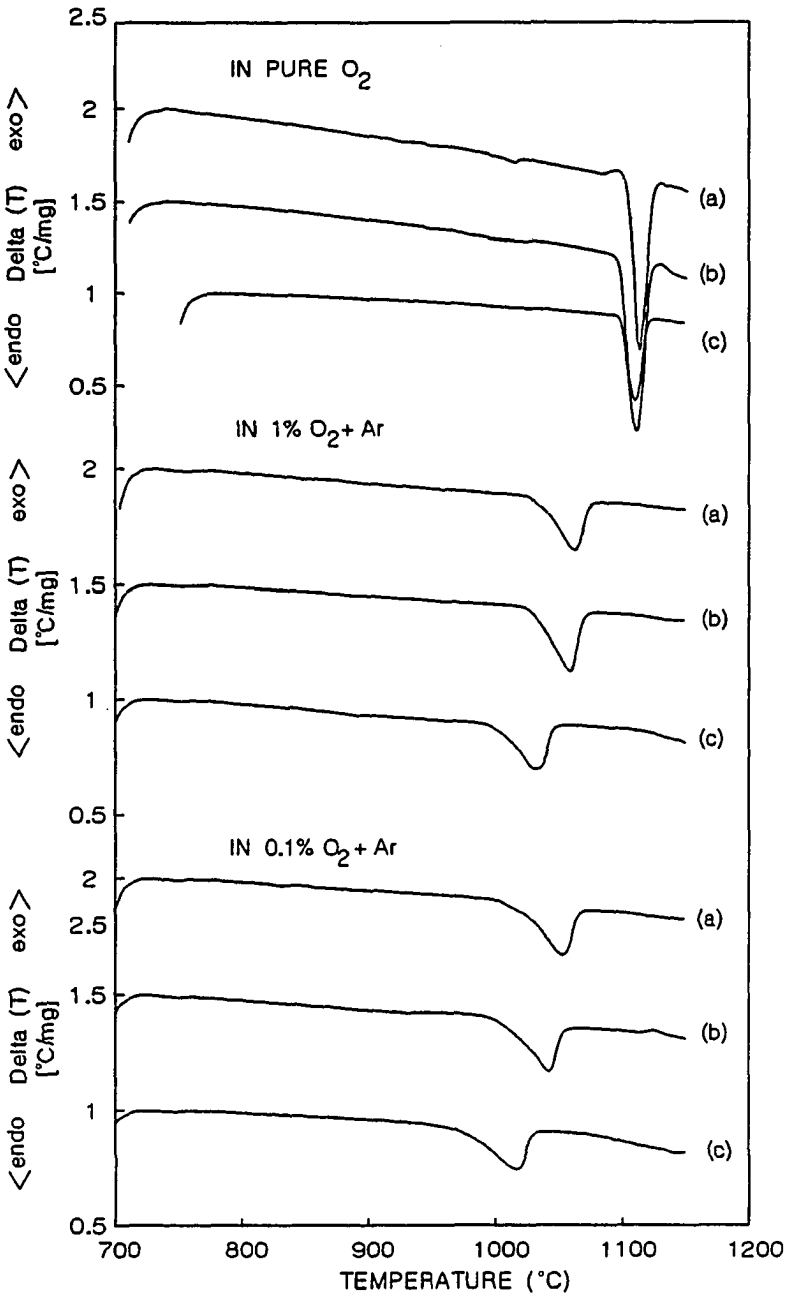

Figure 1.8. DTA curves in different partial oxygen atmospheres for x = 0 (a), x = 0.25 (b), and x = 0.5 (c) in $Nd_{1+x}Ba_{2-x}Cu_3O_{7+\delta}$.

PART 2. SUPERCONDUCTIVITY IN $Nd_{1+x}Ba_{2-x}Cu_3O_{7+\delta}$ SOLID SOLUTION

2.1. Introduction

In DC magnetization measurements of bulk superconductivity, it has proven to be more difficult to obtain sharp superconducting transitions with T_c onsets above 90 K in the RE123 compounds for RE= La, Nd, Sm, Gd than in the Y123 [84,86]. When the identical processing conditions producing high T_c onset (> 90 K) and sharp superconducting transition in Y123 are applied to the RE123 compounds for RE = light rare earths, lowered T_c onsets and broadened transitions are usually obtained. This fact motivated the investigation on the superconductivity in $Nd_{1+x}Ba_{2-x}Cu_3O_{7+\delta}$ solid solution as a representative of light rare earth 123 solid solution systems.

Though their solubility limits are different, light rare earth elements can commonly occupy the Ba sites in addition to their own sites, leading to the $RE_{1+x}Ba_{2-x}Cu_3O_y$-type solid solutions unlike Y and heavy rare earth elements [1]. As discussed in the previous section (see Fig. 1.8), the phase stabilities of the samples having various compositions in Nd123 solid solution are almost identical in pure oxygen, but those having compositions of smaller x (i.e., more Nd on Ba sites) are more stable in reduced partial oxygen atmospheres. This implies that Nd substitution for Ba site is favored at higher oxygen partial pressure. As previously mentioned, even in the nominal Nd123 sample, small amounts ($x < 0.04$) of Nd, therefore, seems to substitute Ba sites in pure oxygen atmosphere. Especially, the cation site disordering between Nd and Ba in Nd123 solid solution is most likely affected by the thermal history, such as sintering temperature and

heating/cooling rate, and ambient atmosphere. This cation site disordering is considered to affect the oxygen site disordering and hence believed to have a significant effect on T_c. The amount and distribution of extra Nd on Ba sites in $Nd_{1+x}Ba_{2-x}Cu_3O_{7+\delta}$ solid solution must be closely related to the maximum obtainable oxygen content and oxygen disordering respectively, which is in turn considered to affect the superconducting transition behaviors of the Nd123 solid solution samples. Furthermore, the T_c onset above 90 K was achieved in the nominal La123 superconductor by [84] only if it was reacted at 900°C in N_2 atmosphere and oxygen-annealed at 400°C. This may be explained by the suggestion that the stoichiometric La123 phase is stabilized only at low oxygen partial pressure as in Nd123. This also suggests that the above trend in Nd123 can be generalized to all light rare earth 123 superconductors. Consequently, it is critical to systematically understand the effect of processing on the superconductivity in the Nd123 solid solution.

Numerous authors [4-8] have reported on a solid solution $Nd_{1+x}Ba_{2-x}Cu_3O_{7+\delta}$ existing between the $NdBa_2Cu_3O_{7-y}$ and the $Nd_3Ba_3Cu_6O_{7+y}$ compounds based on XRD data. However, there is considerable disagreement in the literature as to the superconducting properties as a function of Nd content based on resistivity and AC susceptibility measurements. Common to most of the literature studies is a decrease in the Meissner fraction as the Nd content is increased [8,87,88]. This suggests that the materials are not single superconducting phase.

In the present study, DC magnetization measurements of sintered compacts have shown that the transition width and superconducting fraction are strongly dependent on the temperature at which the material is sintered. For small batches (5g), in which sample homogeneity can be assured, sharp transitions are easily obtained over the range of compositions ($0 \leq x \leq 0.3$). In larger batches (50g), small inhomogeneity in the precursor powder before calcining results in significant impurity phases. For samples with

$x > 0$, this results in broad transitions.

A study on the effects of processing on the superconductivity is based on phenomenological observations. Further understanding is possible only if the structure of a sample after thermal processing is accurately analyzed. The most accurate analysis method to probe the site occupation must be neutron diffraction. For this purpose, samples were sent to ETH, Zürich in Switzerland to be analyzed by neutron diffraction.

In this work, we will demonstrate that while the solid solution does exist over the range $x = 0.04$ to 0.6 at high temperature, there are probably three phases at low temperature. Two of these phases are orthorhombic and superconducting with T_c's of 90 K and approximately 50 K while the third is tetragonal and normal. DC magnetization measurements also show a constant Meissner fraction for the two orthorhombic phases unlike previous reports. Broad superconducting transitions and low Meissner fraction are found to result from incomplete oxygenation of the samples. The cause of this problem appears to be a grain boundary phase which interferes with oxygen diffusion. The results which bear on the origin of the broad transitions in the homogeneous samples and magnetization data showing the temperature and field dependence of a sample with $x=0.04$ will be presented. The results of the neutron diffraction study on these samples will be presented only to reveal the origin of different T_c behavior.

2.2. Experimental Procedures

The materials for the present study were prepared by solid state reactions of Nd_2O_3, $BaCO_3$, and CuO. The precursor powders were dried, weighed, and ground together in a micromill to submicron size. The materials were pressed into pellets, calcined twice in flowing air (flow rate $\approx$ 10 *l*/min) for 24 hours at 890°C with an

intermediate grinding and pressing. Compositions $Nd_{1+x}Ba_{2-x}Cu_3O_{7+\delta}$ were prepared either directly from the starting constituents or by micromilling calcined powders with x= 0.0 and x= 0.5. The samples were then sintered at 1000 or 1050°C in flowing oxygen (flow rate $\approx$ 50 cc/min) for twenty four hours. The samples received a variety of oxygen treatments to convert to the orthorhombic phase, which will be discussed in detail later.

Microstructures of samples were observed by optical and SEM. Powder XRD and DTA were used for identifying phases of these samples. EDS on polished cross sections showed that independent of preparation routes, the Nd and Ba were uniformly distributed in the primary phases. Scanning Auger Microscopy (SAM) was used to investigate compositional varitions near grain boundary regions of samples by A.J. Bevolo. Oxygen contents of the samples were measured by Inert Gas Fusion method at the analytical center in Ames Lab.

DC Magnetization measurements were performed in a Quantum Design MPMS SQUID magnetometer both in field cooled (FC) and zero field cooled (ZFC) mode with the applied fields of both 10 and 50 Oe. Elastic and inelastic neutron scattering for Nd123ss has been performed by Allenspach at ETH in Switzerland.

2.3. Results and Discussion

Processing-Superconductivity Relationships

Samples with sharp transitions and consistent Meissner fractions (Fig. 2.1) were prepared using the following final schedule. In O_2 atmosphere, the furnace was rapidly ramped to 900°C and held for 30 minutes to be followed by slow ramping at 1°C/min to 1050°C, where it was held for 24 hours. The temperature was then lowered at 0.1

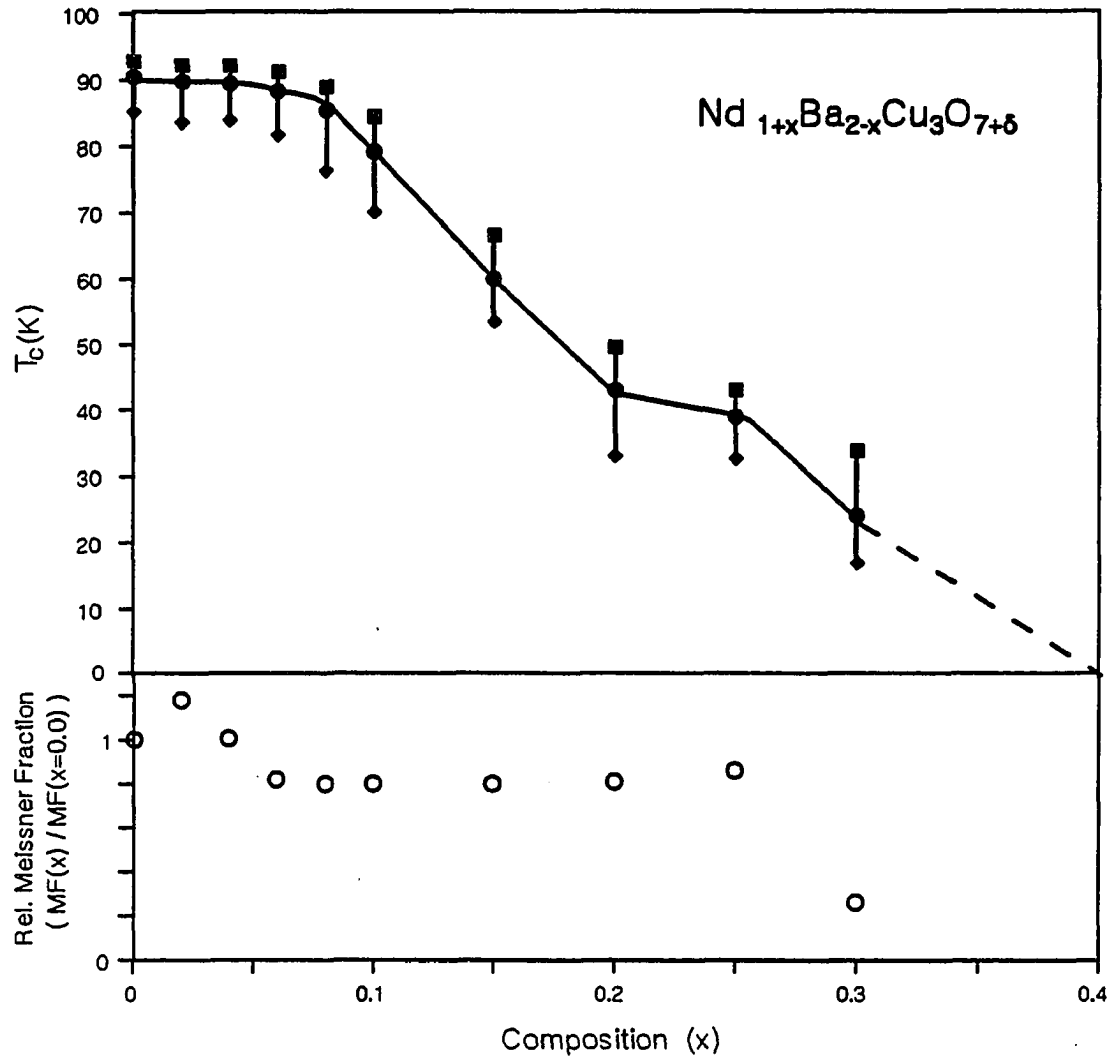

Figure 2.1. Superconducting transition temperature and relative Meissner fraction versus composition. For the applied field of 50 Oe, T_c corresponding to the transitions of 10%, 50%, and 90% FC values at 10 K on the FC curves are indicated as filled squares, circles, and diamonds, respectively. Meissner fractions (MF(x)) are normalized to the x=0.0 value (MF(x=0.0)).

°C/min to 900°C, held for 1 hour, and again at 1 °C/min to 600°C with a pause of 6 hours. Following a ramp at 1 °C/min to 400°C, the samples were held for 24 hours and furnace cooled. All samples except low Nd substitution ($x < 0.04$) appeared single phases as determined by XRD and DTA. For the samples of $x < 0.04$, small peaks of $BaCuO_2$ phase were observed on the XRD patterns and a small hump with the onset temperature of ~ 1025°C in pure O_2 atmosphere, which is believed to be only due to this second phase [60], was noticed on DTA curve (see Fig. 1.8).

The initial set of samples with nominal compositions of x=0.0, 0.1, 0.2, 0.25, 0.3, 0.4, and 0.5 were sintered at 1000°C for 24 hours, air quenched and then annealed in O_2 at 900°C for one hour and cooled at 1 °C/min to 450°C and held for 24 hrs followed by a furnace cool to room temperature. DC magnetization measurements of these samples showed broad transitions, though the onsets were such that resistivity or AC susceptibility measurements would have exhibited sharp transitions at relatively high temperatures. In addition, the Meissner fractions showed a systematic decrease as a function of increasing x. Further oxygen treatments of these samples at low temperature resulted in nonsystematic changes in both T_c and Meissner fraction.

As x is increased the transition temperatures and widths indicate a number of regimes (Fig. 2.1). As mentioned previously, for $0 < x < 0.04$, these samples are not single phases but small amounts of $BaCuO_2$ are involved. Close metallographic examination using both optical and SEM confirmed this conclusion. In fact, for the initial set of samples, the systematic decrease in the transition width and varying Meissner fraction were noticed for $0 < x < 0.02$ [86]. The source of the impurity was traced to the fact that the starting Nd_2O_3 powder was dried at 750°C which while sufficient to dry Y_2O_3 is too low in the Nd_2O_3 case. Subsequent drying of the Nd_2O_3 for 24 hours at 950°C followed by 10 hours at 1000°C resulted in a 1.25% weight loss. Thus, for x <

0.0125, the samples are Nd-deficient showing that the range of solid solution does not extend beyond the 123 compound. For $0.04 \leq x < 0.3$, the superconducting transitions are sharp and exhibit a constant Meissner fraction of ~ 30% in the applied field of 50 Oe (Fig. 2.2). There is evidence for two plateaus in the data (Fig. 2.1), the first at 90 K for $x < 0.1$ and the second at approximately 50 K for $0.1 < x < 0.3$. As shown in Fig. 2.2, the $x=0.3$ sample shows a sharp transition at 35 K but only 1/3 the Meissner fraction of the other superconducting samples. For compositions $x=0.4$ and $x=0.5$ the magnetization data follows a Curie law at low temperatures with the 0.4 sample showing evidence of 2% of a superconducting impurity phase at 20 K (Fig. 2.2).

Two plateaus in T_c vs x suggest comparing these Nd123ss materials with T_c behaviors of oxygen deficient Y123 samples. As Nd increases in Nd123ss, total oxygen content should increase because Nd^{+3} substitutes for Ba^{+2} sites. In order to investigate the similarity between Nd123 and Y123, the oxygen contents of the Nd123ss samples studied were measured by Inert Gas Fusion method. To obtain better statistics, three measurements per each sample have been performed. The error per each measurement is 1.5 wt% O_2 in the sample. The error in the average oxygen contents from three measurements is ± 0.06. While the error bars of measurements are too large to determine detailed behaviors, gross trends may be evident.

The oxygen contents vs x are plotted in Fig. 2.3. As expected, general trend shows that oxygen content increases as extra Nd on Ba sites increases. In order to take into account the added oxygen associated with Nd on the Ba sites, the formal (i.e., average) valence of Cu (V_{Cu}) was calculated. Assuming Nd, Ba, and O have fixed valence states of +3, +2, and +2, respectively, the values of V_{Cu} could be calculated from the following equation:

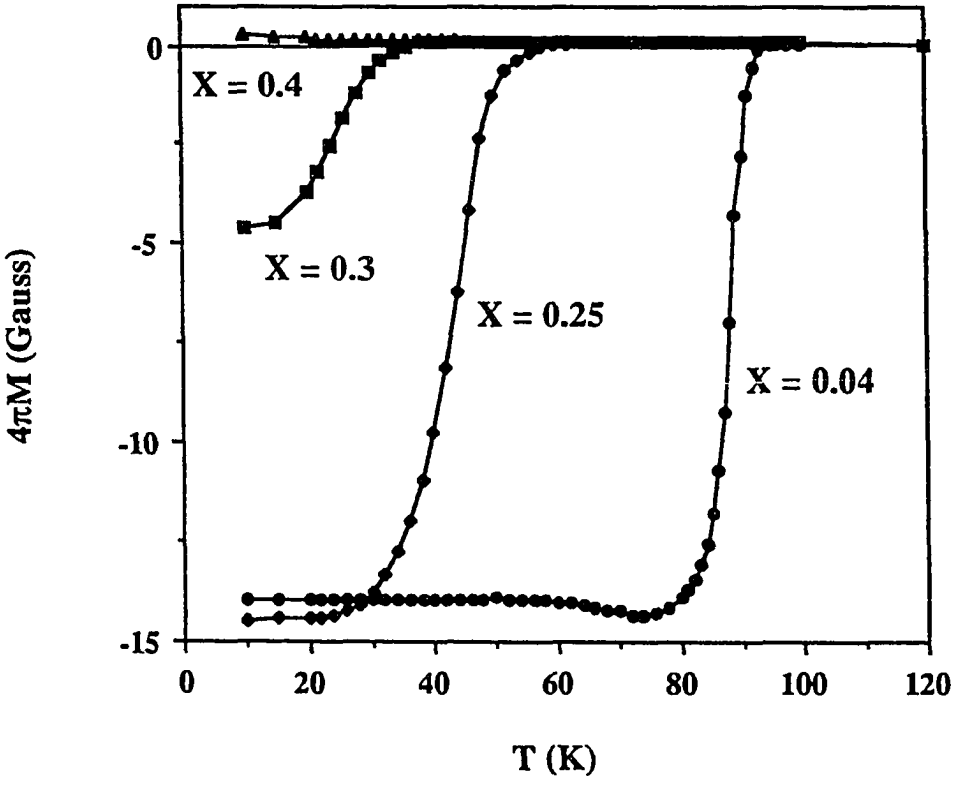

Figure 2.2. Field Cooled (FC) DC magnetization curves for the $Nd_{1+x}Ba_{2-x}Cu_3O_{7+\delta}$ solid solutions with the applied field of 50 Oe.

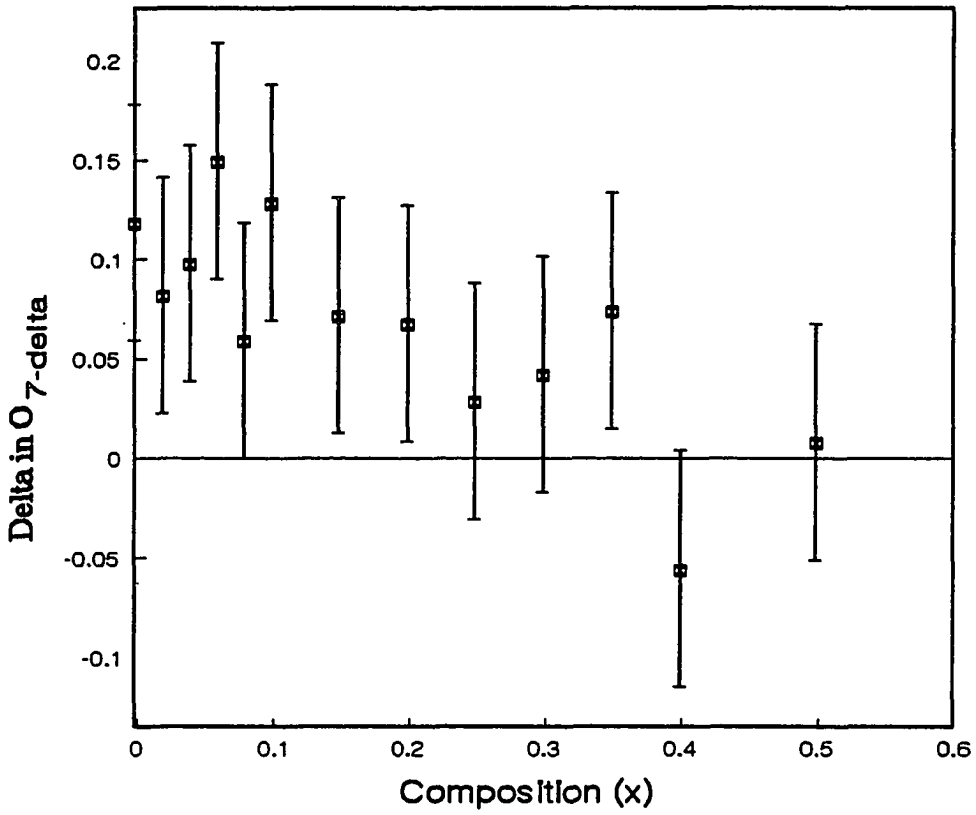

Figure 2.3. Measured total oxygen contents versus compositions are plotted. For the oxygen content, delta(δ) in $Nd_{1+x}Ba_{2-x}Cu_3O_{7-\delta}$ is used.

V_{Cu} = [2×(avg. oxygen content) - 3(1+x) - 2(2-x)] ÷ 3

where avg. oxygen content is the average oxygen content and x is the amount of extra Nd on Ba sites noted in $Nd_{1+x}Ba_{2-x}Cu_3O_{7+\delta}$. Fig. 2.4 shows the relationship between formal valence of Cu and x. There is a clear trend that formal Cu valences decrease as x increases for fully oxygenated samples. This trend has been characterized by a linear least square fit as shown in Fig. 2.4.

By plotting T_c vs formal valence of Cu for Nd123ss and Y123, a direct comparison between the systems can be made. In Fig. 2.5, we have plotted these data. For Nd123ss, formal valences of Cu were calculated from the linear fit data in Fig. 2.4. For Y123, the values of Cu were calculated from the oxygen contents in the literature reported by Cava et al. [89], using the above equation (here, x = 0). For purposes of comparison, the scales for the formal Cu valence have been adjusted to emphasize the similarity. Common to both systems, it is observed that T_c is insensitive to the initial drop in V_{Cu} and then abruptly decreases as V_{Cu} further decreases until it is again less sensitive to V_{Cu}. This suggests that two plateaus in T_c vs x for Nd123ss basically have the same origin with those in T_c vs oxygen content for Y123. Therefore, the analogy of this system to the ortho I and ortho II phases in the $YBa_2Cu_3O_{7-y}$ system is clear. Careful examination of the powder XRD diffraction patterns show that for $x < 0.1$ the material is orthorhombic and for $x > 0.3$ it is tetragonal. For $0.1 < x < 0.3$, there is some evidence for splitting of the tetragonal XRD peaks suggesting that the analogy to the $YBa_2Cu_3O_{7-y}$ system is correct with the ortho I, ortho II, and tetragonal phases. As is expected in this situation, the width of the superconducting transitions reflect the slope of the T_c versus x curve. An obvious difference is that T_c of Nd123ss is more sensitive to V_{Cu} than T_c of Y123 so that for a small change of V_{Cu}, T_c of Nd123ss changes more abruptly. In addition, the second

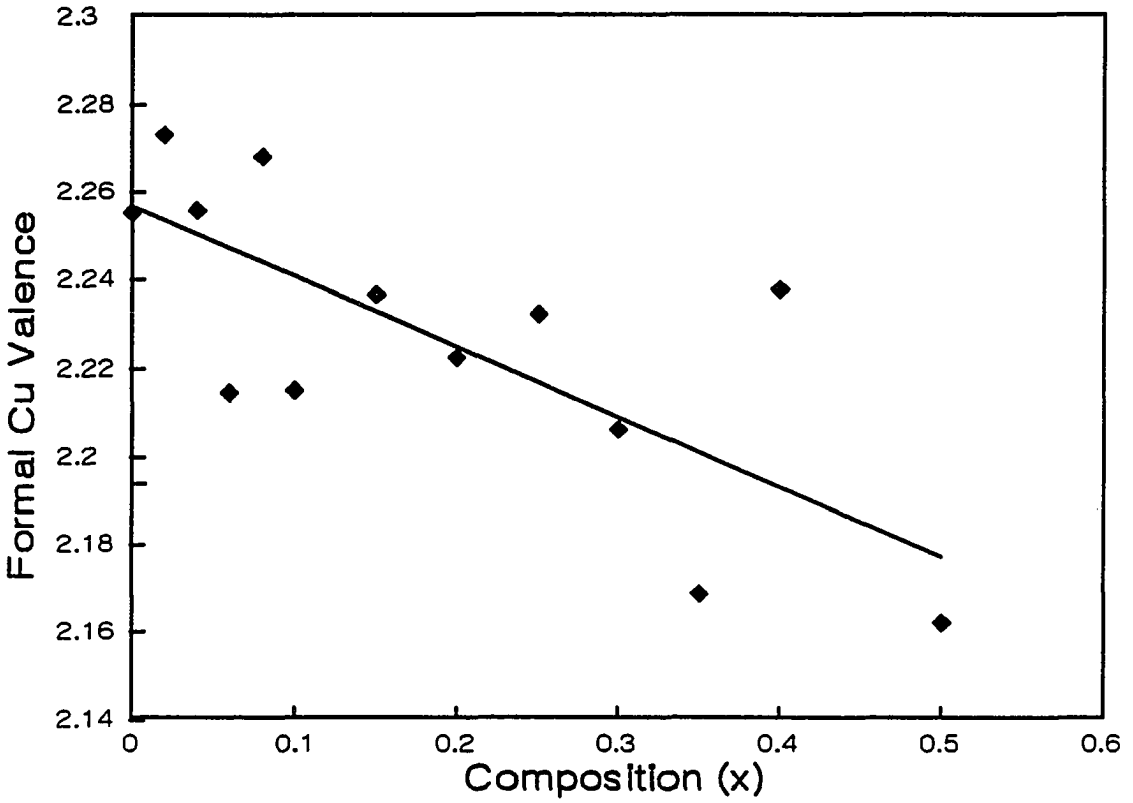

Figure 2.4. Formal valences of Cu calculated from average oxygen contents are plotted as a function of composition. From the linear regression method, the solid line was obtained to show a gross trend.

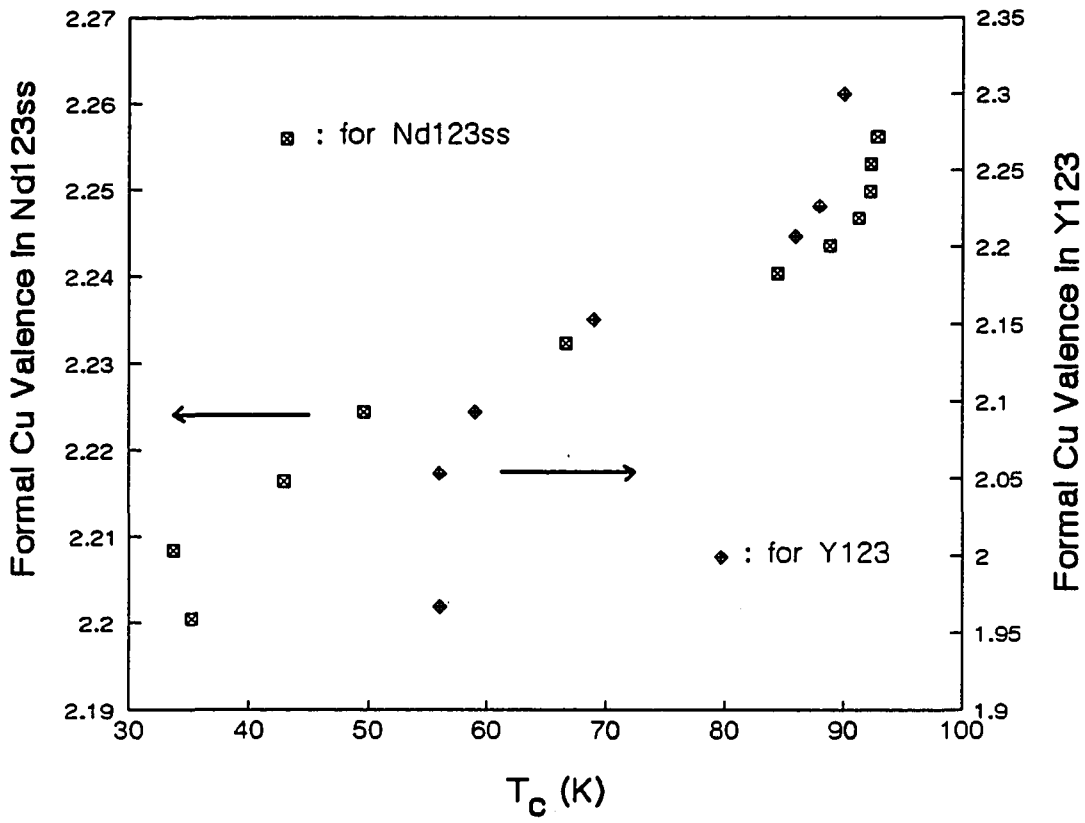

Figure 2.5 For a direct comparison between Nd123ss and oxygen deficient Y123 systems, T_c versus formal Cu valences (V_{Cu}) are plotted for both systems. For Nd123ss, the V_{Cu} values were taken from the solid line in Fig. 2.4 and for Y123, those were calculated from the published data by Cava et al. [89].

plateau in T_c in Nd123ss extends to a lower value than in Y123. While T_c in Y123 is a function of V_{Cu}, it is well characterized by Cava et al. [89] that two plateaus at 90 K and 60 K as a function of oxygen stoichiometry are associated with plateaus in the effective valence of the plane coppers, Cu(2) but not with that of the chain coppers, Cu(1) (see Fig. 2). In our simple approach, only average valence of Cu is considered and hence, there is no way to separate the valence changes of Cu sites in the Nd case. However, as we know that excess Nd affects the occupation of the O(5) sites, there is no reason to expect that the change of the effective Cu(2) valence as a function of V_{Cu} is the same in $Nd_{1+x}Ba_{2-x}Cu_3O_{7+\delta}$ as it is in $YBa_2Cu_3O_{7-y}$. Since the O(5) site is related to the chain sites Cu(1), it is reasonable to expect that as the O(5) sites are occupied the change in the Cu(1) valence in Nd123ss is less than in Y123. This would imply that the Cu(2) valence is a much stronger function of V_{Cu} in Nd123ss than in Y123.

The differences between the present data (Fig 2.1) and the literature data [8,87,88] are two-fold. One is that the sample preparation methods in the literature commonly employ the sintering temperatures of $\leq$ 1000°C which lead to broad transition widths and a systematic decrease in Meissner fractions as a function of increasing x in the present study. The other one is that common to most of the literature studies is a decrease in the Meissner fraction from AC susceptibility measurements as the Nd content is increased, suggesting that the materials are not single superconducting phase in contrary to the present results. In addition, close investigation of superconductivity in the narrow composition range ($0 < x < 0.1$) has not been reported.

For comparison, samples of nominal composition $Nd_1Ca_xBa_{2-x}Cu_3O_7$ were prepared. Since Ca^{2+} has the same ionic radius as Nd^{3+}, Ca substitution for Ba sites should introduce the same degree of size effect without the change in O content associated with the valence change. While the Ca substitution does affect T_c, the depression is not

nearly as pronounced as in the Nd case (Fig. 2.6). Powder neutron diffraction analysis for a sample with nominal composition of $NdCa_{1.25}Ba_{1.75}Cu_3O_y$ by Allenspach [54], however, shows that this compound actually has $(Nd_{0.93}Ca_{0.07})(Nd_{0.07}Ca_{0.18}Ba_{1.76})Cu_3O_7$ which is more complicated than expected because simple substitution of only Ca for Ba sites does not occur. Therefore, a simple comparison is impossible.

While the above data is well behaved, it was observed that the transition widths, Meissner and screening fractions for all values of x are much more dependent on processing parameters than in the Y123 case. In an attempt to understand the origin of the broad transition widths and inconsistent Meissner fractions obtained under normal Y123 processing conditions a wide range of processing conditions were investigated for the composition $Nd_{1.25}Ba_{1.75}Cu_3O_{7+\delta}$. It was determined that samples furnace-cooled from 1000°C to 900°C prior to oxygenation exhibited the same broad transitions as samples quenched from 1000°C and then heated to 900°C (Fig. 2.7(C)). Extended anneals (up to 96 hrs) at 450°C did not appreciably affect the shape of the transition, however slow cooling at 0.15 °C/min from 900°C to 450°C followed by 24 hours at 450°C produced sharp transitions. When annealed at 450°C for 16 hours in N_2 the weight loss for the slow cooled sample with the sharp transition was twice that of the normally processed material. When the sintering temperature was raised to 1050°C, a marked change in the behavior was noted as shown in Fig. 2.7(A). Independent of the heat treatments intermediate between sintering and the final 450°C anneal, the samples exhibited consistent transition temperatures with uniformly sharp transitions, and high Meissner fractions. There was one exception to this behavior which occurred when a 1050°C sample, which had received the full oxygenation schedule, was subsequentially heated to 1000°C for 24 hours and then oxygen-annealed at 450°C. This sample exhibited a broad transition (Fig. 2.7(B)). This

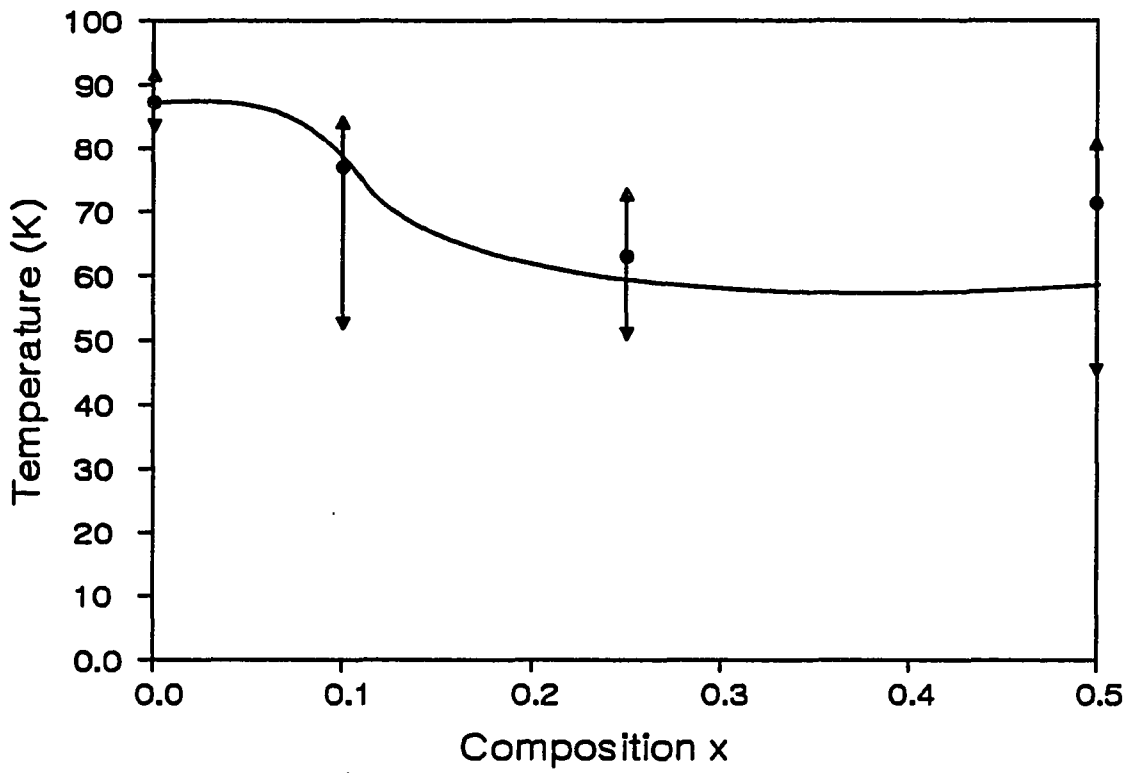

Figure 2.6. Superconducting transition temperature versus composition for $NdCa_xBa_{2-x}Cu_3O_{7-y}$. With the applied field of 50 Oe, 10, 50, and 90 % of the transition in the FC curves as measured by DC magnetization are indicated.

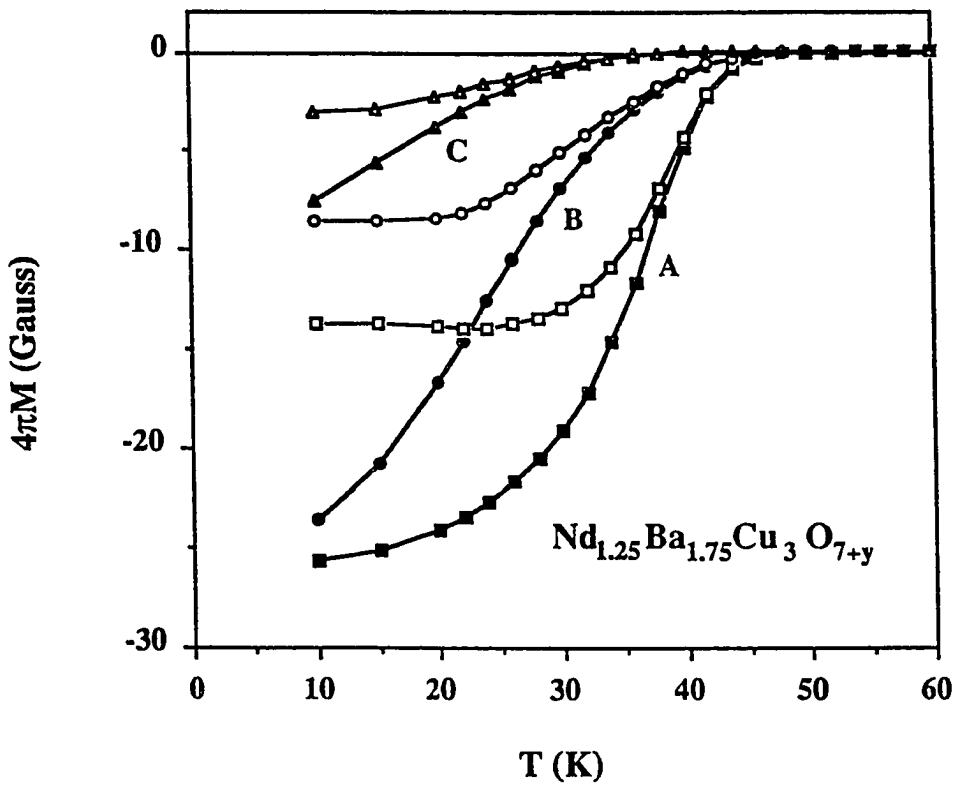

Figure 2.7. DC magnetization curves for $Nd_{1.25}Ba_{1.75}Cu_3O_{7+\delta}$. All samples received the same oxygen treatment at 450°C. (A) Sintered at 1050°C. (B) Sample A was annealed at 1000°C. (C) Sintered at 1000°C. Open symbols are Field Cooled (FC) measurements and closed symbols are Zero Field Cooled (ZFC).

is in contrast to the sharp transition obtained when after sintering at 1050°C and cooling to 1000°C holding for 24 hours and then treating normally as shown in Figure 2.7(A). Differential Thermal Analysis (DTA) of the two samples, one sintered at 1000°C with a broad transition and the other at 1050°C with a sharp transition revealed the presence of a minor melting event at 974°C in both samples. The event is tentatively identified as the peritectic reaction between $Nd_{1.25}Ba_{1.75}Cu_3O_{7+\delta}$ and CuO indicates the presence of less than 1 wt% CuO impurity phase.

Interestingly, when a sample with a sharp transition was subsequentially heated to 1000°C for 24 hours and oxygenated, the sample exhibited a broad transition. This is in contrast to the sharp transition obtained when after sintering at 1050°C and cooling to 1000°C holding for 24 hours and then oxygenated normally. It should be noted that the peritectic decomposition temperature of $Nd_{1+x}Ba_{2-x}Cu_3O_{7+\delta}$ is 1110°C in pure O_2 atmosphere so that no decomposition of the compound should take place during the sintering at 1050°C. Since a single sample was changed from a sharp transition to a broad transition, the transition width is not associated with sample inhomogeneity temperature itself.

With a minor melting event taking place near the region of interest, the possibility of the distribution of the impurity phase affecting the oxygenation of the sample exists. In order to investigate this hypothesis, a broad and a sharp transition sample were fractured *in situ* in a Scanning Auger Microscope. In both samples a thin Nd deficient grain boundary layer was found. The thickness of the layer was the same within experimental resolution. In both samples the oxygen content was uniform within individual grains. Due to sample orientation effects comparison of oxygen content between grains was not accurate enough to determine overall oxygen homogeneity. No evidence was found to support the hypothesis.

A second hypothesis investigated is that Ba on the Nd sites is responsible for the broad transition. The lower site disorder at higher temperature could result from what is effectively more reducing atmosphere at high temperature. For this study, neutron diffraction and inelastic scattering have been employed. The results will be discussed below.

Structure-Superconductivity Relationship

According to Allenspach [54], in some Nd123 samples with orthorhombic symmetry, somewhat high O(5)-occupation was detectable, which was dependent upon the processing condition, and some effects on crystalline electric field (CEF) are generated as well as the variation of the transition temperature. From the results of neutron spectroscopy-study on x= 0, 0.25, 0.5, it will be discussed how the processing condition affects O(5)-occupancy in the nominal Nd123.

In the samples of the nominal Nd123, $BaCuO_2$ always appeared as a minor phase on their XRD patterns, which was reproducible for 5 different batches. This result is also independent of reaction temperatures so that it is commonly observed after calcination at 890°C in flowing air or after subsequent repeated reaction at 1050°C for 24 hrs in O_2 atmosphere. There are two possibilities for this result. The first one is a deviation of the starting materials from nominal 123 composition especially due to insufficient drying of Nd_2O_3 at 700°C for 24 hrs since the weight loss of Nd_2O_3 precursor is about 1.25 % after subsequent drying at 1000°C for 10 hours. Since fully dried Nd_2O_3 powder produced the same result, this possibility is less likely. The second possibility is the formation of Nd123 solid solution rather than the nominal 123 under given calcination condition. In this case, it is natural to obtain two phases of 123ss and 011 from the nominal composition

of 123. Since the phase stabilities of Nd123ss are comparable to Nd123 in pure oxygen atmosphere, a small amount of Nd can readily substitute for Ba sites even in the nominal Nd123 composition, and thus O(5) sites can be occupied because this extra Nd on Ba sites can induce O(5)-occupation to satisfy the charge neutrality. The present experimental result shows that 011 phase in the nominal Nd123 disappears and Nd123ss (x=0.25) decomposes into 123, 211, and 001 phases when they are reacted in the lower p_{O2} atmosphere ($p_{O2} < 10^{-2}$ atm). This means that Nd123ss is stable only above a certain oxygen partial pressure at least $p_{O2} > 0.2$ atm. Therefore, the second possibility is highly probable. In order to identify the conditions for stable phases, a systematic study on the stable phase boundaries must be made as in the Y123 [68].

Several further questions are still unanswered: (1) What is the lowest solubility limit under a given atmosphere (P_{O2}) ?. (2) How does the extra Nd on Ba site actually arrange in the crystal structure ? (3) What is the cause of high O(5)-occupation determined by neutron diffraction [54] in some Nd123 samples of oxygen concentration as high as 6.94 ? For the first question, it is extremely difficult to determine the value because the solubility limit is believed to be a function of P_{O2} and temperature and moreover, the value seems to be small. According to experimental results of XRD, DTA, and SEM, the value must be approximately 0.02 - 0.04 for the sample sintered at 1050°C in oxygen and followed by slow cooling to 450°C (0.1 °C/min) and held for 24 hrs for oxygen annealing since for samples with x> 0.04 no impurity phases were detectable. This result is different from that reported by Zhang et al. [70] who suggested x=0.1. However, they have not prepared samples with the compositions of $0.0 < x < 0.1$. In addition, most authors investigating Nd123 superconductors have not even tried to closely look at the lower solubility limit. For the second question, it is not clear yet whether the small number of extra Nd ions on Ba sites are randomly distributed (i.e., ordered) or

locally disordered. For Y123, the oxygen ordering is known to be dependent upon the oxygen concentration [89] such that at low oxygen concentration (about 6.5) oxygen site ordering is different from that at high oxygen concentration close to 7. Therefore, two types of orthorhombic phases (OI and OII) are formed and they are closely related to superconducting transition temperature. However, the situation is more complex in the Nd123 since we should also consider the ordering of extra Nd ions on Ba sites, as well as that of oxygen ions. Furthermore, extra Nd sites are closely related to oxygen occupation because of its higher valence state (+3) compared to Ba ions (+2). Since most oxygens required for tetragonal to orthorhombic transition are incorporated during cooling and oxygen annealing and the cation mobility is much lower than that of oxygen at such temperature region, extra Nd sites probably determine the oxygen sites in the sample of high oxygen concentration. The experimental results in chapter 1 strongly suggest that even in Nd123 solid solution there is a small amounts of Nd on the Ba sites (x=0.04). Therefore, we can not exclude the possibility of severe local disordering in cation sites such that the local distribution of extra Nd satisfies from nominal 123 to larger extent of solid solution (even to the upper solid solution limit, $x \approx 0.6$).

The next question is how much this inhomogeneous distribution in Ba sites occupied by Nd ions is localized with a random microscopic scale in the grain. This must be closely related to the processing condition. Since the superconducting transition of the sample sintered once at 1050°C for 24 hrs and followed by an oxygen annealing described above is still broad, the extra Nd ions are probably still strongly disordered and hence higher O(5)-occupation is possible. The grain is likely to be analogous to the fine mixture of solid solution samples with relatively high solubility band. After repeated regrinding and sintering at the same condition, the transition becomes sharp and T_c onset increases a little. This is probably due to ordering of extra Nd ions. On the other hand, when the

samples are sintered below 1000°C in O_2, such a sharp transition could have never been obtained. This is the case of most thermal reactions reported in the literature. Therefore, there must be an optimum temperature in a given atmosphere to randomize extra Nd on Ba sites. Since the sample usually has small amount of 011 phase and the p3 reaction (123+011 → L) or 011 melting occur at about 1025°C in O_2 [3], sintering temperature must be above this temperature. For the third question, it can be understood as follows; Though there exists a severe local disordering in extra Nd sites, the oxygen content can be as high as in a ordered case. This disordered extra Nd sites will induce higher O(5)-occupation if O(5)-occupancy is not linearly but parabolically (or exponentially) proportional to the amount of extra Nd concentration on Ba site and thus transition curve will be broad. This will be more severe when the sample is sintered at lower temperature or the cation site is highly disordered such as the quenching experiment like melt-spin processing (T_c measurements show this for my sample). According to the result of CEF for $NdBa_2Cu_3O_{6.94}$ by Allenspach [54], the peak at 12 meV totally shifts and broadens, and the spectrum very strongly resembles that of the sample with x=6.62 in that T_c = 25 K and O(4)-occupancy =0.59. The only difference is the O(5)-occupancy.

For the sample x=0.04, field cooled magnetization versus temperature measurements show a sharp transition in Fig. 2.8. The small anomaly below T_c is associated with a non-equilibrium flux distribution trapped in the sample during cooling. The zero field cooled data shows field starting to penetrate the sample at 40 K indicating weak link behavior. High field hysteresis measurements were carried out at 10, 30, 50, and 70 K as shown in Fig. 2.9. Two factors are immediately apparent in the magnetization loops. First is the paramagnetic contribution of the Nd moments which increases at low temperature. Second is the marked fish tail effect at all temperatures above 10 K. Extensive work on this effect in single crystals of $YBa_2Cu_3O_7$ by Seuntjens

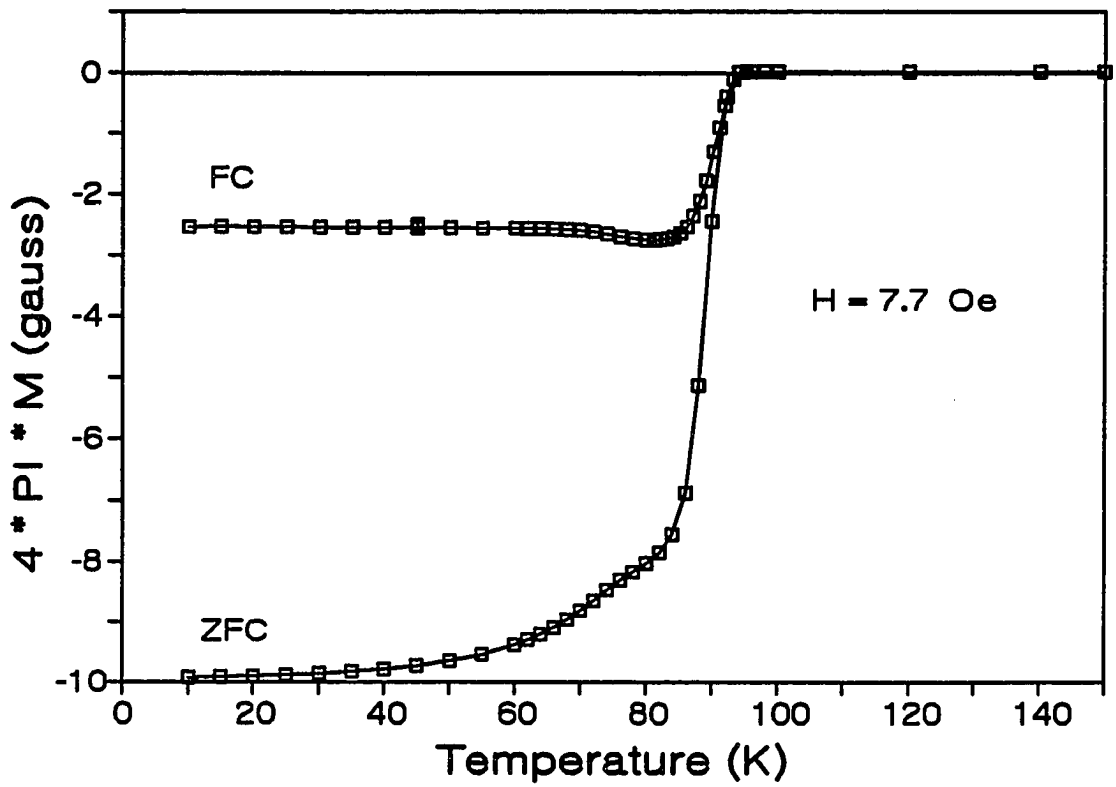

Figure 2.8. Magnetization versus temperature for $Nd_{1.04}Ba_{1.96}Cu_5O_{7+\delta}$.

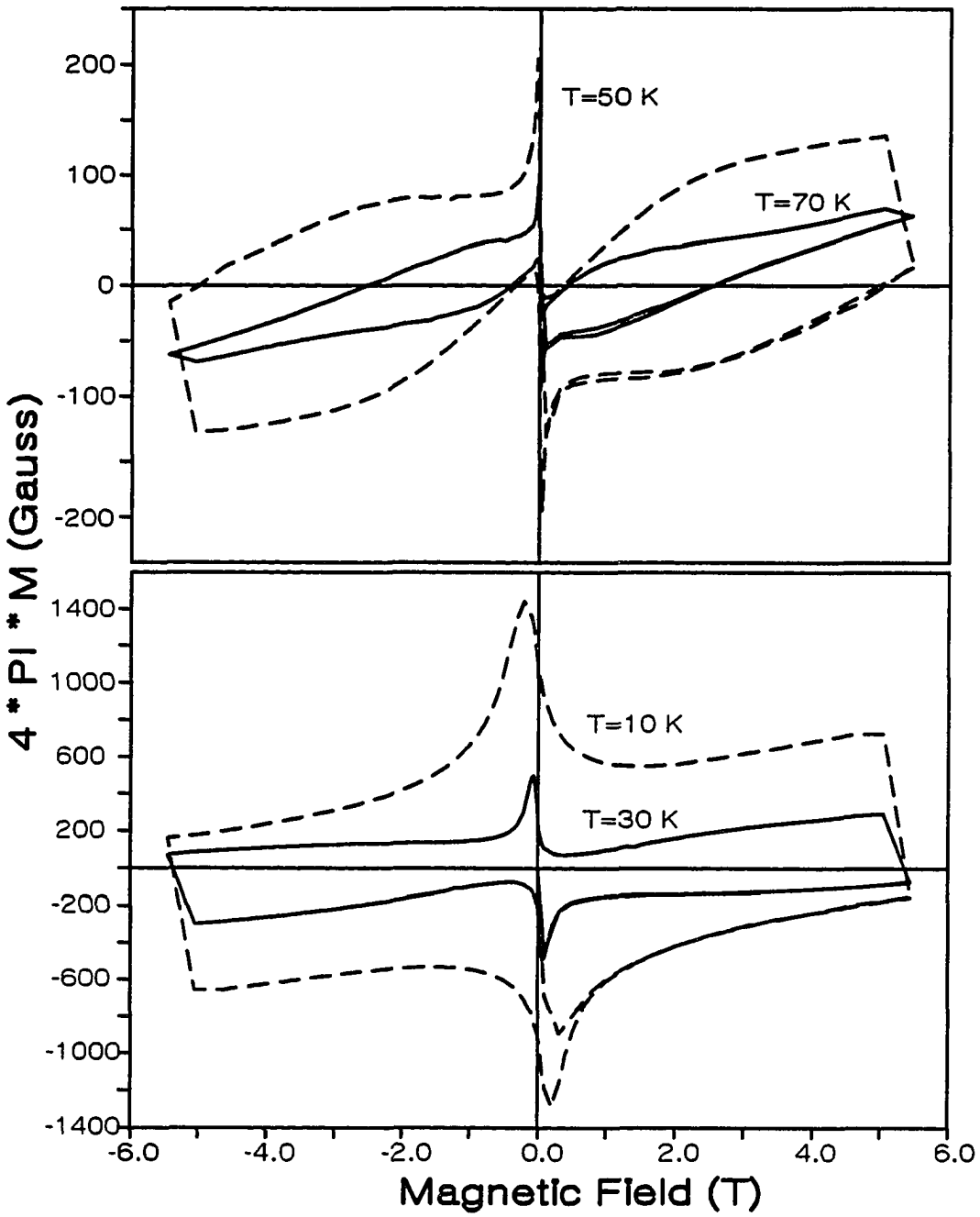

Figure 2.9. Magnetization versus Field for $Nd_{1.04}Ba_{1.96}Cu_3O_{7+\delta}$.

and co-workers [90] had shown that it is due to incomplete oxygenation of the sample. Upon extended oxygen annealing the effect is eliminated and the width of the loop and hence J_c is considerably enhanced. If the optimum anneal is exceeded, J_c is reduced from the optimum value. If the analogy to the Y material holds for Nd, further oxygen annealing is necessary before we can separate the effect on pinning of Nd on the Ba sites from oxygen defects due to insufficient heat treatment.

In Fig. 2.10, the width of the hysteresis loop versus field is plotted for all four measured temperatures. Of particular interest is the relative field independence of the high field region. Applying the Bean model [91] using the average sample grain size of 20 microns gives critical currents of 10^6, $4x10^5$, $2x10^5$, and $4x10^4$ amps/cm^2 for 10, 30, 50, and 70 K in an applied field of 3T. These values are very encouraging considering the incomplete oxygenation of the sample. The situation on the grain boundaries is considerably less positive. Due to the high temperatures required to obtain sharp transitions, grain growth is a problem even in very clean samples. The microcracking which is expected to occur with grains of this size combined with the observed Nd deficient layer on the grain boundaries results in very low critical currents and considerable effort will be required to overcome these problems.

2.4. Conclusion

The $Nd_{1+x}Ba_{2-x}Cu_3O_{7+\delta}$ system has been shown to be extremely sensitive to impurity phases which interfere with complete oxygenation of the samples. For uniformly oxygenated samples there appears to be a complete analogy between this system and the $YBa_2Cu_3O_{7-\delta}$ system.

$Nd_{1+x}Ba_{2-x}Cu_3O_{7+\delta}$ samples have been prepared with sharp superconducting

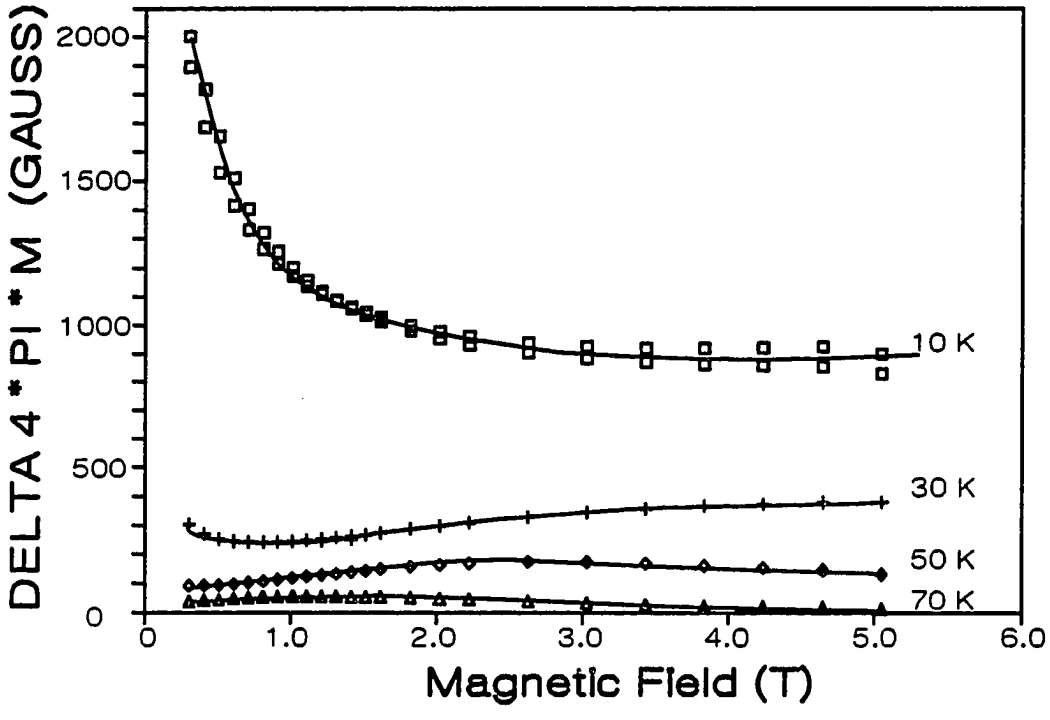

Figure 2.10. Widths of the magnetic hysteresis loops for $Nd_{1.04}Ba_{1.96}Cu_3O_{7+\delta}$.

transitions by careful attention to the details of sample preparation. Two causes for broad samples have been observed. The first is sample inhomogeneity which is more difficult to eliminate than in the $YBa_2Cu_3O_7$ case and the second appears to be associated with site disorder within a homogeneous sample. Very reasonable intragranular critical currents have been obtained in a sample with a small amount of Nd substituted on the Ba sites but it is not clear if the Nd plays a direct role in flux pinning at this time. Intergranular critical currents are still quite low due to the large grain size in the high temperature processed material and the Nd deficient layer on the grain boundaries.

PART 3. THEORETICAL BACKGROUND FOR THE FLUX CREEP MODEL

In this section, a thermally activated flux creep theory will be reviewed. This theory was originally proposed by Anderson [55] and later, more analytically derived and successfully applied to the various conventional superconductors by Beasley et al. [56]. The details in analytical expressions for this theory are available in numerous publications [92], and hence this theory will be described with minimum mathematical tools and discussed from the materials aspect. Recently developed theories attempting to explain flux motions in the new ceramic superconductors will be briefly summarized since there exists no consensus among them yet. Before describing the above theory, general classification of superconductors will be reviewed for basic understanding and the critical state model will be introduced since this model is often used to analyze the magnetic hysteresis and the flux creep in the non-ideal Type II superconductors.

3.1. Classification of Superconductors

According to their magnetization curve behaviors, all superconductors can be grouped into two types, Type I and Type II as shown in Fig. 3.1. When a bulk superconductor exhibits perfect diamagnetism (complete Meissner effect) up to the field H = H_c (thermodynamic critical field) and becomes normal above H_c as shown in Fig. 3.1(a), it is named Type I superconductor. Many pure metal superconductors exhibit this behavior. In fact, the complete exclusion of an applied magnetic field from the interior of a Type I superconductor does not occur. According to London equations [93], an applied

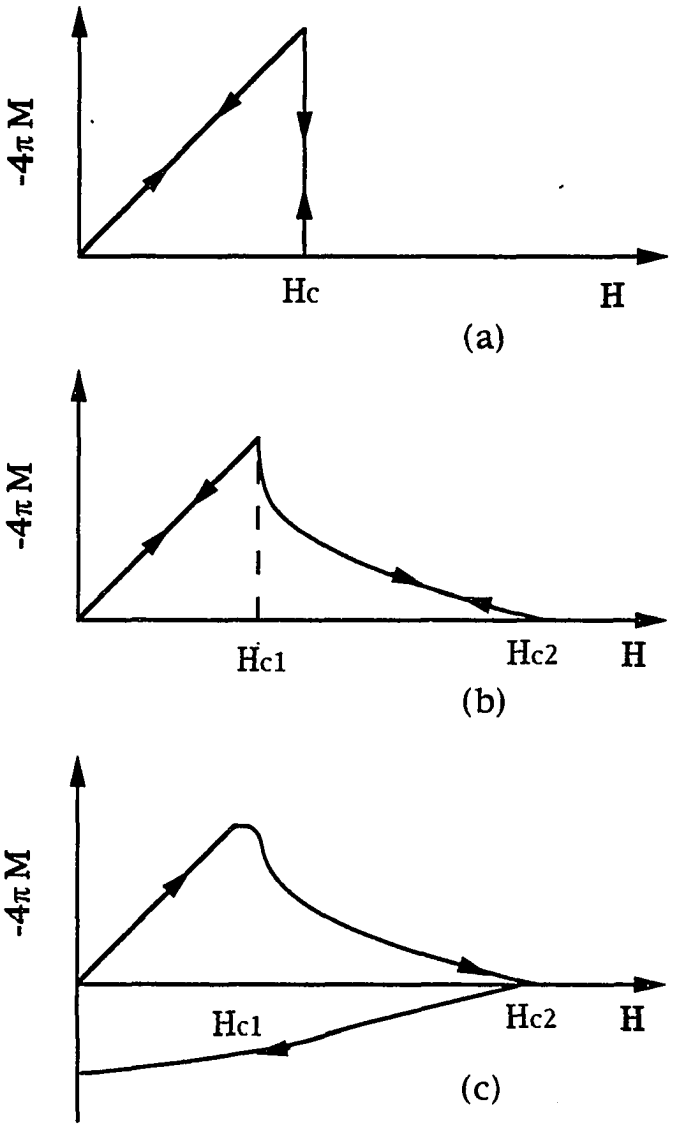

Fig. 3.1. Magnetization of superconductors: (a) Type I, (b) ideal Type II, and (c) non-ideal Type II (irreversible magnetization)

magnetic field exponentially penetrates from surface into a superconductor, so that the penetration can be characterized by the depth λ_L (London penetration depth) at which the field has fallen to $1/e$ of its value at the surface. For typical value $\lambda_L(0)$ at zero temperature for pure superconductors is about 500 Å. Type II superconductors have two distinct superconducting regions as shown in Fig. 1(b) and (c). Below H_{c1} (the lower critical field), they behave exactly the same way as Type I. Above H_{c1} and below H_{c2} (the upper critical field), a mixed state of superconducting and normal regions becomes stabilized. As an applied magnetic field increases, perfect diamagnetism is continuously destroyed and disappears above H_{c2}. In addition to numerous alloy or transition metal superconductors, all new oxide superconductors exhibit Type II behavior.

The existence of Type II superconductors was first theoretically predicted in terms of Ginzburg-Landau (G-L) theory [94] by Abricosov in 1957 [95]. Abricosov found that there was a characteristic value of $\kappa = 1/\sqrt{2}$ which separates two distinct superconducting phases. The G-L parameter κ is given by λ/ξ, where λ is the penetration depth and ξ is the coherence length. For $\kappa < 1/\sqrt{2}$, the surface energy between superconducting and normal regions is positive and so the total free energy is raised. Hence the perfect Meissner state is the lowest energy state. The materials with $\kappa < 1/\sqrt{2}$ are conventional Type I superconductors. For $\kappa > 1/\sqrt{2}$, the surface energy is negative. This negative surface energy stabilizes a mixed state, usually called a vortex state. The materials with $\kappa > 1/\sqrt{2}$ are Type II superconductors.

The vortex state in Type II superconductors is the thermodynamic state in which quantized magnetic flux penetrates the superconductor in an array of flux tubes (variously called fluxoids, fluxons, or vortices) each carrying a quantum of flux ϕ_o, where $\phi_o = h/2e = 2.067851\ (\pm\ 5 \times 10^{-6}) \times 10^{-15}$ Weber. From the center of each quantized flux tube, local magnetic field penetrates over a distance $\lambda(T)$. The strength of superconductivity is

given by an order parameter which increases from zero at the center to unity at the surface of the vortex.

In Type II superconductors, ideal reversible magnetization behavior as shown in Fig. 3.1(b) is more difficult to achieve for fields above H_{c1} because the sample with vortices is thermodynamically in the most stable state, giving only a partial Meissner effect with $0 < -4\pi M < H$. Even a small degree of inhomogeneity is then sufficient to pin some vortices at local free energy minima so that some vortices remain trapped inside a sample when the external field is removed. Most Type II superconductors show an irreversible magnetization behavior as shown in Fig. 3.1(c) due to such an interaction with defects.

If a Type II superconductor has the flux line that is free to move, the Lorentz force resulting from currents in superconductor will cause the flux line to move by transferring energy from the current to the flux line lattice. This results in a voltage drop i.e., a non-zero resistance. Therefore, for a Type II superconductor, the flux lines must be pinned in order to observe zero resistance in the presence of a current. For a sufficiently large current, the Lorentz force on the flux lines will be sufficient to depin the flux line lattice and destroy zero resistance. If the pinning force for the flux line lattice is not much greater than kT, the combination of a thermal activation and Lorentz force will result in flux line motion at currents less than the critical current density J_c.

As a result, the magnetic hysteresis can be understood in terms of the pinning of the vortices by the defects. Moreover, because this pinning of vortices is necessary for the material to be able to carry a volume transport current (as opposed to a surface current in the penetration depth), practical conductors are designed to be as irreversible as possible. As shown in Fig. 3.1(c), the superconductors with the departures from the reversible curve are called the non-ideal Type II superconductors, or hard superconductors.

3.2. The Critical State Model

The critical state model was first proposed by Bean [91] in 1962 to interpret the irreversible (i.e., hysteretic) magnetization in the conventional superconductors. In the critical state, the Lorentz force on the vortices is assumed to be balanced by the pinning force. Here the Lorentz force is originated from the interaction between the vortex and the supercurrent which is associated with the local induction field gradient inside the sample. When the magnetic field is applied to a hard superconductor, the field starts to penetrate the material above H_{c1} in the form of vortices. The vortices nucleated in the penetration layer are driven into an inhomogeneous mixed-state superconductor until they are trapped by pinning sites such as defects. Some vortices overcoming the pinning force move further into the material until they are subsequently pinned. Consequently, a downward gradient of flux density from the surface is established. The basic premise of Bean model is that there exists a limiting macroscopic superconducting current density $J_c(H)$ that a hard superconductor can carry; and further, that any electromotive force, however small, will induce this maximum current to flow locally. In other words, a critical state is established when the circulating current density associated with the gradient of local field in the material is equal to the critical current density J_c. As a result of these screening currents, the induction field (B) inside the superconductor is less than the applied field (H) for increasing fields while $B > H$ for decreasing fields.

For a uniform slab of the thickness D with H parallel to the plane of the slab, the following relation between the hysteresis width (ΔM) and J_c was derived by Bean [46] for H larger than the full penetration field strength (H^*) at which the magnetic flux first completely penetrates the sample to the center as shown in Fig. 2.2(b):

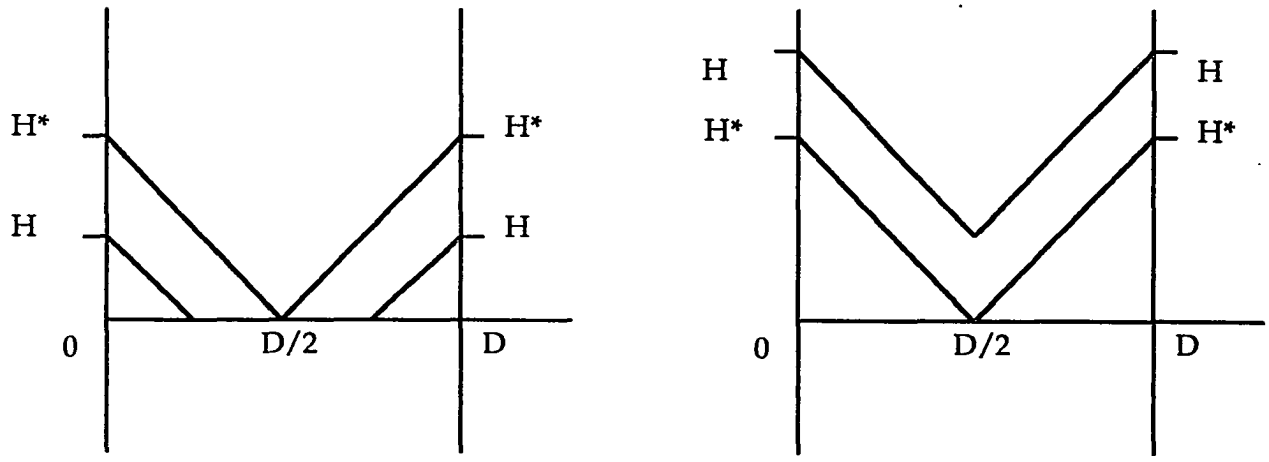

Fig. 3.2. Local field distribution in a slab at a constant applied field based on Bean model : (a) partial penetration for $H < H^*$ and (b) full penetration for $H > H^*$

$$\Delta M = (D/2c)J_c \qquad (1)$$

where c is the light velocity. Therefore, J_c can be indirectly determined by measuring the hysteresis width. This is so called "magnetic J_c". For different sample geometry, one can obtain different expressions as follows [96,97]:

$$\Delta M = (2a/3c)J_c, \quad \text{for a cylinder} \qquad (2a)$$

$$\Delta M = (a/c)(1-a/3b)J_c, \quad \text{for a rectangle} \qquad (2b)$$

where, a is the radius in Eq. (2a) and 2a×2b is the cross section in Eq. (2b).

For many high T_c samples, relevant dimensions must be taken from grain size because the applied magnetic field larger than H^* penetrates the grain boundaries. Moreover, if materials have high conduction anisotropy as in high T_c superconductors, the crystallographic orientation relative to the applied field direction must be also considered.

In the Bean model, J_c is assumed to be independent of field. More detailed models incorporate a field dependence of J_c. Kim et al. [98] modified the Bean model and suggested that the critical current density J_c was dependent on the local induction field and so proposed the relationship, $J_c \propto 1/H$ for high fields. Likewise, many treatments of the critical state model for interpreting the magnetization in different systems have been proposed. Recently, M. Xu [99] has reported generalized equations for the critical state model by unifying all possible functions of $J_c = J_c(T,H)$.

For the low values of the critical current density, one obtains that the difference between the magnetic induction at the surface and at the center of the specimen is much

smaller than the applied field in ceramic high T_c superconductors. Therefore, B is essentially constant and hence the Bean approximation of a uniform J_c throughout the sample is probably valid.

3.3. A Thermally Activated Flux Creep Theory

In the conventional Type II superconductors, it has been observed that the magnetization slowly decays at a given applied field and temperature as time proceeds. This magnetic relaxation was attributed to the metastable distribution of vortices in the superconductor caused by the pinning sites. Since the decay rate in the conventional superconductor is extremely slow, Bean critical state model could be successfully employed to magnetically estimate the critical current density.

Before going further into analytical expressions, a brief discussion on the origin of the flux creep will be appropriate. Consider a single flux line in a material with a uniform sinusoidal pinning potential $U(x) = U_0 \sin x$ (i.e., wash board potential) as shown in Fig. 3.3(a). With no current flowing, a flux line at position a is pinned if $U_0 >> kT$. A current flowing perpendicular to x exerts a force on the flux line in the x direction, which results in the "tilted wash board potential" as shown in Fig. 3.3(b). When the current reaches a critical value J_c, the relationship in the potential is given by $U(a) = U(b)$ and then the flux line moves. For $J < J_c$, $U(b) - U(a) > 0$, but there is a probability $P \propto exp\ [-\{U(b)-U(a)\}/kT]$ so that the flux line can move from a to c due to thermal activation. This process is called a thermally activated flux creep.

In real superconductors, flux lines are not isolated but interact with each other so that the flux line lattice (FLL) is formed. Hence an effective pinning potential U_0 of FLL must be considered. Since material has fixed defects (defect lattice, DL) but FLL changes

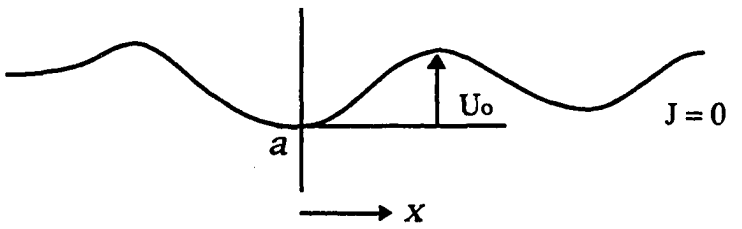

(a)

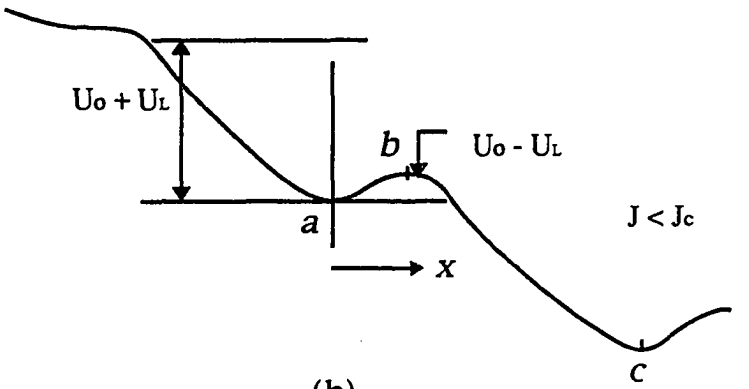

(b)

Fig. 3.3. A simple schematic diagram explaining the origin of the flux creep. Curve in (a) is a uniform sinusoidal pinning potential (i.e., wash board potential) and in (b) is "tilted wash board potential" due to Lorentz force.

as self-field induced from screening current changes, the relationship between FLL and DL determines U_o so that $U_o = U_o$ (J, H) at a given temperature.

Analytical theory for this relaxation behavior was first proposed by Anderson [55] and proved to be good agreement with the experimental results by Kim et al [98]. In this theory, a thermally activated flux creep is presumed to occur and the logarithmic time decay of magnetization is derived. Detailed theoretical analysis was given by Beasley at al. [56], in 1969.

In the above flux creep theory, the depth of an intrinsic pinning potential well, U_o, which is the activation energy in the absence of a flux gradient, is modified by a potential arising from a Lorentz force on the vortices proportional to the transport current density J, which equals to the critical current density J_c in the critical state. Suppose this perturbation energy is U_L, the intrinsic pinning potential U is reduced to an effective pinning potential $(U_o - U_L)$ (see Fig. 3.3). Since the thermally activated vortices are presumed to move into the sample by hopping along the pinning centers, the simple Arrenhius equation for the hopping rate is given by

$$\nu = \nu_o \{\exp[-(U_o - U_L)/kT] - \exp[-(U_o + U_L)/kT]\} \qquad (3a)$$

or

$$\nu = 2\nu_o \exp(-U_o/kT)\sinh(U_L/kT) \qquad (3b)$$

where ν_o is an attempt frequency of an order 10^8 - 10^{12} sec^{-1}, and the first and second terms in Eq. (3a) are forward and reverse flux hoping respectively. This equation also implies that the "true" critical current can be defined only if no flux hopping occurs in the

critical state because, if vortices still move, current density cannot keep its maximum value. As assumed in Anderson-Kim flux creep model, suppose there exists a linear relationship between the effective pinning potential and current density; $U = U_o(1-J/J_{co})$ (i.e., $U_L = U_o(J/J_{co})$), where J_{co} is the critical current density without the thermal activation. Under the condition $U_L >> kT$, which means the reverse hopping rate is negligible compared with the forward hopping rate, the flux hopping rate is given by

$$\nu = \nu_o \exp[- U_o(1-J/J_{co})/kT] \qquad (4)$$

For a given measurement frequency ν, we can get the following relationship:

$$J = J_{co} [1 - kT/U_o \ln(\nu_o t)] \qquad (5)$$

Finally, the logarithmic time decay of J(t) is obtained. In the critical state, the critical current density J_c can be used instead of J. Then the above equation can be rewritten as

$$J_c = J_{co} [1-kT/U_o\ln(t/\tau_o)] \qquad (6)$$

where τ_o is the relaxation time at the critical state.

By combining Eq. (6) with the critical state model, one can relate J_c to the magnetization (at least at low temperatures) for the expression of the magnetic relaxation. If Bean critical state model is used, one can directly derive a logarithmic magnetic relaxation for a slab of thickness D, valid in the limit $H > H_{c1}$ and $H > H^* = 2\pi DJ_c/c$:

$$dM/d\ln(t) = (DJ_{co}/4c)(kT/U_o) \qquad (7)$$

If we combine this equation with the relationship between J_c and the hysteresis loop width derived from Bean model (Eq.(1)) and let $J_c \approx J_{co}$ to the first-order approximation in kT/U_o:

$$dM/dln(t) = (\Delta M/2)(kT/U_o) \qquad (8)$$

Consequently, this relation can be used for the calculation of the pinning energy from the magnetic relaxation and hysteresis loop width measurements at a given applied field and temperature. Later, Eq.(8) will be also used for the flux creep study on Nd123 solid solution.

More analytically than Anderson's derivation for the logarithmic flux creep rate, Beasley et al. [100] used a non-linear diffusion equation for the flux conservation and solved it in a thin hollow cylinder to obtain the total flux in the specimen as a function of time. The solution lead to the logarithmic time decay of the total flux, which is the same result with Anderson-Kim flux creep theory. By assuming $U >> kT$, the resultant flux creep rate R is given by

$$R = \pm(1/3)\pi kT\rho^3[(\partial\Phi/\partial|\nabla B|)_{t1,\rho}]^{-1}(1\pm\delta) \qquad (9)$$

where ρ is the radius of the cylindrical sample and δ is the correction factor, which is small compared to unity. The $\pm$ signs correspond to increasing and decreasing applied fields. They also pointed out that U could be a non-linear function of ∇B (or J) when thermal activation becomes comparable to an pinning energy barrier (i.e., violating the assumption, $U/kT >> 1$, which is required for the linear approximation as in Anderson -

Kim model). As shown in Figure 3.4, in the critical state, Eq. (9) can be graphically solved. In this case, the flux creep rate is given by

$$R = (d\phi/dt) = (\pi/3)kT\rho^3 \ (4\pi/c) \ (J_c/\Phi_o)(1\pm\delta) \qquad (10a)$$

or in the average form, $R_{av} = (R^+ + R^-)/2$

$$R_{av} = (d\phi/dt)_{av} = (\pi/3)kT\rho^3 \ (4\pi/c) \ (J_c/U_o) \qquad (10b)$$

Since $4\pi M = \phi/\pi\rho^2$ and c is the speed of light, and by using the relation $\rho J_c = 15\ \Delta M$ for a cylindrical sample from Bean model, we can have the same analytical expression with Eq. (7).

3.4. Flux Creep Theories in High T_c Superconductors

In contrast to the conventional superconductors, one of the characteristic features of high T_c superconductors is their large magnetic relaxation. For high T_c superconductors, large thermally activated flux creep is expected since the pinning potential U_o is small and thermal energy kT is large. The large relaxation was first reported by Müller et al.[100] in the magnetization of $(La,Ba)_2CuO_4$ ceramics, and it has been argued that this behavior reflects a superconducting glassy state resulting from random weakly linked superconducting grains. Thereafter, extensive flux creep studies [101-104] of high T_c superconductors, mostly $YBa_2Cu_3O_7$, have been performed. In particular, Yeshurun and Malozemoff [101] reported that the magnetic relaxation in Y123 crystals was comparable to ceramics, suggesting either that the crystals themselves were granular or that some other

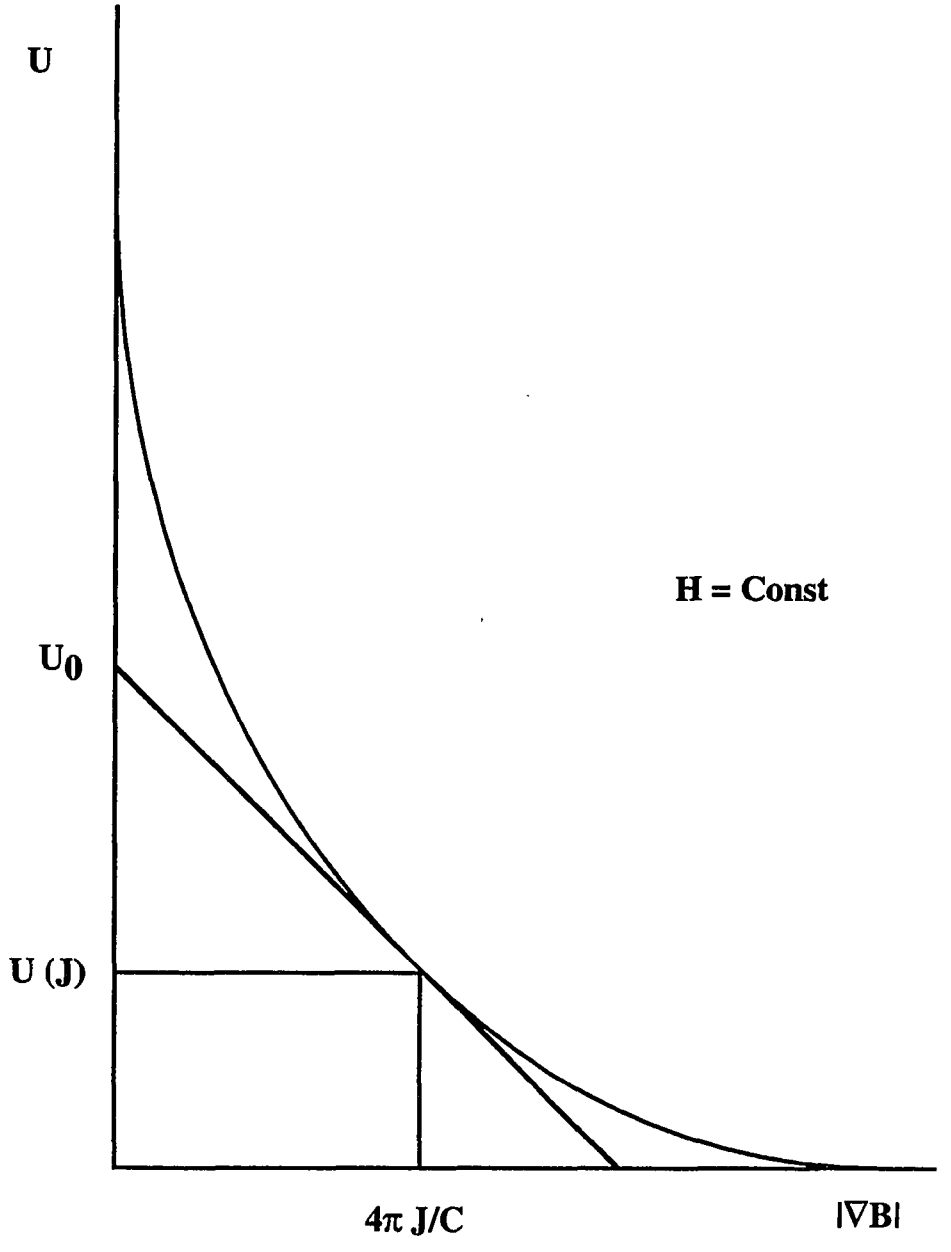

Fig. 3.4. Graphical interpretation of the relationship among U, U_o, and J from Beasley et al. [56]

mechanisms, like a giant flux creep, were occurring, and pointed out that the time-dependent magnetization result could be interpreted by a classical thermally activated flux creep. They also found that the relaxation was anisotropic, in that it was faster for the applied field parallel to the c-axis, and that the field-cooled magnetization showed much less relaxation, indicating the field cooled (FC) magnetization might deviate from the flux profile of the critical state model.

Common to most of magnetic relaxation studies of high T_c superconductors, rough logarithmic relaxation with respect to time has been observed on either the zero-field cooled (ZFC) or remnant magnetization. This logarithmic relaxation behavior, well-known in conventional superconductors, has been explained by the classical Anderson-Kim theory of flux creep. The large flux creep rate is considered to be inherited from low pinning barriers due to small coherence lengths of the high T_c superconductors. Hence it is a serious problem for application since the higher operating temperature naturally increase thermal activation.

In the analytical solution of the Anderson-Kim flux creep theory by Beasley et al.[56], the time dependence of the total flux $\phi(t)$ in the specimen is given by $\phi(t) = \phi(t_o) - A \ln(t/t_o)$, where A is constant. Hagen and Griessen [105] pointed out that this relaxation has two non-physical divergences. The divergence at t=0 can simply be removed by an appropriate choice of the origin on time. The other at $t \rightarrow \infty$ was not a problem for classical superconductors because of their extremely slow relaxations. However, for high T_c superconductors, which exhibit large relaxation effects, it is evident that for times larger than $t = t_o \exp(\phi(t_o)/A)$ the Beasley expression is not valid as $\phi(t)$ must always remain positive. Furthermore, the assumption $U/kT >> 1$ is not applicable to high T_c materials. Assuming a linear approximation in U vs J, Hagen and Griessen derived a relation,

$$M(t) = M_o[1-(kT/U_o)\ln(1+t/t_o)]$$

which is based on a Monte Carlo simulation without the restriction of $U/kT >> 1$. This relation is well obeyed up to $t = t^*$ given by $t^* = t_o \{\exp(U_o/kT)-1\}$. For $t >> t^*$, $M(t) \sim \exp(-\alpha t)$. Here t_o is the relaxation time and $10^{-6} < to < 10^{-12}$ sec.

The above derivation is based on an assumption of a single barrier height model. Hagen and Griessen [105] extended this model to include a distribution of activation energies which resulted in a distribution function composed of the fraction of barriers and activation energies.

Unlike the logarithmic time decay of magnetization, numerous non-logarithmic behaviors at high magnetic fields have been also reported [106-110] since the magnetization deviates further from logarithmic time dependence as measuring temperature increases close to T_c. It is believed that the linear relationship holds at low temperature (but not too low like $T < 5K$ in 90 K 123 superconductors) in Y123 superconductors and thus the classical thermally activated flux creep theory may be applied to these materials. In order to interpret the non-logarithmic time decay of magnetization, several theories have been suggested for high temperature or high field regimes. Kes et al. [106] pointed out that large magnetic relaxation at high temperature might be caused by the large flux flow rather than a discrete motion of flux creep, and proposed a thermally activated flux flow (TAFF), in which for $J_{co} >> J$, $\sinh(JU_o/J_{co}kT)$ term in Eq.(3b) could be approximated by $(JU_o/J_{co}kT)$. The TAFF model interprets the observed non-logarithmic decay as a crossover from Anderson-Kim logarithmic decay to exponential decay, where the crossover time t_{cr} is of $(1/\nu_o)\exp(-U/kT)$. In a collective flux creep model, Feigel'man et al. [107] derived a decay $J(T,t) = J_{co}[U_o/kT\ln(t/t_o)]^{1/\alpha}$, $t_o \sim 1/\nu_o$ by assuming $J << J_{co}$

and $U(J) = U_o(J_c/J)^{\alpha}$ (power law). Then, $R = d\ln(M)/d\ln(t) = kT/[U_o + \alpha kT\ln(t/t_o)]$. This model is valid at high temperature because distance between vortices becomes smaller than the penetration depth. Fisher [108] proposed a vortex glass phase for a collective vortex creep. This model predicts α to be a universal exponent less than 1, in contrast to the claim of the Feigel'man et al. which predicts values changing from 1/7 to 3/2 to 7/9 with increasing temperature. Finally, from resistivity measurements near T_c, a logarithmic law for the J-dependent pinning barrier $U = U_o\ln(J_{co}/J)$ has been assumed by Zeldov et al.[109]. This leads to $J = J_{co}(t/t_o)\exp(-kT/U_o)$ and $R = kT/U_o$. Each of these models results in a non-logarithmic decay of magnetization.

With the assumption of $U/kT >> 1$ but no assumption of a linear approximation in U vs J, Xu et al.[103] derived the flux creep rate $R = (1/M)dM/d\ln t = -kT/U_o^*$ from Eq.(8) in a flux creep model by Beasley et al. [56], where $U_o^* = -|\nabla B|(\partial U/\partial|\nabla B|)$ is an apparent pinning potential whose relationship to the true pinning potential U_p depends upon the nature of the U versus deriving force relationship. More recently, Maley et al.[110] reported the flux creep in grain-aligned samples of YBCO powder. With no assumption of a linear relationship in U vs J, and for $U >> kT$, they appealed to Arrenhius relation for flux jumping. Then the relation $U(J) = kT[\ln(dM/dt) + c]$ is derived, with c a temperature and field-dependent constant. This approach is physically unclear yet but it enables to compare the flux pinning energies between different systems.

All approaches to interpret the magnetic relaxation in high temperature superconductors are simply based on the various functional forms of J-dependent U. Thus those may be simplified by a graphical interpretation as Beasley et al. suggested. For a linear approximation as in Anderson-Kim model, U as a function of J (or $|\nabla B|$) must be a straight line. However, as pointed out by Beasley et al. [56], it must be generally a curve in the U - J plane and moreover, it must be also concave regardless of their special

functional forms, such as power law and exponential law. The temperature dependence of the effective pinning potential U_o at a given H can be understood on this plot since U_o is the intercept on U axis extrapolated from the tangent line at a given J_c and hence U_o increases as temperature increases from T_1 to T_2 as shown in Fig. 3.5(a).

Until this point, we have not explicitly discussed the origin of the pinning force. Recently, Hylton and Beasley [53] have proposed the flux pinning mechanisms in thin films of $YBa_2Cu_3O_x$ with very large critical current densities. Based on the analysis of typical pinning energies and critical current densities, it is argued that the pinning is due to a large density of point defects.

They suggested the conclusion that core interactions were most likely responsible for the pinning in these thin films. To examine core pinning they assumed that the core of the vortex sits in a defect that is "normal" in the sense that the order parameter is completely depressed in the vicinity of the defect. The energy gain per unit length ϵ_c of a vortex in such a defect is just the condensation energy in the core region;

$$\epsilon_c = (H_c^2/8\pi)\, \pi\xi_{ab}^2 = \Phi_0^2/64\pi^2\lambda_{ab}^2$$

where ξ_{ab} and λ_{ab} are coherence length and penetration depth in the a-b plane. H_c is a critical magnetic field and Φ_0 is a flux quantum.

Consequently, it is obtained that minimum energy U_o for depinning a vortex line from defects on it, which is called characteristic pinning energy of the system by authors, is given by

$$U_o = 2l_p/l\epsilon_c d \qquad (11)$$

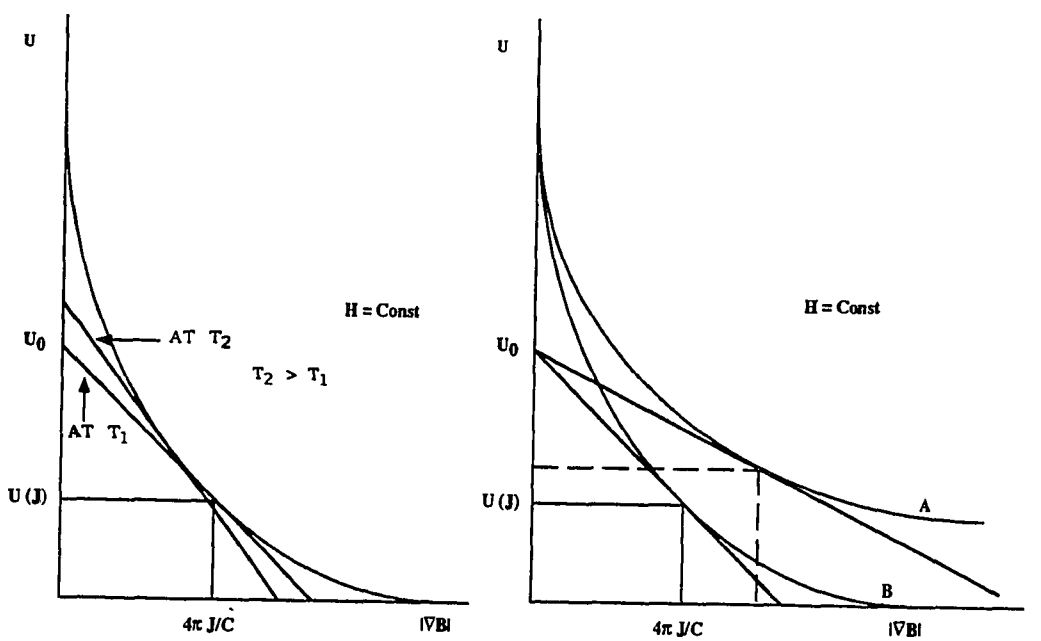

(a) (b)

Fig. 3.5. Graphical interpretation for (a) a linear increase in U_o as a function of temperature and (b) a differentiation of pinning barriers between different systems

where l is the length of a vortex and l_p is a pinned vortex segment length. The condensation energy ϵ_c in the core region is given by determined by $\epsilon_c = (H_c^2/8\pi)\pi\xi_{ab}^2 = \Phi_o^2/64\pi^2\lambda_{ab}^2$, where ξ_{ab} and λ_{ab} are the coherence length and penetration depth in the a-b plane. d is a distorted length from the pinning points.

The above equation implies that pinning energy is proportional to the density of point defects (more accurately, the distance between point defects). To calculate the minimum density of defects for the effective flux pinning, they also proposed a simple model of pinning by point defects in the CuO_2 planes that predicts a spacing between defects of 53 Å. However, in order to obtain larger J_c, a maximum defect concentration will be required without degrading T_c too much.

PART 4. FLUX CREEP IN $Nd_{1+x}Ba_{2-x}Cu_3O_{7+\delta}$ (x= 0.0 - 0.1)

4.1. Introduction

The highest transport critical current density (J_c) achieved for the bulk-type high T_c ceramic superconductors is at least two orders of magnitude lower than that for the best thin films. This low J_c is generally known to originate from weak links at grain boundaries because high T_c ceramic superconductors have extremely short coherence length (ξ) and highly anisotropic conduction. In addition, the intragranular critical currents are low due to flux creep in the bulk materials. Unfortunately, the reported magnetic relaxation in the $YBa_2Cu_3O_{7-\delta}$ single crystals is as fast as in the ceramics, indicating that it is also essential to introduce the flux pinning sites in the grains to achieve the high intragranular J_c.

There has been considerable effort directed at identifying the flux pinning mechanism, but no consensus has been reached. On the other hand, experimentally there has been reasonable success in producing the effective flux pinning centers by various techniques. Examples are the generation of defects by irradiating Y123 single crystals [48-50], the precipitation of fine CuO phase in the matrix of the Y123 grains by decomposing Y124 [51], the production of stacking faults by incorporating excess CuO to Y123 phase [111], and the trapping of fine Y211 particles in the Y123 grains by solidifying Y123 partial melt (i.e., Y211 + liquid phase) below the incongruent melting temperature of Y123 [67]. While a recent report by Civale et al. [50] clearly demonstrates that columnar defects (about 50 Å in diameter and more than 15 μm long) generated by heavy-ion

irradiation can play a role of strong flux pinning centers at high temperatures and fields, this method is not readily applicable to a mass production of the material. Therefore, a systematic study on the potential effective pinning sites is still required so as to identify more effective defect-types (including second phases) and to optimize the size, shape, and distribution of those defects.

Among $REBa_2Cu_3O_{7-\delta}$ superconductors, Nd substitution for Y site has been studied by numerous authors [4-8]. It is particularly interesting in that there exists a solid solution $Nd_{1+x}Ba_{2-x}Cu_3O_{7+\delta}$ (solubility limit : $0.04 \leq x \leq \sim 0.6$ at 890 °C in air or pure oxygen atmosphere) and superconductivity appears up to $x \approx 0.4$ when it is oxygen-annealed. In addition, from a processing standpoint, it must be also interesting alternative to Y123 for application because the primary phase region of Nd123 on the phase diagram is known to be much wider than that of Y123 [66,2]. On the other hand, many of the superconducting transitions reported for $Nd_{1+x}Ba_{2-x}Cu_3O_{7+\delta}$ are excessively wide probably due to the existence of the same solid solution that makes this material interesting. We have produced samples having sharp superconducting transitions for the extensive compositions ($x = 0.0 - 0.5$) [113] in $Nd_{1+x}Ba_{2-x}Cu_3O_{7+\delta}$ and confirmed that there is no substantial decrease in T_c for $x < 0.06$ while a significant depression of T_c occurs for $x > 0.1$.

Since the substitution of Nd^{3+} for Ba^{2+} site is expected to suppress the superconducting order parameter due to an increased oxygen content of the O(5) sites surrounding this substitution, the question arises as to whether the flux pinning strength can be enhanced due to variations in the local oxygen order.

In this work, we present the results of the magnetic relaxation measurements and the estimation of the flux pinning energy (U_o) within the framework of a classical thermally activated flux creep model [55,56,112] for the $Nd_{1+x}Ba_{2-x}Cu_3O_{7+\delta}$ solid solution ($x = 0.0 - 0.1$). And we will apply the results of Hylton and Beasley's analysis

[53] on a flux pinning mechanism to qualitatively understand the present system. In addition, we have carefully examined experimental data to separate measurement artifacts from sample properties and suggested a successful measurement procedure for this purpose.

4.2. Experimental Procedures

Sample Preparation

The precursor materials of Nd_2O_3, $BaCO_3$, and CuO were dried and weighed to prepare two batches having nominal compositions of x = 0.0 and x = 0.1 in $Nd_{1+x}Ba_{2-x}Cu_3O_{7+\delta}$. The materials were ground in a micromill and pressed into pellets to be calcined three times at 890°C in flowing air (flow rate $\approx$ 10 liters/min) for 24 hours with an intermediate micromilling and pelletizing. Other batches having nominal compositions of x= 0.02, 0.04, 0.06, 0.08 were prepared by mixing as-calcined powders of x=0.0 and x=0.1.

All batches were micromilled to submicron size and pressed into pellets at 10 ksi. Pellets were put together into a tube furnace and sintered at least twice at 1050°C for 24 hours in an oxygen gas atmosphere (O_2 gas flow rate $\approx$ 100 *ml/min*) with an intermediate micromilling and pelletizing, cooled slowly at 1 °C/min to 450°C, held for 24 hours, and cooled slowly to room temperature. To obtain sharp superconducting transitions in this solid solution system, sintering conditions such as temperature and atmosphere are crucial as well as subsequent oxygen-annealing [113] because the Ba site ordering must be achieved by completely randomizing the substitutional solutes of Nd. Details on the effect of the cation site order-disorder due to thermal processing on the superconductivity was

discussed in the previous section.

Sintered bulk samples, which have the average grain size of 40 μm for all batches, were crushed into powder and sieved with 500 mesh (25 μm) to obtain single grain particles. While these samples appeared to be fully oxygenated, powder samples were again annealed in oxygen gas using the following procedures in order to avoid the potential effect of oxygen deficiency on the magnetic relaxation. Each sieved sample was put into a sealed quartz tube filled with oxygen gas at a total pressure of 2/3 bar. The quartz tubes were set into a Al-Bronze block positioned in a tube furnace, held at 450°C for two weeks and cooled to 400 °C and held again for two weeks for the full oxygenation. After long-term oxygenation, particles were again sieved to conform their sizes between 10 and 20 μm. For the c-axis grain alignment (c-axis // H), the particles were put into the hole of a cylindrical shape with a dimension of 4 mm diameter and 3 mm depth machined in a 5×5×5 mm^3 copper cube. An anaerobic polymer of low viscosity (Loctite RC/609) was added and the powders were aligned with a 3 Tesla electromagnet with one face of the cube pressed against the pole piece assuring a reference surface perpendicular to the alignment direction. The polymer was cured with flowing N_2 gas. Larger samples prepared in the same field were subject to optical and x-ray diffraction analysis to determine the degree of alignment The particles embedded in Loctite were observed to be mostly (roughly, more than 80%) single grains under the optical microscopy.

Magnetic Relaxation and Hysteresis Width Measurements

Magnetic measurements were performed in a Quantum Design MPMS SQUID magnetometer. The magnetically aligned specimens were measured with their c-axis parallel to the applied field in the SQUID chamber. Alignment error between the

measuring field and the direction of the applied field for particle alignment was less than 2°. Both magnetic relaxation and hysteresis width were measured at 1 Tesla.

In all the measurement procedures, the scan length was set at 3 cm to minimize the variation in the applied field (< 0.05%) as the sample moved through the SQUID coils. In order to minimize the flux trapped in the SQUID coils at zero field and hence, to assure the same initial measurement condition, the field was oscillated to zero from 3 Tesla at 150 K as a degaussing procedure prior to each measurement.

For the analysis of the flux creep in the superconductors, a critical state distribution of flux lines within the sample is assumed. Deviation from this distribution may arise from many sources including a non-monotonic approach to a set field or temperature, inhomogeneity in the measuring field, and field or temperature fluctuations during measurement. In order to separate measurement artifacts from sample properties, three different procedures were used. In theory, all these procedures should yield the same critical state flux distribution within the sample.

In the first procedure, the sample is zero field cooled (ZFC) to the measurement temperature. When the temperature is stabilized, the external magnetic field is increased to 1 Tesla in the no overshoot mode. Immediately after the field is stabilized at 1 Tesla, magnetization measurements are performed at programmed intervals up to 85 minutes. When this relaxation measurement is finished, the external field is increased to 5 Tesla in the overshoot mode and held for 10 minutes. The external field is then decreased to 1 Tesla in the no overshoot mode. When the external field is stabilized, the relaxation measurement is performed at the same intervals as used for the increasing field step. This procedure will be referred as the field stepped method.

In the second procedure, the magnetic field is increased in small increments such that 0.02 T steps for $H \leq 0.1$ T, 0.05 T steps for $0.1 \leq H \leq 1.0$ T, and 0.1 T steps for

$H > 1.0$ T in the no overshoot mode. With this method, an overshoot in the applied field is expected to be reduced [103]. The magnetic relaxation measurement is performed during the hysteresis measurement (up to 2.5 Tesla) by stopping at 1 Tesla. All other conditions are exactly the same with those in the field stepped method. This sequence will be referred as the graded field method.

Even in the no overshoot mode, we measure a slight decay in the applied magnetic field immediately after setting the persistence switch, which is due to the magnetic relaxation of the SQUID coils. Thus, it is questionable to achieve a critical state distribution of flux lines. In the last procedure, the critical state is achieved by stepping the temperature after the field is stabilized. With the same scan length of 3 cm and degaussing procedure, the sample is zero field cooled (ZFC) to the temperature which is 5 K lower than a measuring temperature. When the temperature is stabilized, the external magnetic field is increased to 1 Tesla in the no overshoot mode in a single step. After the applied field is stabilized and held for 30 minutes, the temperature is increased by 5 K to the measuring value. As soon as the temperature is stabilized, the magnetic relaxation is measured at programmed intervals up to 85 minutes. The temperature is then reduced by 5 K and the applied field is increased to 5 Tesla in the oscillation mode and held for 10 min. The applied field is then decreased to 1 Tesla in the no overshoot mode. After the applied field is stabilized and held for 30 minutes, the temperature is increased by 5 K to the measuring value and the relaxation measurement is performed as previously described. This method will be referred as the stepped temperature method.

In all the above measurement procedures, there is an uncertainty in the zero time ($t = 0$). The effect of this uncertainty is very pronounced for short time data where it is compounded by the fact that it takes approximately twenty seconds to make a measurement. This will be discussed in more detail later. Magnetizations measured for

both increasing field and decreasing field are represented as M^+ and M^- respectively.

While flux creep rates (dM/dln(t)) can be directly determined from the measured magnetization values, calculation of the flux pinning energy requires a knowledge of J_c which is usually calculated from the magnetic hysteresis width ΔM. As noted earlier, since the zero time $t = 0$ is not well defined experimentally and the initial magnetization relaxations occur very fast, large errors can be involved in determining ΔM. From the magnetic relaxation measurements made for both increasing and decreasing fields, ΔM may be accurately determined as a function of time. If the magnetic relaxation is assumed to follow logarithm-time decay, ΔM should be linear in ln(t) so that the relaxation data may be fit to the equation $\Delta M(t) = \Delta M_o + A\ln(t)$ by the least square method. The hysteresis width ΔM_o (= ΔM(1 sec)) obtained by fitting to this equation was used to calculate the effective flux pinning potential (U_o). This procedure reduced the error in ΔM_o due to an ambiguity in the experimental data for the short time since the large time values dominate the fit.

4.3. Results and Discussion

Field cooled magnetization curves on the bulk samples used for the present study are shown in Fig. 4.1. We can see that all samples have sharp transitions and consistent Meissner fractions. In addition, for $x \leq 0.06$, there is no decrease in T_c.

As in Y123 [101], the decays in magnetization are as much as 10 - 25% of the initially measured values after only 85 minutes in our samples. In comparison with conventional superconductors, not only is the pinning energy lower but also the operating temperature is higher. Therefore, this large magnetization relaxation is considered to be due to weak pinning of the flux lines in these materials.

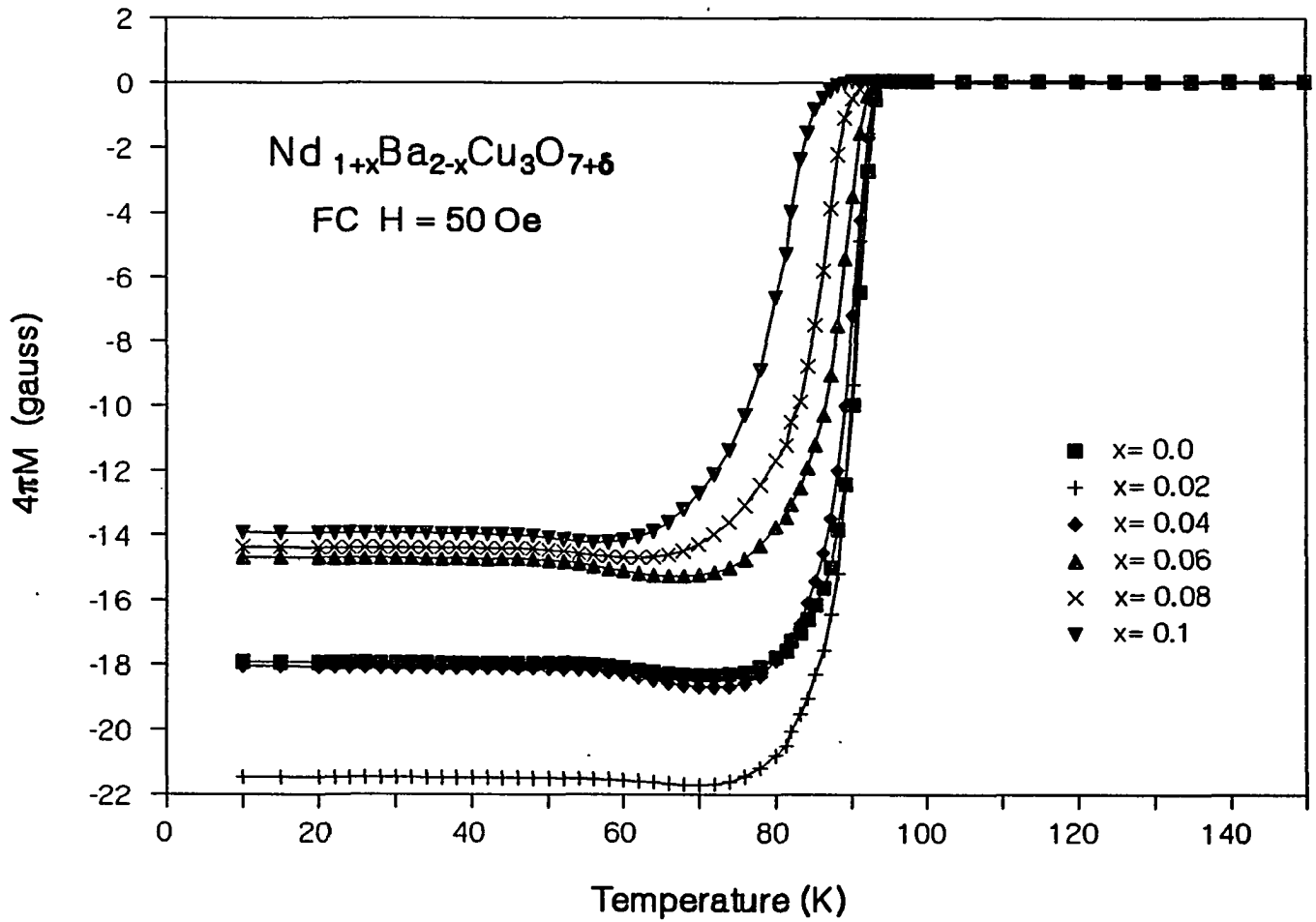

Figure 4.1. Field Cooled (FC) DC magnetization curves on the bulk samples for $0.0 \leq x \leq 0.1$ in $Nd_{1+x}Ba_{2-x}Cu_3O_{7+\delta}$.

According to a thermally activated flux creep theory [55,98], the magnetization (i.e., the screening supercurrent) decays logarithmically as a function of time in the critical state. At low temperatures ($T \leq 40$ K), the decay in magnetization is linear with respect to ln(t) for all compositions studied. As the temperature increases (≥ 50 K), the deviation from linearity in M^+ vs ln(t) becomes significant. This behavior is commonly observed for different measuring procedures or measuring time intervals. Therefore, the logarithmic time decay of magnetization is considered to occur only at low temperatures, tentatively below 50 K.

For an example, the magnetization for increasing field, M^+ vs ln(t) is plotted for all compositions at 10 K and 1 Tesla in Fig. 4.2. This plot is from the data measured by the temperature stepped method. Each curve was offset by the value of M at $t \approx 85$ min to emphasize the difference in the slopes. We can see that the slopes depend on the composition x of the solid solution. When we made the same plot with Fig. 4.2 for all temperatures studied, it was commonly noticed that as the concentration of Nd on Ba sites increases, the slope first increases up to $x = 0.02$-0.04 (1-2% Nd substitution for Ba sites) and then decreases.

The apparent deviation from linearity in M^+ vs ln(t) is also observed at low temperatures for short time, usually for $\ln(t) < 5.5$ (i.e., $t < 4$ min) in Fig. 4.2. This is probably originated from several factors: the ambiguity in determining the exact starting time of relaxation, $t = 0$ (i.e., a zero offset in time), the measuring time (≈ 20 sec), and a small decay in the applied field. Since we used the stepped temperature method, the potential effect of a small decay in the applied field on the magnetization might be avoided. However, other two factors - a zero offset in time and the measuring time - are fundamentally uncontrollable and hence large error in ln(t) for short time data can be generated. Therefore, the deviation from linearity in M^+ vs ln(t) for short time data is

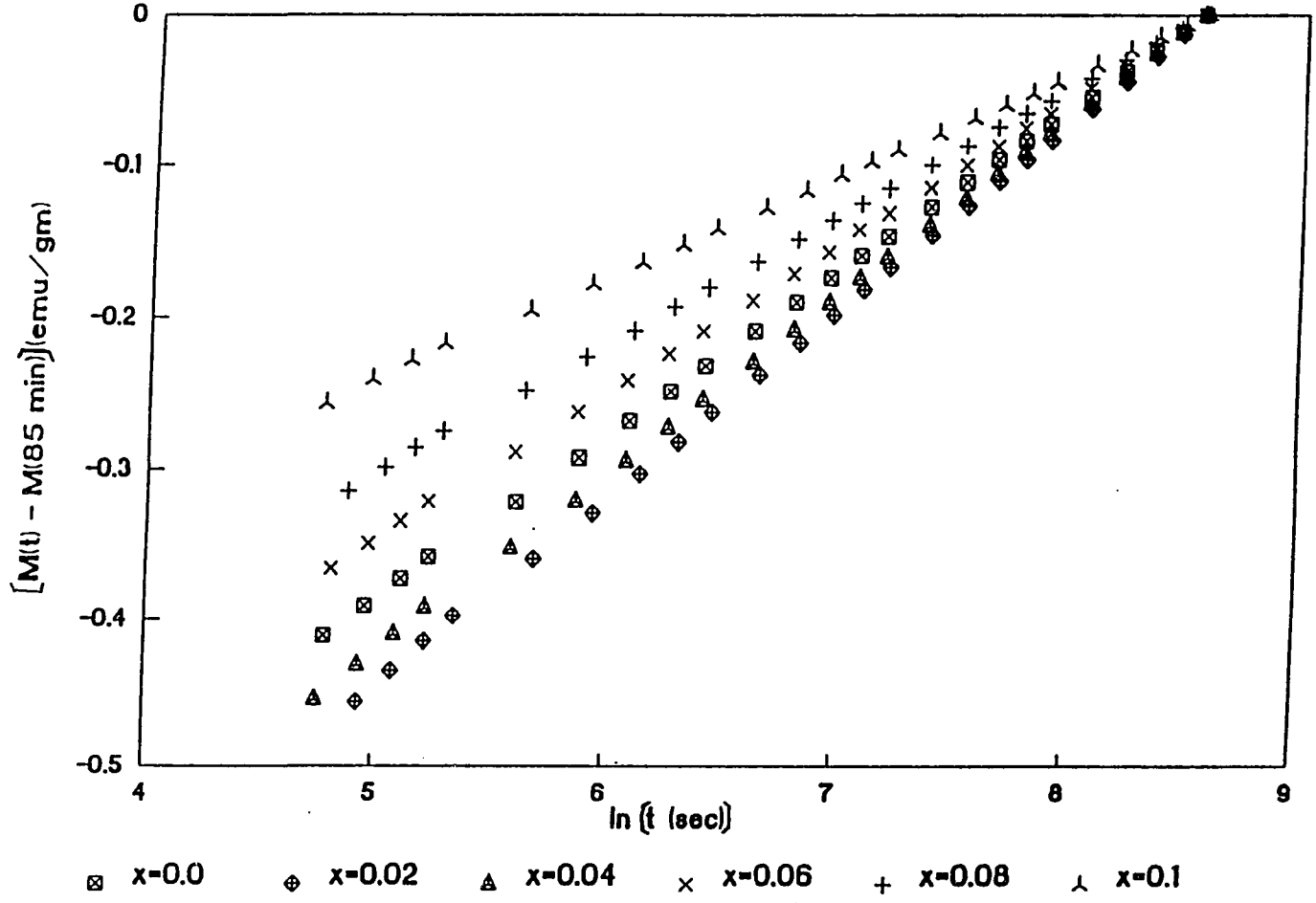

Figure 4.2. Magnetization for increasing field, M^+versus ln(t) at 10 K and 1 Tesla.

probably caused by measurement artifacts.

In order to accurately determine flux creep rates ($dM^+/d\ln(t)$) from a linear least square fit of M^+ (or J_c) vs ln(t), a zero offset in time must be considered. The zero offset in time arises from a settling time which is required for the instrument to be stabilized at a set temperature before starting measurements. It is, therefore, incorrect to determine the starting time of the first measurement as $t = 0$.

If the flux creep rates, $dM^+/d\ln(t)$, are determined by adjusting the zero offset in time to get maximum linearity in M^+ vs ln (t), we find that the flux creep rates are almost identical to values determined only from the data in the time interval of ln(t) $\approx$ 7 - 8.5 without adjustment. The zero offsets in time for all compositions were less than two minutes, which means the magnetic relaxation actually begins less than two minutes before the first measurement. This is consistent with the settling time of the instrument. Furthermore, if we take into account an experimental error bar in ln(t) due to the measuring time, this approach to adjust zero offset in time excellently supports the logarithmic time decay of magnetization because the line having a slope of maximum linearity passes through the error bars of adjusted short time data as well as long time data. However, short time data should be excluded from the calculation of the flux creep rates if we do not consider the zero off set in time.

The flux creep rates as a function of temperature are shown in Fig. 4.3 for all compositions. As temperature increases, the flux creep rate abruptly decreases up to 30 K and thereafter decreases less abruptly above 40 K. However, if we calculate the normalized flux creep rates, S ($\equiv d\ln M^+_{irr}/d\ln(t)$), it is noticed that S keeps almost constant independent of temperature for < 30K. This trend has been generally observed in Y123 superconductors [103, 114] For the calculation of S, the irreversible portion of magnetization, M^+_{irr} was determined through the procedure suggested by Xu et al. [103],

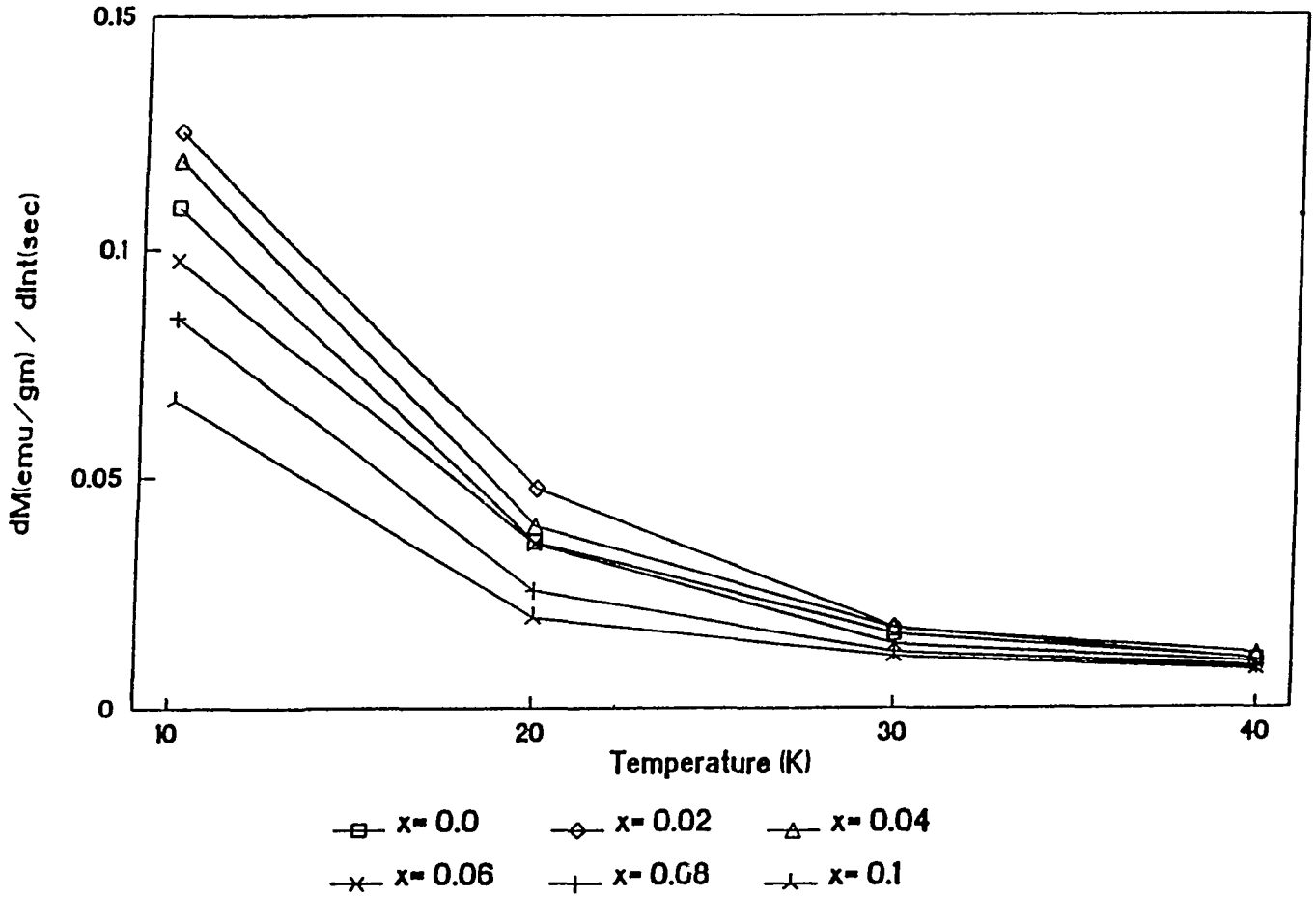

Figure 4.3. Flux creep rates [= $dM^{+}/d\ln(t)$] as a function of temperature for all compositions studied.

in which the reversible portion, M_{rev} is subtracted from the measured magnetization. M^+_{rev} is due to the magnetic moment from Nd and other magnetic impurities, which is assumed to be time-independent.

For the estimation of the effective pinning potential (U_o), we used the following relationship as derived in Eq.(8) in the previous section;

$$dM^+/d\ln(t) = (\Delta M_o/2)\, kT/U_o \qquad (12)$$

where, U_o is the effective flux pinning potential and ΔM_o is the hysteresis width at the very moment magnetic relaxation starts.

In Eq.(12), ΔM_o at t= 1sec was used for the calculation of U_o. In order to determine ΔM_o, both $R^+(= dM^+/d\ln(t))$ for increasing field and $R^-(= dM^-/d\ln t)$ for decreasing field were calculated first. By interpolating ln(t) of M^- on that of M^+, ΔM is determined with respect to ln(t) of M^-. Since $\Delta M = \Delta M_o + (R^+ + |R^-|)\ln(t)$, ΔM_o at t= 1 sec can be obtained by the linear least square fit. For an example, ΔM_o vs composition at H= 1 Tesla and 10 K is shown in Figure 4.4. ΔM_o increases as Nd substitution increases up to x = 0.02-0.04 and then decreases, which is also observed for all temperatures studied. The dependence of ΔM_o on x represents the critical current dependence on x and hence we attribute the increased ΔM_o to the flux pinning effect. However, when we calculate $U_o(x)$, U_o is proportional to $(2/\Delta M_o)dM^+/d\ln(t)$ at a fixed temperature from Eq.(12). Comparing the dependence of $dM^+/d\ln(t)$ vs x in Fig. 4.2 and ΔM_o vs x in Fig. 4.4, we note the behavior is similar and indeed, if we calculate $U_o(x)$, we find that it is constant within experimental error at T = 10 K.

The hysteresis width ΔM_o as a function of temperature for all compositions is shown in Fig. 4.5, which also reveals similar trend as in Figure 4.3. Since $J_c \propto \Delta M$, we

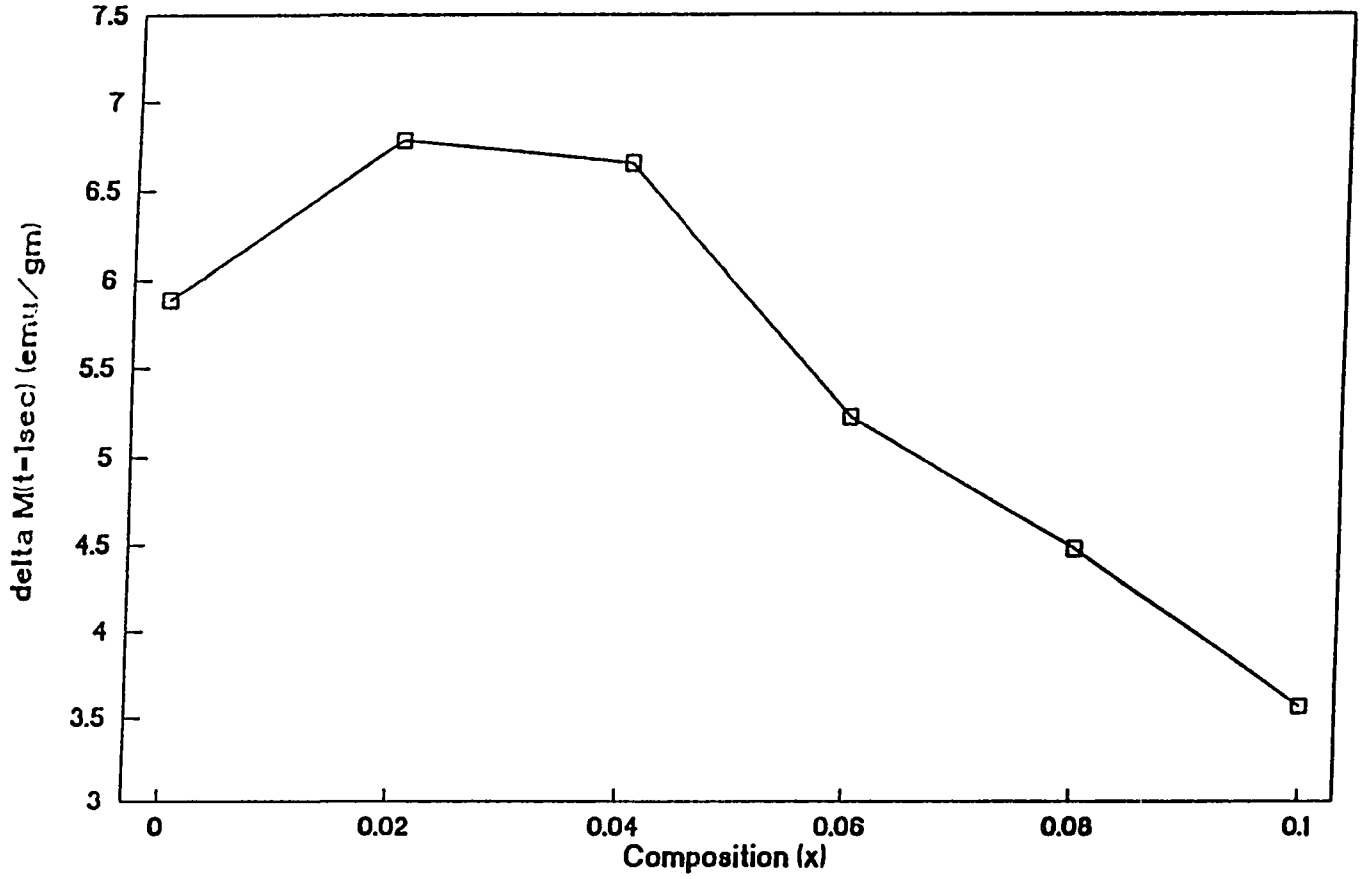

Figure 4.4. Hysteresis width after t = 1 sec (i.e., ΔM_o in the text) versus composition at H = 1 Tesla and 10 K.

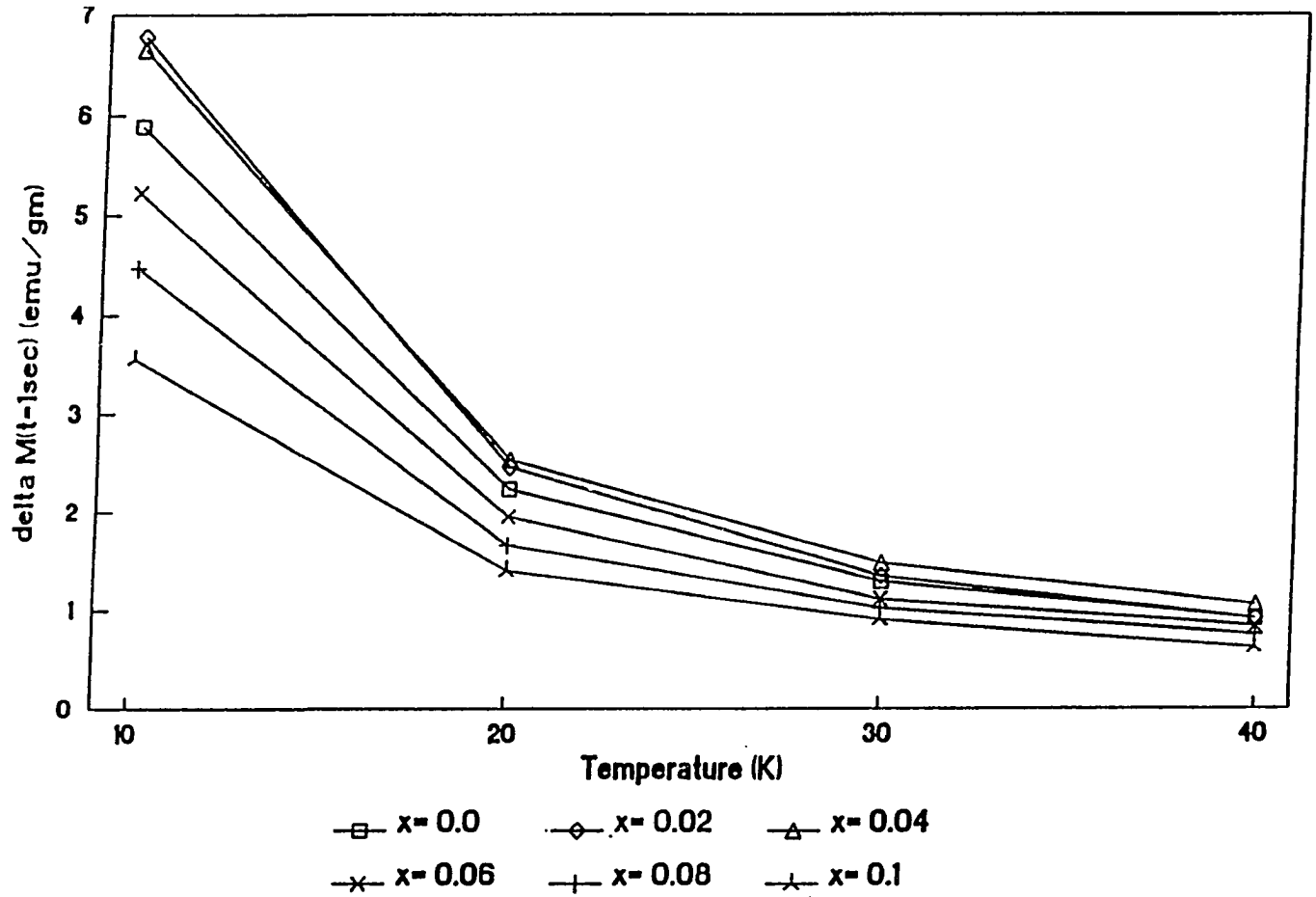

Figure 4.5. Hysteresis width (ΔM_o) as a function of temperature for compositions studied.

can see that J_c abruptly decreases as temperature increases.

The effective flux pinning potential U_o as a function of temperature is plotted in Fig. 4.6. This figure indicates that, except x= 0.1, there is no apparent effect of Nd substitution for Ba sites on the effective flux pinning energy within experimental error. For the composition of x=0.1, however, the apparent depression in U_o at high temperature (> 30 K) is considered to be due to the relatively low superconducting transition temperature of this sample.

For our purposes, we have chosen a simple comparison based on Anderson-Kim flux creep model since J_c and T_c are essentially constant in our solid solution system at a fixed temperature. It must be, however, noted that comparison of these U_o values determined in this manner with those of materials having significantly different J_c and T_c is highly questionable.

A detailed approach such as that of Maley et al. [110] would probably remove the temperature dependence of U_o. To avoid *a priori* assumptions about the effective barrier, $U_e(M)$, they used a rate equation for thermally activation motion of flux suggested by Beasley et al. [56], which is derived into the graphical form of U_e vs $(M - M_{eq}) \propto J_c$. Where, U_e is the effective barrier at J_c and U_o is the pinning potential at the intercept when the tangential line at J_c is extrapolate to U-axis (i.e., $J_c \rightarrow 0$). After that, Maley et al. selected the relationship from the models derived by others which give the relation between U_e and $(M - M_{eq})$ closest to their experimentally derived curves. It is suggested that U_e is non-linear with J and the relation of U_e vs J follows a kind of universal curve as proposed by Beasley et al. In order to fit the magnetization data to the universal curve, they used the fitting constants. This procedure is physically unclear yet, but since the fitting constants can be interpreted as the values which enable to differentiate different systems following different universal curves, it becomes possible to compare the effective barrier

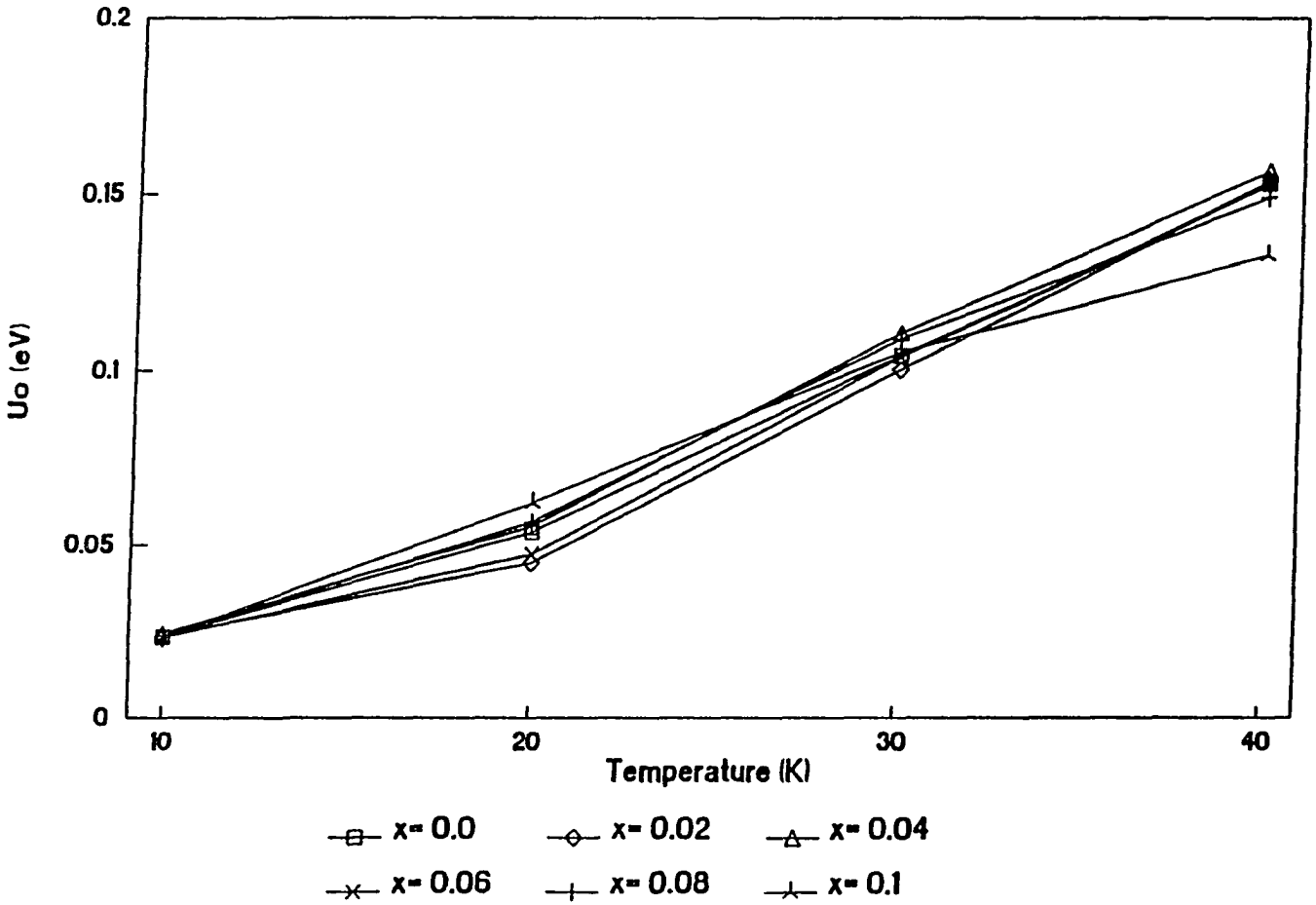

Figure 4.6. The effective flux pinning potential, U_o as a function of temperature for all compositions studied.

energies between different systems. From their data plot, we can see that there can be apparent difference in M (i.e., J_c) though there is no apparent difference in U_o at a fixed temperature (see Fig. 3.5(b)) The reason is probably due to the difference in the density of effective pinning sites which have almost identical depth of pinning potential. If we apply this interpretation to our data, highest ΔM_o values for samples of x = 0.02-0.04 in Fig.4.4 and Fig.4.5 suggest that the optimum density of solutes for effective pinning sites are 1-2 % Nd in Ba site since the effective pinning potential depth is almost identical for all compositions as shown in Fig. 4.6.

Since a point defect is the major defect-type in our system, we may apply the results of Hylton and Beasley [53] who suggested that the pinning in Y123 thin films is due to a large density of point defects. Following to their derivation (see Eq. (11) in chapter 3), a characteristic pinning energy U_o, which represents minimum energy for depinning a vortex line from defects on it, is proportional to a pinned vortex segment length, l_p. Since the composition x can be considered as a number of density of point defects, U_o will be proportional to $\sqrt[3]{x}$. If we follow their approach as discussed in the theory section and apply it to our system, the point defect density of x=0.08 composition is twice that of x=0.04 composition and hence, $U_o(x=0.08)$ is only $\sqrt[3]{2}$ times higher than $U_o(x=0.04)$. Since we see no sharp drop in U_o for x= 0.0 composition, there may exist large number of intrinsic defects which is of the order of extrinsic defects in x= 0.04 sample. The intrinsic defects are probably related to the tentative lower solubility limit of x= 0.04 in Nd123 solid solution. According to the flux pinning mechanism by Hylton and Beasley, it is, therefore, predicted that we can not observe apparent difference in the flux pinning energies, U_o in the Nd123 solid solution (x=0.0 - 0.1) superconductors within experimental error.

4.4. Summary

Six c-axis oriented powder samples with the composition of x = 0.0 to 0.1 in $Nd_{1+x}Ba_{2-x}Cu_3O_{7+\delta}$ have been prepared for magnetic relaxation measurements at 1 Tesla and various temperatures. Our results have shown that J_c is a function of x. However, for larger values of J_c, the flux creep rates are correspondingly larger so that when the activation energy is calculated by following to the conventional thermally activated flux creep theory, $U_o(x)$ is independent of x. For the sample of x=0.1, the apparent decrease in U_o at high temperatures (T > 30 K) probably originates from its relatively low superconducting transition temperature. Furthermore, since the point defect is regarded as the major defect-type in the present system, we applied the results of Hylton and Beasley to our system, which suggests that characteristic depinning energy, U_o values of the Nd123 solid solution (x=0.0 - 0.1) are also essentially constant within experimental error. In conclusion, there is no apparent effect of Nd substitution for Ba sites on the effective flux pinning energy.

GENERAL SUMMARY

$NdBa_2Cu_3O_7$ (Nd123) is one of the family of $REBa_2Cu_3O_7$ (RE123) superconductors (RE = Y and rare earths), commonly having the superconducting transition temperature (T_c) of about 90 K. From a processing standpoint Nd123 is interesting because it exhibits both a higher peritectic decomposition temperature and a broader primary solidification range than Y123. Unlike Y123, the low temperature orthorhombic phase exists over a range of Nd compositions in $Nd_{1+x}Ba_{2-x}Cu_3O_{7+\delta}$ solid solution (Nd123ss) with little effect on T_c. These factors should make Nd123ss an interesting alternative to Y123 for applications. In addition to easing some processing constraints, Nd substitution for Ba sites may have the added benefit of introducing enhanced pinning of the magnetic flux due to variations in the local oxygen order.

In this study, the phase diagram in the Nd-Ba-Cu-O system, superconductivity in Nd123ss, and flux pinning by Nd substitution for Ba sites have been investigated. In the phase diagram study, the discrepancies in the published phase diagrams were clarified. Significant results are as following. The solubility limits of Nd123ss is $0.04 \leq x \leq 0.6$. In stead of Nd_3BaCuO_y, Nd_2BaCuO_{10} is an equilibrium phase having a solid solution. In the BaO-rich region, a new phase $NdBa_6Cu_3O_y$ has been discovered.

Superconductivity in $Nd_{1+x}Ba_{2-x}Cu_3O_{7+\delta}$ was studied for well characterized samples with sharp transitions. With the substitution of Nd^{+3} for Ba^{+2}, there is an increase in the O(5) sites surrounding this substitution. While for $x > 0.1$ there is a significant depression of T_c with $T_c < 5$ K for $x > 0.4$, for $x < 0.1$ there is no substantial decrease in T_c within experimental error. T_c vs x is characterized by two plateaus analogous to T_c vs d in $YBa_2Cu_3O_{7-d}$. Analysis of oxygen contents of Nd123ss suggests the analogy with Y123 is valid. The transition width and Meissner fraction for all

Nd123ss samples are strongly dependent on the temperature at which the material is sintered. Hysteresis measurements show good intragranular critical currents (J_c) at high fields but the intergranular J_c are still low.

In a Type II superconductor at high field, the magnetic flux lines penetrate the material. If the flux lines are free to move, energy transfer from the current to the flux line lattice results in a non-zero resistance and hence the flux lines must be pinned in order to increase J_c. While T_c is not affected over the range $0<x<0.1$, the oxygens surrounding the substituted Ba sites are expected to locally suppress the superconducting order parameter. Such a local suppression of the order parameter may be expected to act as a pinning site for magnetic flux enhancing the critical current density. Hysteresis measurements exhibited a small increase in the magnetic J_c, but flux creep measurements showed no apparent effects of this substitution on the flux pinning energy.

REFERENCES

1. W. Wong-Ng, B. Paretzkin, and E. R. Fuller, Jr, (submitted to Advances in X-ray diffraction) (1989).

2. K. Oka, M. Saito, M. Ito, K. Nakane, K. Murata, Y. Nishihara, and H. Unoki, Jpn. J. Appl. Phys. Lett. **28**, L219 (1989)

3. J. Ullman, R.W. McCallum, and J. D. Verhoeven, J. Mater. Res. **4**, 752 (1989)

4. F. Sujia, X. Shisheung, L. Jingkui, C. Guaungchang, and Z. Zongxiang, Mod. Phys. Lett. B **2**, 1073 (1988)

5. S. Takekawa, H. Nozaki, Y. Ishizawa, and N. Iyi, Jpn. J. Appl. Phys. **26**, L2076 (1987)

6. S. Li, A. Hayri, K. V. Ramanujachary, and M. Greenblatt, Phys. Rev. B **38**, 2450 (1988)

7. K. Zhang, B. Dabrowski, C. W. Chiang, R. D. Shull, and E. R. Fuller, Jr., *High Temperature Superconducting Compounds: Processing of Related Properties*, edited by S. H. Whang and A. DasGupta, The Minerals, Metals and Materials Society, 1989

8. J. E. Blendall, W. Wong-Ng, C. K. Chiang, R. D. Shull, and E. R. Fuller,Jr., *High Temperature Superconducting Compounds: Processing and Related Properties*, Edited by S. H. Whang and A. Dasgupta, The Minerals, Metals and Materials Society, p193 (1989)

9. H. Kammerlingh Onnes, Leiden Comm., **120b**, **122b**, **124c** (1911)

10. B. W. Roberts, *Handbook of Chemistry and Physics*, 61st Ed., E-87, 1980

11. B. W. Roberts, *NBS Technical Note* 482 (1969); *NBS Technical Note* 983 (1978)

12. J. R. Gavaler, Appl. Phys. Lett. **23**, 480 (1973)

13. L. R. Testardi, J. H. Wernick, and W. A. Royer, Solid State Commun. **15**, 1 (1974)

14. W. J. Painter, *High Temperature Superconduction: Overview in Superconductivity: Synthesis, Properties, and Processing*, edited by William E. Hatfield and John H. Miller, Jr., (Marcel Dekker, New York, 1988)

15. C. W. Chu, Presented at the 11th International Vacuum Congress and the 7th International Conference on Solid Surfaces, 25-29 September 1989, Koln, Federal Republic of Germany

16. J. G. Bednortz and K. A. Müller, Z. Phys. B **64**, 189 (1986)

17. C. W. Chu, P. H. Hor, R. L. Meng, L.Gao, Z. J. Huang, and Y. Q. Wang, Phys. Rev. Lett. **58**, 405 (1987)

18. S. Uchida, H.Takagi, K. Kitazawa, and S. Tanaka, Jpn. J. Appl. Phys. **26**, L1 (1987)

19. H. Takagi, S. Uchida, K. Kitazawa, and S.Tanaka, Jpn. J. Appl. Phys. **26**, L123 (1987)

20. R. J. Cava, R. B. van Dover,B.Batlogg, and E. A. Rietman, Phys. Rev. Lett. **58**, 408 (1987)

21. J. M. Tarascon, L. H. Greene, W. R. Mckinnon, G. W. Hull, and T. H. Geballe, Science **235**, 1373 (1987)

22. J. G. Bednortz, K. A. Müller, and M. Takashige, Science **235**, 73 (1987)

23. M. K. Wu, J. R. Ashburn, C. J. Torng, P. H. Hor, R. L. Meng, L. Gao, Z. J. Huang, Y. Q. Wang, and C. W. Chu, Phys. Rev. Lett. **58**, 908 (1987)

24. Z. Zhao, C. Liquan, Y. Qiansheng, H. Yuzhen, C. Gerghua T. Ruming, L. Guirong, C. Changgeng, C. Lie, W. Lianzhong, G. Shuquan, L. Shanlin, and B. Jianqing, Kexue Tongbao, **No. 6**, 412 (1987)

25. L. C. Bourne, M. L. Cohen, W. N. Creager, M. F. Crommie, A. M. Stacy, and A. Zettl, Phys. Lett. A **120**, 494 (1987)

26. E. M. Engler, V. Y. Lee, A. I. Nazzal, R. B. Beyers, G. Lim, P. M. Grant, S. S. P. Parkin, M. L. Ramirez, J. E. Vazquez, and R. J. Savoy, J. Am. Chem. Soc. **109**, 2848 (1987)

27. A. M. Stacy, J. V. Badding, M. J. Geselbracht, W. K. Ham, G. F. Holland, R. L. Hoskins, S. W. Keller, C. F. Millikan, and H. C. Zur Loye, J. Am. Chem. Soc. **109**, 2528 (1987)

28. W. J. Gallagher, R. L. Sandstrom, T. R. Dinger, T. M. Shaw, and D. A. Chance, Solid State Comm. **63**, 147 (1987)

29. P. M. Grant, R. B. Beyers, E. M. Engler, G. Lim, S. S. P. Parkin, M. L. Ramirez, V. Y. Lee, A. Nazzal, J. E. Vazquez, and R. J. Savoy, Phys. Rev. B **35**, 7242 (1987)

30. J. M. Tarascon, L. H. Greene, W. R. Mcknnon, and G. W. Hull, Phys. Rev. B **35**, 7115 (1987)

31. R. J. Cava, B. Batlogg, R. B. van Dover, D. W. Murphy, S. Sunshine, T. Siegrist, J. R. Remeika, E. A. Rietman, S. Zahurak, and G. P. Espinosa, Phys. Rev. Lett. **58**, 1676 (1987)

32. R. Beyer, G. Lim, E. M. Engler, R. J. Savoy, T. M. Shaw, T. R. Dinger, W. J. Gallagher, and R. L. Sandstrom, Appl. Phys. Lett. **50**, 1918 (1987)

33. T. Siegrist, S. Sunshine, D. W. Murphy, R. J. Cava, and S. M. Zahurak, Phys. Rev. B **35**, 7137 (1987)

34. C. N. R. Rao, P. Ganguly, A. K. Raychandgri, R. A. Mohan Ram, and K. Sreedhar, Nature **326**, 856 (1987)

35. P. H. Hor, R. L. Medng, Y. Q. Wang, L. Gao, Z. J. Huang, J. Bechtod, K. Forster, and C. W. Chu, Phys. Rev. Lett. **58**, 1891 (1987)

36. B. T. Matthias, H. Suhl, and E. Corenzwit, Phys. Rev. Lett. **1**, 92 (1958)

37. H. J. Rosen, R. M. McFarlane, E. M. Engler, V. Y. Lee, and R. D. Jacowitz, Phys. Rev. B **38**, 2460 (1988)

38. H. Maeda, Y. Tanaka, M. Fukutomi, and T. Asano Jpn. J. Appl. Phys. Lett. **27**, L206 (1988)

39. Z. Z. Sheng and A. M. Hermann, Nature **332**, 55 (1988)

40. Y. Tokura, H. Takagi, and S. Uchida, Phys. Rev. Lett. **62**, 1197 (1989)

41. L. F. Schneemyer, E. M. Gyorgy, and J. V. Wasqczak, Phys. Rev. B **36**, 8804 (1987)

42. T. R. Dinger, T. K. Worthington, W. J. Gallagher, and R. L. Sandstrom, Phys. Rev. Lett. **58**, 2687 (1987)

43. K. Watanbe, Appl. Phys. Lett. **54**, 575 (1989)

44. P. Chaudhari, R. H. Koch, R. B. Laibowitz, T. R. McGuire, and R. J. Gambino, Phys. Rev. Lett. **58**, 2684 (1987)

45. R. B. Laibowitz, R. H. Koch, P. Chandari, and R. J. Gambino, Phys. Rev. B **35**, 8821 (1987)

46. M. J. Kramer, L. S. Chumbley, and R. W. McCallum, J. Mater. Science **25**, 1978 (1990)

47 M. J. Kramer, and S. R. Arrasmith, IEEE Transactions on Magnetics, 27, **920** (1991)

48. R. B. van Dover, E. M. Gyorgy, L. F. Schneemeyer, J. W. Mitchell, K. V. Rao, R. Puzniak, and J. V. Waszczak, Nature **342**, 55 (1989)

49. L. Civale, A. D. Marwick, M. W. McElfresh, T. K. Worthington, A. P. Malozemoff, F. Holtzberg, J. R. Thompson, and M. A. Kirk, Phys. Rev. Lett. **65**, 1164 (1990)

50. L. Civale, A. D. Marwick, T. K. Worthington, M. A. Kirk, L. Krusin-Elbaum, Y. Sun, J. R. Clem, and F. Holtzberg, Phys. Rev. Lett. **67**, 648 (1991)

51. S. Jin, T. H. Tiefel, S. Nakahara, J. E. Graebner, H. M. O'Bryan, R. A. Fastnacht, G. W. Kammlott, preprint (submitted to Appl. Phys. Lett.) (1989)

52. M. B. Maple, J. M. Ferreira, R. R. Hake, B. W. Lee, J. J. Neumeier, C. L. Seaman, K. N. Yang, and H. Zhou, J. Less-Commom Metals, **149**, 405 (1989)

53. T. L. Hylton and M. R. Beasley, Phys. Rev. B **41**, 11669 (1990)

54. P. Allenspach, PhD Thesis, Title : Neutronenspektroskopische Untersuchung von Hochtemperatursupraleiten, ETH, Zürich, Switzerland (1991)

55. P. W. Anderson, Phys. Rev. Lett. **9**, 309 (1962)

56. M. R. Beasley, R. Labush and W. W. Webb, Phys. Rev. **18**, 682 (1969)

57. F. A. Hummel, *Introduction to Phase Equilibria in Ceramic Systems*, Marcel Dekker, Inc, p 124 (1984)

58. R. W. McCallum, Critical parameters in the RE123 processing, J. Metal, Jannuary, 50 (1989)

59. K. W. Lay and G. M. Renlund, J. Am. Ceram. Soc. **73**, 1208 (1990)

60. T. Aselage and K. Keefer, J. Mater. Res. **3**, 1279 (1988)

61. H. Fjellvag, P. Karen, A. Kjekshus, P. Kofstad, and T. Norby, Acta Chemica Scandinavica A **42**, 178 (1988)

62. Balachandran et al., Mater. Lett. **8**, 454 (1989)

63. K. No, J. D. Verhoeven, R. W. McCallum, and E. D. Gibson, IEEE MAG **25**, 2184 (1989)

64. T. M. Shaw, S. L. Shinde, D. Dimow, R. F. Cook, P. R. Duncombe, and C. Kroll, J. Mat. Res. **4**, 248 (1989)

65. S. Jin, T. H. Tiefel, R. S. Sherwood, R. B. van Dover, M. E. Davis, G. W. Kammlott, and R. A. Fastnacht, Phys. Rev. B **37**, 7850 (1988)

66. R. W. McCallum, M. J. Kramer, T. J. Folkerts, S. R. Arrasmith, B. D. Merkle, S. I. Yoo, Y. Xu and K. W. Dennis, "Conainterless Melt Processing of $REBa_2Cu_3O_{7-x}$" {RE = Y, Gd, Nd} to be appeared in *High Temperature Superconductors*, Nova Science Publishing, NY (1992)

67. M. Murakami, Mod. Phys. Lett. B **4**, 163 (1990)

68. D. E. Morris, N. G. Asmar, J. H. Nickel, R. L. Sid, and J. Y. T. Wei, Physica C **159**, 287 (1989)

69. D. Shi and D. W. Capone II, preprint (1989)

70. K. Zhang, B. Dabrowski, C. W. Segre, D. G. Hinks, I. K. Schuller, J. D. Jorgrnsen, and M. Slasik, J. Phys. C : **20**, L935 (1987)

71. S. A. Hodorowicz, J. Czerwonka, and H. A. Eick, J. Sol. Sta. Chem. **88**, 391 (1990)

72. E. R. Hovestreydt, J. Appl. Crystallogr. **16**, 651 (1983)

73. K. Osamura and W. Zhang, Z. Metallkde. **82**, 408 (1991)

74. R. Kipka and H. Müller-Buschbaum, Z. Naturforsch. B **32**, 121 (1977)

75. G. Wang, S. J. Hwu, S. N. Song, J. B. Ketterson, L. D. Marks, K. R. Poeppelmeier, and T. O. Mason, Adv. Ceram. Mater. **2**, 313 (1987)

76. K. G. Frase and D. R. Clarke, Adv. Ceram. Mater. **2**, 295 (1987)

77. F. Abbattista, M. Vallino, and D. Mazza, Mater. Chem. Phys., **21**, 521 (1989)

78. W. Zhang and K. Osamura, Jpn. J. Appl. Phys. **29**, 1092 (1990)

79. D. M. DeLeeuw, C. A. H. A. Muutsaers, C. Langereis, H. D. A. Smoorenburg, and P. J. Mommers, Physica C **152**, 39 (1988)

80. R. S. Roth, K. L. Davis and J. R. Dennis, Adv. Ceram. Mater. **2**, 303 (1987)

81. C. L. Teske and H. Müller-Buschbaum, Z. Naturfarsch. **27**, 296 (1972)

82. L. M. Lopato, Ceramurgia Int. **2**, 18 (1976)

83. F. Abbattista, M. Vallino, and D. Mazza, Mater. Chem. Phys. **21**, 521 (1989)

84. T. Wada, N. Suzuki, T. Maeda, A.Maeda, S. Uchida, K. Uchinokura, and S. Tanaka, Appl. Phys. Lett. **52**, 1989 (1988)

85. F. Sujia, X. Shisheng, L. Jingkui, C. Guaungchang, Z. Zongxiang, Mod. Phys. Lett. B **2** [9] 1073 (1988)

86. R. W. McCallum and S. I. Yoo, IEEE Transactions on Magnetics **27**, 1143 (1991)

87. H. Nozaki, S. Takekawa, and Y. Ishizawa, Jap. J. Appl. Phys. **27**, L31 (1988)

88. R. A. Steeman, E. Frikkee, R. B. Helmholdt, D. M. Leeuw, and C. A. H. A. Mustsaers, Physica C **153-155**, 950 (1988)

89. R. J. Cava, A. W. Hewat, E. A. Hewat, B. Batlogg, M. Marezio, K. M. Rabe, J. J. Krajewski, W. F. Peck Jr, and L. W. Rupp Jr., Physica C **165**, 419 (1990)

90. Seunjens, Ph.D. Thesis, University of Wisconsin-Madison, 1990

91. C. P. Bean, Rev. Mod. Phys. **36**, 31 (1964)

92. A. M. Campbell and J. E. Evetts, Adv. Phys. **21**, 199 (1972).; M. Tinkham, *Introduction to Superconductivity*, McGraw-Hill, New York, 1975; reprinted by Robert E. Krieger E. Krieger Publishing Co., Florida, in 1980 and 1985, pp 174 - 181.

93. F. London and H. London, Proc. Roy. Soc. A **208**, 71 (1935)

94. V. L. Ginzburg and L. D. Landau, Zh. Eksperim. i Teor. Fiz. **20**, 1064 (1950)

95. A. A. Abrikosov, J.E.T.P. USSR **32**, 1442 (1957); J. Phys. Chem. Solids **2**, 199 (1957)

96. D. X. Chen and R. B. Goldfarb, J. Appl. Phys. **66**, 2489 (1989); D. X. Chen, A. Sanchez, and J. S. Munoz, J. Appl. Phys. **67**, 3430 (1990); D. X. Chen, A. Sanchez, J. Nogues, and J. S. Munoz, Phys. Rev. B **41**, 9510 (1990)

97. A. Umezawa, G. W. Crabtree, J. Z. Liu, H. W. Weber, W. K. Kwok, L. H. Nunez, T. J. Moran, and C. H. Sowers, Phys. Rev. B **36**, 715 (1988)

98. Y. B. Kim, C. F. Hempstead, and A. R. Strnad, Phys. Rev. Lett. **9**, 306 (1962)

99. M. Xu, D. Shi, and R. F. Fox, Phys. Rev. B **42**, 10773 (1990)

100. K. A. Muller, M. Takashige, and J. G. Bednorz, Phys. Rev. Lett. **58**, 1143 (1987)

101. Y. Yeshurun and A. P. Malozemoff, Phys. Rev. Lett. **60**, 2202 (1988).

102. M. Tuominen, A. M. Goldman, and M. L. Mecartney, Phys. Rev. B **37**, 548 (1988); Physica (Amsterdam) **153C-155C**, 324 (1988)

103. Youwen Xu, M. Suenaga, A. R. Moodenbaugh, and D.O. Welch, Phys. Rev. B **40**, 10882 (1989).

104. I. A. Campbell and L. Fruchter, Phys. Rev. Lett. **64**, 1561 (1990)

105. C. W. Hagen and R. Griessen, Phys. Rev. Lett. **62**, 2857 (1989); Thermally Activated Magnetic Relaxation in High Tc Superconductors, *Studies of High Temperature Supercondors* vol. **3**, edited by A. V. Narlikar (Nova Science Publ. 1989) p 159.

106. P. H. Kes, J. Aarto, J. van den Berg, C. J. van der Beek, and J. A. Mydosh, Supercond. Sci. Technol. **1**, 242 (1989).

107. M. V. Feigel'man, V. B. Geshkenbein, A. I. Larkin, and V. M. Vinokur, Phys. Rev. Lett. **63**, 2303 (1989)

108. M. P. A. Fisher, Phys. Rev. Lett. **62**, 1415 (1989).

109. E. Zeldov, N. M. Amer, G. Koren, A. Gupta, R. J. Gambino, and M. W. McElfresh, Phs. Rev. Lett. **62**, 3093 (1989).

110. M. P. Maley, J. O. Willis, H. Lessure, and M. E. McHenry, Phys. Rev. B **42**, 2639 (1990).

111. M. W. Kramer, Appl. Phys. Lett. **58**, 1086 (1991)

112. A. M. Campbell and J. E. Evetts, Adv. Phys. **21**, 199 (1972).

113. S. I. Yoo, M. J. Kramer, K. W. Dennis, and R. W. McCallum, "Granular superconductivity and Microstructure in $Nd_{1+x}Ba_{2-x}Cu_3O_{7-y}$" in High Temperature Superconductors, Materials Aspects, H. C. Freyhardt, R. Flukiger, and M. Peuckert Editors, Informationsgesellschaft, p 593 (1991)

114. A. P. Malozemoff and M. P. A. Fisher, Phys. Rev. B **42**, 6784 (1990)

ACKNOWLEDGMENTS

This moment to complete my Ph.D. must be one of the happiest moments in my life. It could have never happened to me without the help of a large number of people. Thank God for me to meet those wonderful people.

First of all, I'd like to express my deepest gratitude to professor Dr. R. W. McCallum for his support and guidance. It was a great fortune to me meeting him throughout graduate school years, and his encouragement and kindness will be remembered forever.

I also wish to gratefully acknowledge the following persons: Kevin Dennis, Matt Kramer, Jeff Shield, Youwen Xu, Brian Merkle, Steve Arrasmith, Tim Folkerts, and Ming Xu for their assistance and friendship. My thanks extend to all other group members with whom shared joyful moments and faculty members who lead me to deeper understanding in my major.

I am thankful to my parents for their love and support. I thank my lovely wife, Younshin, and lovely son, Changyul, without whose love and support this work would not have been possible.

This work was performed at Ames Laboratory under contract no. W-7405-ENG-82 with the U.S. Depart of Energy. The United States government has assigned the DOE Report number IS-T 1613 to this thesis.